Large-Scale Photonics Integration: Data Communications to Optical Beamforming

Thesis by
Aroutin Khachaturian

In Partial Fulfillment of the Requirements for the
Degree of
Doctor of Philosophy

CALIFORNIA INSTITUTE OF TECHNOLOGY
Pasadena, California

2021
Defended 12/09/2020

Aroutin Khachaturian
ORCID: 0000-0001-8304-3302

To Angineh
and
to my family.

ACKNOWLEDGEMENTS

I must start by offering my gratitude to Professor Hajimiri, who has been a great role model and has provided me incredible guidance and support throughout my Caltech experience. He has given me the freedom to pursue and expand on different projects of my choice independently. An experience so valuable and an opportunity so rare that I will be forever grateful for it.

Next, I would like to thank my thesis committee members Professor Changhuei Yang, Kerry Vahala, Azita Emami, and Axel Scherer. I would also like to thank Dr. Sanders (Sandy) Weinreb, for serving in my Candidacy committee.

I must also thank the members of CHIC lab. Professor Firooz Aflatouni, who inspired me to pursue photonics integration in graduate studies and trained me during the early days of my graduate studies. Dr. Behrooz Abiri, who is a great friend and has patiently taught me many useful skills in photonics integration and has guided me in the early days of graduate studies for photonics. Next, I must thank my friend Dr. Reza Fatemi with whom I have collaborated extensively on various projects. Reza is very analytical in his approach to research, and our discussions and collaborations have been the most fruitful. I must also thank Parham Porsandeh Khial, who is a great friend, with whom I have collaborated on a few projects, engaged in various discussions during work time, and traveled and explored outside the lab. Next, I must acknowledge my friend, Dr. Alex Pai, who has mentored me during my undergraduate studies and has been very supportive. In addition, I must thank Dr. Brian Hong who is a very caring friend and offered me his help for several projects. I also thank Professor Constantine Siders with whom I have had fruitful collaboration and discussion. I must also thank Artsroun Darbinian, who has been very helpful and our collaboration was very fruitful. I must thank Andy Zhou and Julian Sanders, who have helped me in photonics measurement and characterization.

I also acknowledge all the advice and help that I have received from my outside collaborators: Professor Larry Dalton and Dr. Delwin Elder for SOH modulator integration, Professor Kambiz Jamshidi, Reza Hosseini, and Mircea Cătuneanu for our collaborations in IHP process, and Dr. Nankyung Suh Cockerham for her valuable input regarding the Global Foundries process.

Next, I would like to thank the other member of CHIC and MICS labs with whom

I have had fruitful discussions: Dr. Saman Saeedi, Professor Manuel Monge, Craig Ives, Aryan Hashemi, Samir Nooshabadi, Austin Fikes, Matan Gal, Professor Steve Bowers, and Kaushik Dasgupta. KNI staff and members who have helped and trained me in semiconductor fabrication: Dr. Guy DeRose, Dr. Matthew Hunt, Alex Wertheim, Bert Mendoza, and my friends Dr. Mahmoud Kalaee and Lucia De Rose. Finally, I must express my utmost gratitude to my family, who has continuously supported me throughout this journey.

ABSTRACT

Integrated photonics is an emerging technology that has begun to transform our way of life with the same amount of impact that integrated CMOS electronics has. Currently, photonics integration is orders of magnitude less complicated than its electronics counterparts. Nonetheless, it serves as one of the main driving forces to meet the exponentially increasing demand for high-speed and low-cost data transfer in the Information Age. It also promises to provide solutions for next-generation high-sensitivity image sensors and precision metrology and spectroscopy instruments. In this thesis, integrated photonics architectures for solid-state photonic beamforming and processing are investigated for high-resolution and high sensitivity lens-free transceiver applications. Furthermore, high-efficiency integrated electro-optical modulators aiming to meet the demand of high-density photonic integration with improved modulation efficiency, small footprint, and lower insertion loss are investigated.

Two integrated photonic solid-state beamforming architectures incorporating two-dimensional apertures are explored. First, a novel transceiver architecture for remote sensing, coherent imaging, and ranging applications is demonstrated. It reduces system implementation complexity and offers a methodology for very-large-scale coherent transceiver beamforming applications. Next, a transmitter beamforming architecture inspired by the diffraction pattern of the slit annular ring is analyzed and demonstrated. This transceiver architecture can be used for coherent beamforming applications such as imaging and point-to-point optical communication. Finally, a coherent imager architecture for high-sensitivity three-dimensional imaging and remote-sensing applications is present. This novel architecture can suppress undesired phase fluctuations of the optical carrier signal in the illumination and reference paths, providing higher resolution and higher acquisition speed than previous implementations.

Moreover, several compact, high-speed CMOS compatible modulators that enable high-density photonic integration are explored. Ultra-compact and low insertion loss silicon-organic-hybrid modulators are designed and implemented for high-speed beamforming and high-efficiency complex signal modulation applications. Finally, a novel integrated nested-ring assisted modulator topology is analyzed and implemented for high-density and high modulation efficiency applications.

PUBLISHED CONTENT AND CONTRIBUTIONS

A. Khachaturian, B. Abiri, A. Zhou, and A. Hajimiri, "Monolithic Mach-Zehnder Interferometer Modulator in an unmodified CMOS process," 2015 IEEE Photonics Conference (IPC), pp. 394-395, 2015. Available: https://ieeexplore.ieee.org/abstract/document/7323627.
10.1109/IPCon.2015.7323627.
I designed and measured the device and wrote the paper.

A. Khachaturian, B. Abiri, and A. Hajimiri, "A compact spiral Mach-Zehnder Interferometer Modulator on SOI process," 2015 IEEE 12th International Conference on Group IV Photonics (GFP), pp. 151-152, 2015. Available: https://ieeexplore.ieee.org/document/7305996.
10.1109/Group4.2015.7305996.
I measured the device and wrote the paper.

R. Fatemi, A. Khachaturian, and A. Hajimiri, "A nonuniform sparse 2-D large-FOV optical phased array with a low-power PWM drive,"IEEE Journal of Solid-State Circuits, vol. 54, no. 5, pp. 1200–1215, 2019. Available: https://ieeexplore.ieee.org/document/8649827.
https://doi.org/10.1109/JSSC.2019.2896767.
I contributed to the design and measurement.

R. Hosseini, A. Khachaturian, M. Cătuneanu, P. P. Khial, R. Fatemi, A. Hajimiri, and K. Jamshidi, "Compact, High Extinction Ratio Silicon Mach-Zehnder Modulator with Corrugated Waveguides," Conference on Lasers and Electro-Optics, pp. SM3B.6, 2018. Available: http://www.osapublishing.org/abstract.cfm?URI=CLEO_SI-2018-SM3B.6.
10.1364/CLEO_SI.2018.SM3B.6.
I contributed to the design, measurement, and wrote the paper.

R. Fatemi, A. Khachaturian, and A. Hajimiri, "A low power PWM optical phased array transmitter with 16° field-of-view and 0.8° beamwidth," in 2018 IEEE Radio Frequency Integrated Circuits Symposium (RFIC), 2018, pp. 28–31. Available: https://ieeexplore.ieee.org/abstract/document/8428847.
https://doi.org/10.1109/RFIC.2018.8428847.
I contributed to the design and measurement.

R. Fatemi, A. Khachaturian, and A. Hajimiri, "Scalable optical phased array with sparse 2D aperture," in Conference on Lasers and Electro-Optics,Optical Society of Amer-

ica, 2018, STu4B.6. Available: http://www.osapublishing.org/abstract.cfm?URI=CLEO_SI-2018-STu4B.6.
https://doi.org/10.1364/CLEO_SI.2018.STu4B.6.
I contributed to the design and measurement.

R. Fatemi, P.Khial, A. Khachaturian, and A. Hajimiri, "Breaking FOV-aperture trade-off with multi-mode nano-photonic antennas," IEEE Journal of Selected Topics in Quantum Electronics, vol. 27, no. 1, pp. 1-14, 2021. Available: https://ieeexplore.ieee.org/document/9206075.
10.1109/JSTQE.2020.3026966.
I contributed to the theoretical analysis and simulation.

R. Fatemi, B. Abiri, A. Khachaturian, and A. Hajimiri, "High sensitivity active flat optics optical phased array receiver with a two-dimensional aperture," Opt. Express, vol. 26, no. 23, pp. 29 983–29 999, Nov. 2018. Available: http://www.opticsexpress.org/abstract.cfm?URI=oe-26-23-29983.
https://doi.org/10.1364/OE.26.029983.
I contributed to the measurement and analysis.

R. Hosseini, A. Khachaturian, M. Cătuneanu, P. P. Khial, R. Fatemi, A. Hajimiri, and K. Jamshidi, "Compact, High Extinction Ratio Silicon Mach-Zehnder Modulator with Corrugated Waveguides," Conference on Lasers and Electro-Optics, pp. SM3B.6, 2018. Available: http://www.osapublishing.org/abstract.cfm?URI=CLEO_SI-2018-SM3B.6.
10.1364/CLEO_SI.2018.SM3B.6.
I contributed to the design, measurement, and wrote the paper.

A. Pai, A. Khachaturian, S. Chapman, A. Hu, H. Wang, and A. Hajimiri, "A handheld magnetic sensing platform for antigen and nucleic acid detection," Analyst, vol. 139, pp. 143-1411, 2014. Available: https://pubs.rsc.org/en/content/articlehtml/2013/an/c3an01947k.
https://doi.org/10.1039/C3AN01947K.
I contributed in the measurement and writing of the paper.

TABLE OF CONTENTS

LIST OF ILLUSTRATIONS

NOMENCLATURE

1D-OPA. OPA with elements in a 1D grid.

2D-OPA. OPA with element in a 2D grid.

AF. Array Factor.

CRA-MZI. Cascaded Ring Assisted Mach-Zehnder Interferometer.

FOV. Field-of-View.

MZI. Mach-Zehnder Interferometer.

MZM. Mach-Zehnder Modulator.

NRA-MZI. Nested Assisted Mach-Zehnder Interferometer.

OPA. Optical Phased Array.

PAM. Pulse-Amplitude Modulation.

PTAT. Proportional to Absolute Temperature.

RA-MZI. Ring Assisted Mach-Zehnder Interferometer.

SiP. Silicon Photonics.

SISCAP. Semiconductor-Insulator-Semiconductor Capacitor.

SOH. Silicon-Organic-Hybrid.

SSB. Single-Sideband.

TF-LN. Thin-Film Lithium-Niobate.

TO. Thermo-Optic.

TOF. Time-of-Flight.

TOPS. Thermo-Optic Phase Shifter.

Chapter 1

INTRODUCTION

Today, the most basic of consumer electronics systems we use are so sophisticated in design that they operate almost magically, where the average user has no perception of the system's operation. These complex integrated systems stem from the invention of the first working transistor in 1947 in Bell Labs, which itself came from advancements in quantum mechanics in the early 20th century. Integrated electronics density has grown exponentially (Moore's law) since the realization of the integrated circuits in the 1960s. The world of electronics improved from a thousand integrated components to billions in a matter of decades thanks to high reliability, high operation speed, and low power consumption of CMOS silicon integrated electronics. Nonetheless, the fundamental physical limitations such as power dissipation and propagation speed of the signal across the chips have presented several bottlenecks for the advancement of integrated circuits [1]. While the performance of the integrated circuits continues to increase as a matter of smaller transistor size or higher complexity of integration, the margin of improvement seems to get narrower and narrower over time. A fundamentally different approach to integration or incorporation of new materials and device fabrication techniques is required to advance the field in the long term.

While one group of scientists and engineers worked on the interaction of electrons, another group applied the knowledge of quantum mechanics to the generation and manipulation of the photons and created the first working coherent photon source, the laser, in 1960 [2]. This invention opened up another world of possibilities to build systems for functions that were previously unavailable from conventional light sources and electronics. The first optical communication link using fiber and a laser source was deployed in 1975, and the speed and data-carrying capacity of optical links have grown exponentially. These advancements were partially achieved by utilizing the advances in electronics integration toward low-cost and reliable photonics fabrication and integration, creating integrated photonic platforms. This has resulted in an exponential improvement in the data-carrying capacity of optical links similar to the exponential growth of electronics. This exponentially growing performance in integrated photonics, when combined with the highly accessible and low-cost electronics devices, has created a new demand, an exponentially growing

internet traffic of about 60% [3], [4]. This rate of growth has surpassed the rate of growth of the devices that enables it. Currently, the signal-carrying capacity of a single fiber per wavelength is about 20%, and improvement in router blades increase at a rate of 40% [3] which signifies the importance of innovation in data-communication and telecommunication systems.

Parallel to the efforts in high-speed data communications, integrated photonic systems were also explored for integrated photonic beamforming. Early demonstration of integrated photonic beamforming dates to 1972 [5]–[7]. High-speed beamforming and steering (18GHz) were first demonstrated in 2008 [8]. Large-scale optical phased array in integrated silicon photonics first was demonstrated in [9]. Starting 2013, large-scale OPAs with more than 100 elements and coherent nano-photonics imagers implemented in CMOS compatible silicon photonics foundries started to show promise for solid-state high-performance OPAs with MHz and higher beam steering and capability [10]–[12]. These solid-state OPAs can be used to replace mechanically steered, MEMS, and liquid crystal based beamforming and beam steering solutions [13], [14].

Many other potential applications and use cases of integrated photonics (other than high-speed fiber communications and beamforming) have been demonstrated. Integrated photonics has been demonstrated in biological sample detection [15], motion sensors such as integrated photonics gyroscopes [16], coherent imaging [11], photonics beamforming [17], lens-free incoherent imaging [18], [19], quantum key distribution [20], and deep learning [21] applications. Compared to integrated electronics, integrated photonics is still in its early stages. The largest current WDM systems for data communication or integrated photonic beamformers comprise of a few thousand integrated components much simpler than their electronics counterparts.

In this thesis, systems and architectures that improve integrated photonic systems beyond the current performance, density, and complexity limitations are explored. Application areas such as LIDAR, remote sensing, and imaging applications are examined, and architectures for large-scale, high-resolution, and high sensitivity wave processing are proposed. Integrated coherent image-processing techniques for high-sensitivity, high-resolution, and high dynamic range imaging are explored. Finally, several architectures for improved high-speed signal modulations for high-density and high-complexity photonics integration are proposed.

1.1 Contributions

Solutions for scalable, high-resolution, and low-power integrated photonics beamformers as a transmitter, receiver, or transceivers are explored. State of the art integrated beamformers achieve large FOV beamforming at the expense of requiring a stable and widely tunable laser, while OPAs with a low-cost single laser suffer from a limited FOV. Moreover, interconnect density between integrated electronics and photonics sub-systems limits the achievable integration density and complexity. We proposed two integrated beamformers to address these issues.

First, we demonstrated a novel 2D transceiver with an electronically steered beam that can operate with a fixed-wavelength, low-cost laser. This architecture simplifies the system implementation and offers better scalability without sacrificing beamwidth or the FOV. It has the same beamwidth as an $N^2 \times N^2$ element array beamformer with only $N \times N$ radiators. The field-of-view (FOV) of this aperture is limited by the radiating element and not the phased array architecture itself. Furthermore, our proposed architecture addresses the interconnect density challenge by requiring only $2N$ interconnects between the electrical driver and the photonic sub-system to control $N \times N$ radiators independently. This architecture resolves $3\times$ more points than our previous demonstration [22] with the same number of radiators and phase shifters. Second, we demonstrated another novel transmitter beamformer architecture that operates at a single frequency and achieves 2D beamforming through electronic control. This architecture is inspired by the diffraction pattern of the annular ring and offers low side-lobe levels. The system FOV is limited by the radiating elements FOV and not the proposed array.

In addition, we explored coherent imaging systems for ranging, remote sensing, and medical imaging application. Our proposed coherent imager eliminates several limitations of our previous work [11]. The previous generation's coherent imager suffers from a low dynamic range and slow signal acquisition speed due to the system's random optical phase fluctuation. This system resolves those problems by making the system output signal insensitive to optical path phase fluctuations and suppresses undesired signals. Furthermore, similar to driver interconnect challenges in integrated beamformers, this work had a similar limitation in terms of the scalability of the aperture since the required electrical routing will increase inter-element pitch and reduce the resolution of the resulting image. We proposed a novel readout architecture that reduces the number of electrical interconnects for an $N \times N$ pixel imager from N^2 to $2N$.

For data communication applications, solutions for low insertion loss, low drive voltage, and compact drivers are explored. Conventional integrated high-speed silicon photonics modulators require a large drive voltage and have a large chip footprint. We present five designs that reduce the footprint needed for complex signal integration. Three electro-optic modulators are proposed that reduced the footprint of the integrated high-speed modulator. Another high-speed electro-optic modulator is proposed based on silicon-organic-hybrid (SOH) modulators that decouple loss and index modulation and are used for high-speed, high-performance system design. A complex waveform modulator and two high-speed integrated OPAs of 4 elements and 128 elements are implemented. Finally, a multi-ring resonator architecture is proposed that reduces drive voltage requirements for high-speed amplitude modulation in a small footprint.

1.2 Thesis Outline

In the following chapter, a brief overview of the integrated photonic platform is given. Various components and sub-blocks available in the process crucial to understanding the operation of the blocks and system in the subsequent chapters are introduced. The prospects of this platform for high-density integration are examined.

Chapter 3 examines integrated photonics beamforming challenges and introduces the co-prime photonics beamforming transceiver architecture. It analyzes the performance limitation of existing solutions and how this architecture addresses them. A silicon photonics implementation is designed and measured, demonstrating grating-lobe-free beamforming. An improved version of this co-prime array is designed that addresses some of the shortcomings of the previous system. Chapter 4 introduces the annular ring OPA inspired by the diffraction pattern of a continuous annular ring aperture. A silicon photonics implementation is designed and measured, demonstrating 2D beamforming.

Chapter 5 investigates the challenges with current coherent imaging systems and proposes an architecture to address several fundamental challenges. An expandable aperture design is proposed, implemented, and tested. Coherent FMCW ranging is demonstrated.

Chapter 6 through 8 propose three electro-optic modulators that improve on-chip footprint and drive voltage requirements of the high-speed modulators. In Chapter 9, current solutions for modulation in a silicon photonics platform are explored. Silicon-organic-hybrid modulators are investigated, and integrated silicon photonics

systems are designed using this modulator. Finally, in Chapter 10, a multi-stage ring-assisted MZI amplitude modulator is designed and implemented in a silicon photonics platform that reduces the drive voltage requirements for modulation in a compact footprint.

Chapter 2

SILICON PHOTONICS INTEGRATION

This chapter gives a brief overview of silicon photonic integration. Current platforms for silicon photonic integration are presented. The building blocks for photonic integration for signal processing and photonics wave manipulation are presented. Several examples of high-density photonic systems for data-communications applications are investigated. Limitations of integrated photonics platforms in solid-state beamforming are considered.

2.1 Silicon Photonics Platform

Large-scale photonics integration is a function of the performance of the available photonics components and the accessibility of those devices to integrated electronics that control and co-process the optical signal. Based on these two criteria, three approaches to silicon photonics integration are presented. Dedicated photonic processes [23] offer minimal electronic components. This photonic circuit needs to be co-integrated and co-packaged with an external electronics chip for control and sensing. This approach results in high-performing electronics and photonics components and enhanced system performance, and many industrial applications operate using this approach [24]. However, for high-speed applications, the parasitics of the interconnects limits the system performance. Furthermore, applications that require a very large number of interconnects between the two systems become impractical.

On the other hand, electronics SOI processes can be used to create integrated photonic waveguides and incorporate various photonics devices, including germanium photodetectors [25]. These platforms are ideal for systems in which the photonics circuit complexity is limited. While the integrated electronics perform ideally and interconnect-density and parasitics limitations are removed, the photonics components operate sub-optimally and typically with higher losses than dedicated photonics platforms [26]. Recently developed, hybrid monolithic platforms with high-performing electronics and photonics components can be used for complex electro-optic system integration without suffering from interconnect density and parasitics-related limitations [27], [28]. These monolithic solutions are more expensive than individual electronics or photonics processes since all components

need to be co-fabricated, resulting in fabrication complexity. In addition, given the large footprint of photonics devices compared to electronic, hybrid integrated systems are typically dominated by the integrated photonics components. Therefore, the reduced interconnect parasitics and integration density must pose an operational bottleneck for these monolithic solutions to make sense economically.

2.2 Silicon Photonic Devices

Currently, integrated photonics platforms offer a wide range of components that allow for optical wave manipulation and linear signal processing. This includes electro-optic modulation to modify the optical signal and photodetector that can be used for optical power detection and can act as photonics mixers (Fig. 2.1).

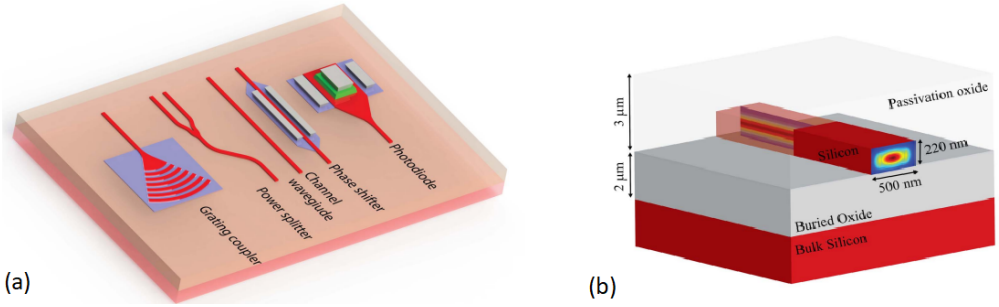

Figure 2.1: Silicon photonics platform. (a) Devices available for silicon photonics integration. (b) Optical mode confinement in dielectric waveguides [17].

Photonics Signal Routing, Distribution, and Chip-Coupling

Similar to optical fibers, an integrated photonic platform offers signal routing and distribution by using dielectric waveguides, sandwiching a high refractive-index core material inside a low refractive-index clad materials [29]. Given the maturity of silicon photonics fabrication processes, photonics waveguide structure on one or multiple layers can be fabricated reliably with low loss [30]. Currently, metallic photonic waveguides have a very high propagation loss and have very limited applications [31]. Leaky guided-modes where the light is confined in the lower index region have also be demonstrated for photonics modulation [31].

These dielectric waveguides can be used for signal routing across the chip between different system sub-blocks. Signals can be divided using evanescent-based directional couplers, MMI interferometers, y-junctions, and adiabatic couplers [32]. Interfacing with a photonics chip via an optical fiber or free-space requires the electromagnetic design of mode couplers. Grating-based couples allow for an efficient

chip to fiber coupling [33]. Tapered waveguides terminated at the side of the chip [34] can be used to efficiently interface with lensed fiber. The larger the number of photonics layers, the higher the coupling efficiency and the higher the system's tolerance to misalignment [35].

Photonics Signal Modulation and Detection

Photonics signals can be modulated electronically with integrated amplitude and phase modulators. Amplitude modulation is achieved by increasing the absorption in the integrated waveguide. Some of these modulators are very compact and can operate in GHz frequencies [36]. The phase of the photonic wave can be modulated in a variety of ways including with thermo-optic effect [37] and electro-optic effects. Electro-optic effects can be broken down into two groups: those operating based on plasma-dispersion effect [38] and those operating based on the Pockel's effect [39]. A complete overview of the advantages of disadvantages of various integrated modulators is included in Chapter 9.

Photonic signal detection is achieved via integrated photodetectors. In silicon photonic platforms with operation wavelength ranging from the O-band to C-band, germanium is the material of choice. The type of the photodiode device determines the sensitivity as well as the speed of these modulators [40], [41].

2.3 High-Density Photonics Integration

Silicon photonic devices mentioned in the previous section have been utilized for high-complexity and high-density electro-optic system integration. Multi-channel high-speed silicon photonics transceivers capable of modulating electrical signal on several optical frequencies and receiving and processing high-speed signals at high data-rates have been demonstrated [42]. The large-scale silicon-photonic switch matrix with nanosecond-scale reconfiguration time-scale has also been explored [27] for fiber-based router application. For photonics beamforming applications, complex systems with thousands of photonics components [43], [44] have demonstrated one-dimensional, electronically-controlled beamforming. Fully reconfigurable beamforming in two dimensions for complex free-space waveform generations has also been demonstrated for a limited field-of-view [10], [45]. The challenge with achieving a large field-of-view beamforming is that it is required that the free-space-to-chip couplers be closely packed at half-wavelength spacing. The dielectric nature of the integrated photonics components prevents such arrangement of components, and greater than half-wavelength spacing cannot be avoided. Novel integrated signal

processing approaches are required to overcome these limitations.

Chapter 3

COHERENT OPTICAL TRANSCEIVER BASED ON CO-PRIME SAMPLING

A solid-state, optical phased-array transceiver based on co-prime sampling techniques is proposed. This architecture does not trade-off FOV with beamwidth due to 2D routing limitations, which is what impedes aperture scaling in uniformly spaced transceivers. Furthermore, compared to standard $\lambda/2$ transceivers, which require $O(N^2)$ elements to resolve N pixels in the far-fields with a given resolution, this beamforming architecture can capture a coherent image with the same resolution and pixel count with $O(N)$ elements. In one SiP implementation, a co-prime transceiver using an 8x8 transmitter OPA and an 8x8 receiver OPA has been designed and implemented to demonstrate beamforming capability of this architecture. In another implementation, a co-prime transceiver using an 8x8 transmitter OPA and an 8x16 receiver OPA has been designed and tested to demonstrate transceiver ranging[1].

3.1 Introduction

Integrated optical beamforming and image processing has many applications ranging from point-to-point optical communications, 3D imaging, LIDAR for airborne imaging and autonomous vehicles, compact, lens-free projection systems, lens-free imagers, holographic recording, and projection. In conventional optical systems, image processing and reconstruction is achieved using discrete optical elements such as lenses, mirrors, and beamsplitters, and beamforming and scanning is done using mechanical stages. This adds to the cost as well as the complexity of the system. On the other hand, integrated photonic platforms allow for high-density integration of photonic components resulting in a smaller size and increased system complexity. The theoretical potential of optical beamforming was inspired by its RF and microwave counterparts [46]–[48] and early demonstrations of optical beamforming date back to the early 1960s-70s [1,2]. In fact, several integrated photonic beamforming systems have been demonstrated [5]–[7]. On the other hand, the emergence of CMOS-compatible silicon integrated photonics has allowed for the realization of integrated photonic beamforming at lower costs with improved yield using silicon-based dielectric waveguides and radiators [10], [12], [45]. Vari-

[1]This work was done in collaboration with Reza Fatemi.

ous sub-systems for improving the performance of integrated optical beamformers such as high-efficiency integrated modulators [43], [49], high-efficiency radiating elements [50], [51], and integrated on-chip calibration [52] have been proposed.

The trend in SiP OPA integration for greater than one hundred radiating element is to place radiating elements on a one-dimensional grid and beamforming in one dimension using integrated phase-shifters. Beamsteering in the orthogonal direction is achieved using long and wavelength sensitive grating couplers [50] by sweeping the wavelength of the laser. Very large arrays of 512 to 8192 radiating elements in a one-dimensional array have been demonstrated in the past [43], [53], [54]. This architecture is referred hereon as **1D-OPA**, while architectures that have radiating elements placed on a 2D grid are referred to hereon as **2D-OPA**. 1D-OPA architectures have several shortcomings. This architecture requires a widely tunable and low linewidth laser, which adds to the cost and system complexity. The wavelength tunability requirements for this type of phased array is 100nm or more [55]–[58]. At the extreme case, a class of phased arrays requires only a tunable source for beamsteering called serpentine arrays [59], [60]. This architecture also requires over 100nm of wavelength tunability for beamsteering. Radiation beam-angle is very sensitive to the wavelength of the laser, and henceforth precise control of the laser wavelength and linewidth is required to control the beam direction. In addition, multi-beam operation using complex beamforming techniques and multi-wavelength operation without increasing the number of required sources is not possible with this method. This design choice primarily rises from the dielectric nature of the optical waveguides as well as radiating elements in SiP OPAs. In this platform, the dimension of the waveguides and radiating elements are in the order of the wavelength and require sufficient spacing between these SiP devices to prevent undesired coupling between individual signal lines via waveguide and between radiating elements. In a planar photonic platform, a 2D-OPA requires a minimum spacing between radiating elements to allow for the signal to be routed to the radiators in the center of the radiator array (Fig. 3.1). On the other hand, creating large-scale integrated beamformers with a large field-of-view requires placing the elements at half-wavelength spacing. The fabrication limitation of planar OPA and the dielectric nature of placing the element at larger spacing reduced the usable field-of-view of the phased array. Previously demonstrated silicon photonic 2D-OPAs have a very limited FOV [10], [11], [45].

The trade-off between FOV and number of radiating elements for a typical scenario

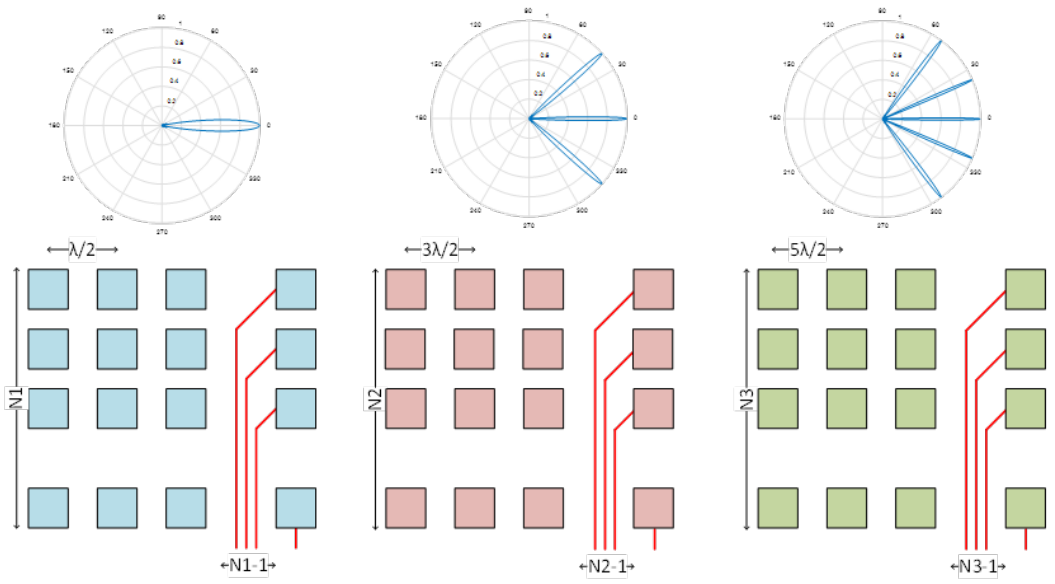

Figure 3.1: Routing optical signal to radiating elements in a 2D grid requires a larger inter-element spacing. $5\lambda/2$ element spacing results in less than 30° FOV.

of $2\mu m \times 2\mu m$ grating couplers, with $500nm$-wide waveguides and $1\mu m$ spacing between elements, is plotted in Fig. 3.2. If all waveguides are routed from a single side to the apertures for a 10×10 OPA, the field-of-view will have an upper bound of 2.3°. Even for an optimized routing where waveguides are routed through all 4 sides of the aperture, the FOV will have an upper bound of 6.2°. Furthermore, it can be seen that FOV gain for multi-layer routing diminishes for a given number of radiating elements. In the case of a two-layer photonics process with twice as many antenna feed paths, the upper bound of the FOV is 8.7°. Henceforth, uniform array beamforming architectures FOVs will be limited to less than 10° for a sufficiently large number of elements.

Several methods are developed to address this issue in 2D-OPAs. For example, the radiating element can be placed next to the phase and amplitude modulators for that radiator as a unit cell several wavelengths in diameter [10], [45]. This method trades the usable field-of-view of the integrated beamformer with the capacity for large-scale integration. Prior arts using this architecture have a limited FOV of a few degrees. Another challenge with these unit-cell-based OPAs is the power consumption of the phase shifter and amplitude modulator. Only thermo-optic (TO) modulators are sufficiently small enough to be integrated into the unit-cell, and static power consumption is required to maintain the desired phase and amplitude. Thus,

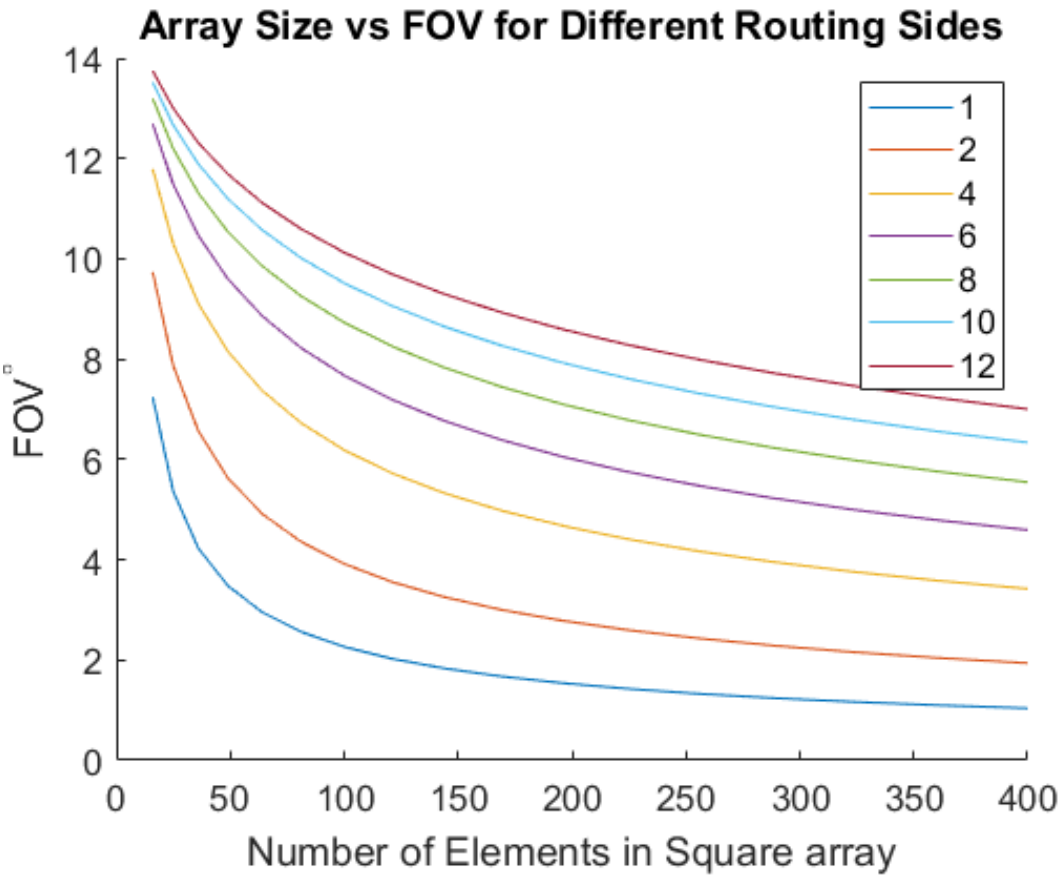

Figure 3.2: OPA FOV as a function of the number of elements in the array. A signal distribution waveguide pitch of $1\mu m$ and radiating element size of $2\mu m \times 2\mu m$ is assumed. The FOV is severely limited once the total number of elements in the array is above 50.

the power consumption of this architecture will scale with the aperture size, and heat management will become an issue. Another method to address the FOV and radiating element count trade-off is using sparse (thinned) arrays. This type of array has been previously constructed in RF and microwave domains for the purpose of reducing the number of required radiating elements and phase modulators. Thinned arrays, minimum redundancy arrays, vernier arrays, MIMO arrays, and nested arrays [46], [61]–[64] are a few examples of sparse architectures in RF, and some of these have been proposed and/or demonstrated for optical integrated phased arrays [17], [65]–[67]. The non-uniform element placement of the radiating elements in this array architecture achieves a narrow beamwidth without reducing the field-of-view with a fewer number of elements compared to the same number of uniformly spaced radiators. The trade-off in this architecture is between the number of radiating ele-

ments and the radiation efficiency (total power in the main beam) which is known as the array sparsity curse. Here, the projected power of the main beam is reduced and spreads in undesired directions. It is only the case in uniform sampling that the power of the main beam goes to equally spaced grating lobes, and the power in the side-lobes (scattered in undesired directions) is minimized. In RF and microwave beamforming, several architectures have been proposed to create a sparse array with deterministic spacing between radiating elements such as minimum redundancy arrays, MIMO arrays, nested arrays, vernier arrays, etc, all of which can be applied to SiP OPAs. The design choice for an optical beamforming method should optimize the required number of radiating elements, achieve superior beamforming performance, and address the planar routing constraints of the SiP platform. More importantly, laser sources are the dominant source of power consumption in SiP integrated systems, and optical amplifiers are inefficient compared to their electronics counterparts. As a result, power management is very critical. Therefore, beamforming methods that have efficient beamforming with uniformly spaced elements and apodized amplitude that utilizes analog array gain are preferred. Also, complex optical modulators with high insertion loss are less desirable.

Transceiver arrays utilizing co-prime beamforming techniques are one method that satisfies all these requirements. Co-prime beamforming is achieved by placing transmitter array elements in a uniform grid with an inter-element spacing d_{TX} and receiver element with uniform inter-element spacing of d_{RX}, where d_{TX} and d_{RX} are co-prime with respect to each other. These uniform arrays only require basic phase and amplitude control and offer array gain before amplification and hence have SNR advantage. Half-wavelength spacing is not required between radiating elements, and henceforth, 2D routing constraints are relaxed. Furthermore, mutual coupling between the radiating elements is reduced [68]. Finally, the co-prime sampling technique offers an optimum number of radiating elements for a given transmitter and receiver inter-element spacing. It is shown that with $O(N)$ beamforming elements, it is possible to achieve $O(N^2)$ resolvable points (PPV). This system allows multi-beam operation for imaging by incorporating multiple receivers or a multi-beam receiver. This system achieves a quadratically larger resolvable spot compared to its radiators without sacrificing SNR and field-of-view. The background formulation of co-prime sampling is explained in Section II, the design of two co-prime OPAs are described in Section III, measurement in IV, and discussion in V.

3.2 Background Formulation for Co-Prime Sampling

Co-prime sampling, which is a sparse signal processing method for beamforming, was proposed in 2010. The concept is first explained from a sampling theory perspective. A more detailed explanation including proofs and derivations can be found in [69],[70].

Aliasing-free reconstruction of a far-field radiation pattern from its spatial samples is analogous to computing the auto-correlation of function from discrete samples. Here the auto-correlation of a signal is calculated by co-prime sub-sampling of the function at lower rates. The simplest way to sample the auto-correlation of a continuous wide-sense stationary function $x_c(t)$ is to sample it uniformly at T intervals resulting in $x[n] = x_c(nT)$ and compute the auto-correlation directly.

$$R_{xx}(k) = E[x[m]x^*[m-k]] = 1/M \sum_{m=0}^{M-1} x[m]x[m-k] \tag{3.1}$$

Since the signal is WSS, it is shown in [69] that one can alternatively sample $x_c(t)$ twice at a lower rates of NT and MT and get $x[n_1] = x_c(n_1NT)$ and $x[n_2] = x_c(n_2MT)$. If N and M are co-prime numbers with respect to each other, then the correlation of the two samples $R_{xy}(k)$ can be expressed in the difference form as

$$R_{xy}(k) = E[x[n_1N]x^*[n_2M]] = R_{xy}(k) = E[x[n]x^*[n-k]], \tag{3.2}$$

where $k = n_1N - n_2M$. [70] shows if N and M are co-prime, then there exists a set of integers n_1 and n_2 that can be used to compute all integers k. In the aforementioned work, this is referred to as a **difference co-array**.

This concept can be extended to beamforming applications, as explained in Fig. 3.3 and Fig. 3.4. Assuming there are 12 discernible directions, the far-field can be sampled using a transmitter array with element spacing of 3d and a receiver array with element spacing of 4d. The transmitter array will have 4 grating lobes sampling 4 out of 12 resolvable spots, and the receiver array will have 3 grating lobes sampling 3 out of 12 resolvable spots, which will result in aliasing if they are individually used to sample the far-field. However, as a transceiver, the pattern of the transmitter and the receiver multiply, resulting in a single resolvable spot. The phase of the transmitter and the receiver individually and with respect to each other can be shifted to collect power from all 12 resolvable spots at the same time.

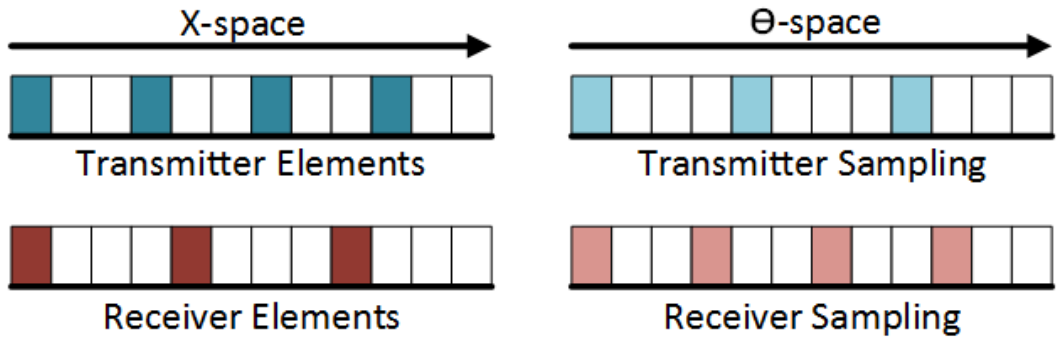

Figure 3.3: Co-prime sampling in spatial domain and the equivalent spectral samples.

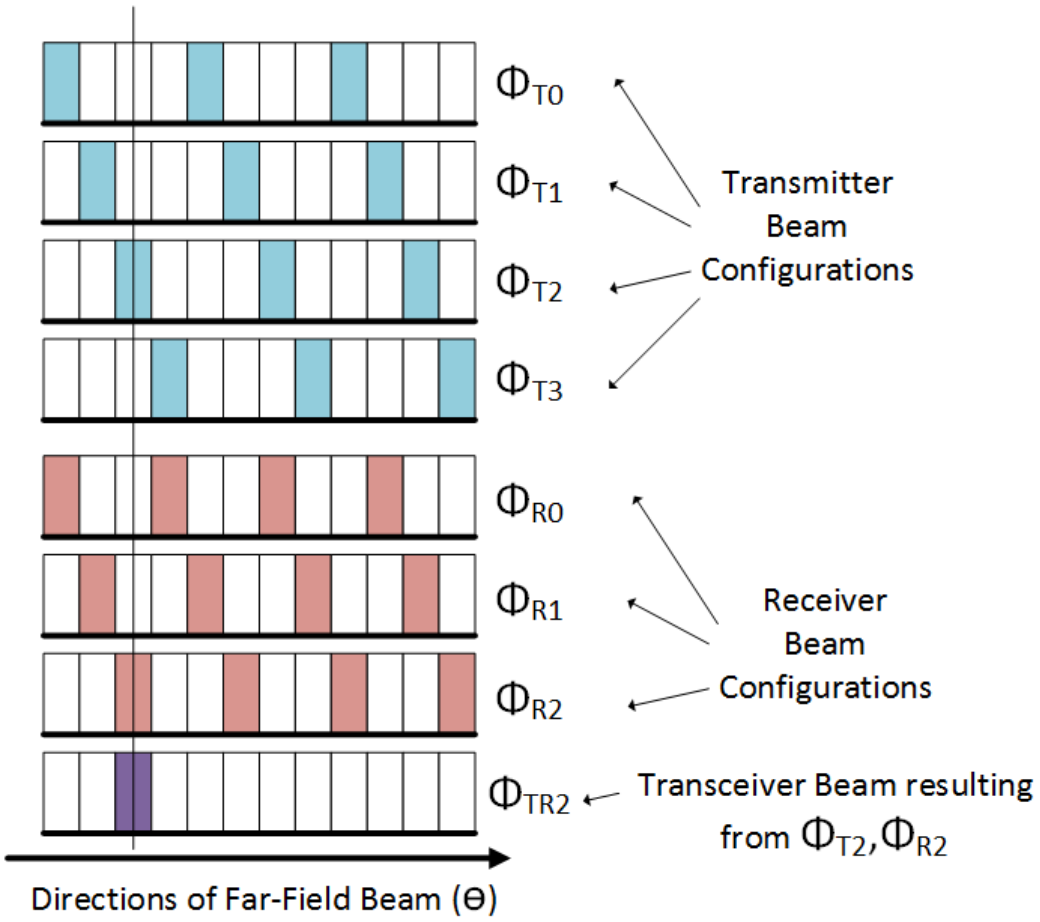

Figure 3.4: Co-prime sampling.

A general formulation for an active transceiver-based phased-array beamforming is

given by

$$E_{TRx}(\theta, \theta_{Rx}, \theta_{Tx}) = E_{Rx}(\theta, \theta_{Rx}) * E_{Tx}(\theta, \theta_{Tx}) * \rho(\theta), \tag{3.3}$$

where θ is the beam direction with respect to the normal, ρ is the complex reflectance

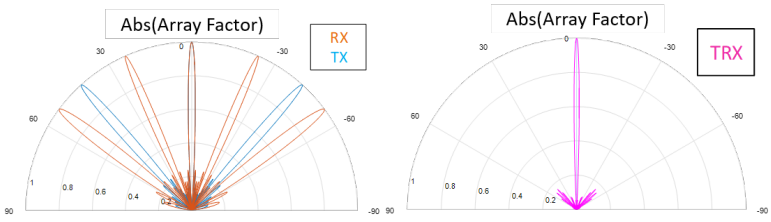

Figure 3.5: Co-prime beam pattern multiplication.

of the target, and θ_{Tx} and θ_{Rx} are the transmitter and receiver active beamforming directions, respectively. For systems where the transmitter or receiver has a single receiving/transmitting element, the corresponding term in the equation above will simplify to unity. Using co-prime numbers 3 and 5 and unit spacing of $\lambda/2$, the beam pattern for such transmitter and receiver pairs and the resulting co-prime transceiver array is visualized in Fig. 3.5. Array factor for individual phased arrays can be written in the general case of a phased array in one-dimension with N elements placed randomly across a line with variable amplitudes. The radiating pattern, also known as array factor, can be formulated as

$$AF(\theta, \theta_d) = \sum_{n=0}^{n=N-1} a_n \times e^{jkd_n(\sin(\theta)-\sin(\theta_d)))} \tag{3.4}$$

Although a non-uniform set of amplitudes [71] as well as non-uniform spacing [65] can improve the performance of a phased-0array, they are omitted in this analysis for simplicity. All of the radiating elements are fed with a normalized constant amplitude of $1/N$ and are placed uniformly at $d_n = nd_0$. Therefore, the simplified formula for the far-field radiating pattern amplitude, or array factor (AF), is given by

$$AF(\phi) = \frac{e^{j\phi/2(N-1)}}{N} \times \frac{sin(N\phi/2)}{sin(\phi/2)}, \tag{3.5}$$

where

$$\phi = kd_0(\sin(\theta) - \sin(\theta_d)) \tag{3.6}$$

As mentioned earlier, in integrated 2D-OPAs $d_0 > \lambda/2$ will result in grating lobes. For inter-element spacing of $d_0 = M\lambda/2$ the direction of the main radiating lobe and grating lobes, denoted by θ_M, are located at the solutions of $\sin(\theta_d) - \sin(\theta_M) =$

$2k/M$ where $-M/2 < k < M/2$ is an integer [48]. $k = 0$ is the location of the main beam ($\theta_d = \theta_M$) while $k \neq 0$ denote the grating lobes. If $M > 1$, there is more than a single solution to this equation, which results in grating lobes. For a transceiver array with N_{tx} elements with d_{tx} spacing and N_{rx} elements with d_{rx} spacing, the array factors of the transmitter and receiver multiply and can be written in a form similar to [3.3] as shown in Fig. 3.5.

$$AF(\phi_{rx}, \phi_{rx}) = \frac{e^{j(\phi_{rx}-\phi_{tx})/2(N-1)}}{N_{rx}N_{tx}} \times \frac{sin(N_{rx}\phi_{rx}/2)}{sin(\phi_{rx}/2)} \times \frac{sin(N_{tx}\phi_{tx}/2)}{sin(\phi_{tx}/2)} \tag{3.7}$$

In this scheme, the inter-element spacing between the transmitter elements $d_{tx} = Q\lambda/2$ and the receiver elements $d_{rx} = P\lambda/2$ are co-prime numbers with respect to each other within a constant factor of $\lambda/2$ ($\nexists k \in Z, P = k \times Q$). In this case, the location of the main and grating lobes (assuming that both arrays are pointing in the same direction $\theta_d = \theta_{Rx} = \theta_{Tx}$) are at the solutions of the system of equations given by (3.8) and (3.9).

$$\sin(\theta_d) - \sin(\theta_{Mtx}) = 2k_1/Q \tag{3.8}$$

$$\sin(\theta'_d) - \sin(\theta_{Mrx}) = 2k_2/P \tag{3.9}$$

It is shown in [70] that the grating lobes of the two arrays only overlap in a single point ($\theta_{Mtx} = \theta_{Mrx}$) for co-prime values of P and Q. The larger the number of transmitter and receiver array elements, the smaller the side-lobe levels. An important aspect of using co-prime sampling for photonic beamforming is that increasing the co-prime array size by choosing larger co-prime numbers P and Q results in even larger inter-element spacing, which simplifies the routing even further.

3.3 Design

To demonstrate co-prime beamforming capability, two variants of SiP co-prime transceivers were designed and implemented using AMF CMOS photonics foundry. First, an 8x8 transmitter and an 8x8 receiver with equal power distribution between transmitter and receiver elements are used to demonstrate co-prime beamforming capability. Afterward, a larger 8x8 transmitter, in conjunction with an 8x16 receiver with an integrated transmitter and receiver modulators and amplitude control for the receiver aperture, is designed and implemented to enhance sensitivity for transceiver operation and FMCW ranging.

Design A: 8x8 Transmitter/8x8 Receiver

The block diagram of the chip is shown in Fig. 3.6. The chip comprises a transmitter OPA and a heterodyne receiver OPA with an inter-element spacing and radiating

element count that satisfy co-prime beamforming conditions. 8 transmitter elements with an inter-element spacing of $9.2\mu m$ and 8 receiver elements with inter-element spacing of $12.4\mu m$ with operational wavelength of $1.55\mu m$ result in 6λ spacing for the transmitter and 8λ spacing for the receiver. Hence, the patterns are co-prime with respect to each other within a factor of 2. Therefore, grating-lobe free operation FOV for this transceiver will be 30° larger than the FOV of the individual apertures. Light is coupled into the chip using a fiber grating coupler. A Y-junction splits the input light equally into the transmitter beamforming block for target illumination and as the reference signal for receiver beamforming and homodyne mixing.

There are two 8x8 phase modulator blocks corresponding to the transmitter and receiver OPAs. A Y-junction tree splitter divides the power equally among 64 radiating elements. 64 thermo-optic phase shifters in the path of each radiating element adjust the relative phase between the radiating element for electronic beamforming. The phase shifters are driven in a row-column fashion with only 16 electrical connections for 64 phase shifters. Therefore, only $2N$ electrical connections are required for $N \times N$ phase shifters. The phase adjusted light radiating through 64 nano-photonic radiators, and a beam is formed in the far-field distance of the transmitter array. The beam reflects off the target and is collected by 64 nano-photonic radiators identical to the transmitter ones. The receiver array is configured as a homodyne receiver with LO path phase-shifting. The receiver array's relative phases are adjusting by tuning the phase shifters placed in the LO reference path rather than the signal path to improve receiver SNR. Similar to the transmitter path phase shifters, the receiver phase shifters are also placed in a row-column matrix format requiring only 16 electrical connections for 64 phase shifters. The received and LO signals are mixed using 50/50 directional couplers and balanced detectors. The output signal of each balanced detector is shown in (3.10). Beamforming signal gain is achieved by adding all the output currents of the 64 balanced detectors. The output of the array as a function of (θ, ϕ) is shown in (3.11).

$$I_{BDij} = R\sqrt{P_{LO}P_{Rx,ij}}cos(\Delta\phi_{ij}) \tag{3.10}$$

$$I_{output}(\theta,\phi) = \sum_{i,j=1}^{8,8} R\sqrt{P_{LO,ij}P_{Rx,ij}}cos(\Delta\phi_{ij}) = 64R\sqrt{P_{LO}P_{Rxtotal(\theta,\phi)}} \tag{3.11}$$

The design of the thermo-optic phase shifter and electrical drive circuitry, the radiating element, co-prime transmitter and receiver beamforming performance, and on-chip control units are detailed in the next 4 sub-sections.

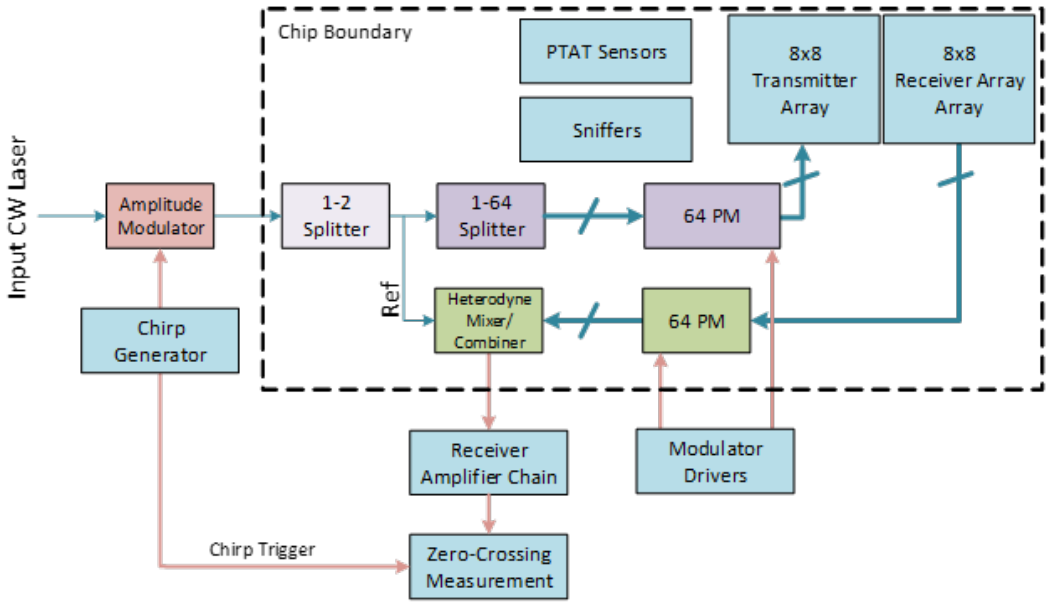

Figure 3.6: Block diagram of design A: Integrated phase shifters adjust the phase of the transmitter and receiver OPAs independently. The return signal is mixed using balanced heterodyne detectors on-chip. The relative phase of the received and LO signals are adjusted in the reference path to improve receiver sensitivity. FMCW amplitude chirp for ranging is applied externally.

Compact Spiral Thermo-Optic Phase Shifter

After an equal split of the transmitter power into 64 paths, the optical phase is adjusted using an 8x8 array of thermo-optics (TO) phase shifters (TOPS). The TO phase shifter unit is a co-spiral silicon resistive slab-heater and a silicon waveguide of 350μm (Fig. 3.7). An oxide trench encloses individual phase shifters, which helps with the thermal isolation. The resistive slab-heater comprises of four resistors in parallel, which improves modulator design fidelity toward process variations and failures. Thermal modulation simulation of the phase shifter shows that for 20mW power delivered via the resistive heater and good substrate thermal contact, there is minimal cross-talk between the elements.

All phase-shifters in one row and all phase shifters in one column share a common electrical connection resulting in a total of 8 row signals and 8 column signals for the transmitter and the same for the receiver (Fig. 3.8). A series of dummy heaters were included in the row-column heater matrix to balance the heat gradient across the chip, increasing the electrical connections from 8 rows to 9 rows. The row-column are driven via pulse amplitude modulation (PAM) drivers, which program one column of thermal phase shifters at a time (Fig. 3.9). The thermal modulators have a

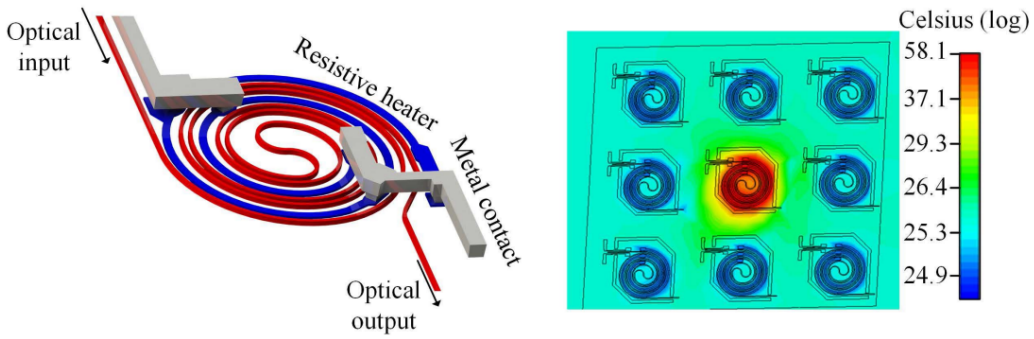

Figure 3.7: Compact spiral thermo-optic phase shifter (left). An oxide trench surrounds the radiators and reduces the cross-talk between adjacent phase-shifters. Thermal simulation of the cross-talk between the elements (right).

time-constant in the order of 10ms. The row-column driver circuit continuously re-programs the TO phase-shifter columns at MHz frequencies. This allows all TO phase shifters to maintain a particular phase value on average. This scheme allows for independent control of all phase shifters in the matrix of NxN TOPS with only 2N+1 (+1 for the dummy heaters in the matrix) electrical connections. This significantly reduces the interconnect between the driver circuitry and the photonic chip.

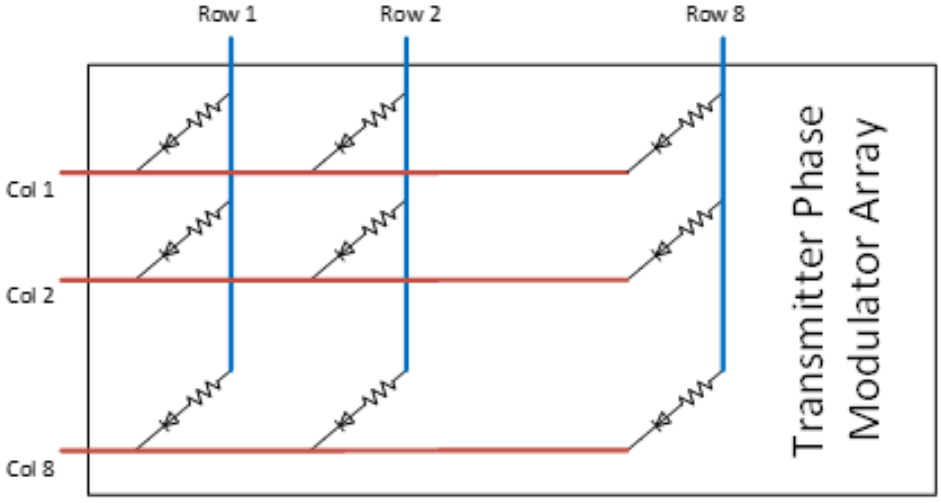

Figure 3.8: Electrical routing of the thermo-optic phase shifters. Phase shifters are placed in a row-column fashion which allows programming 64 phase shifters with 16 drive nodes.

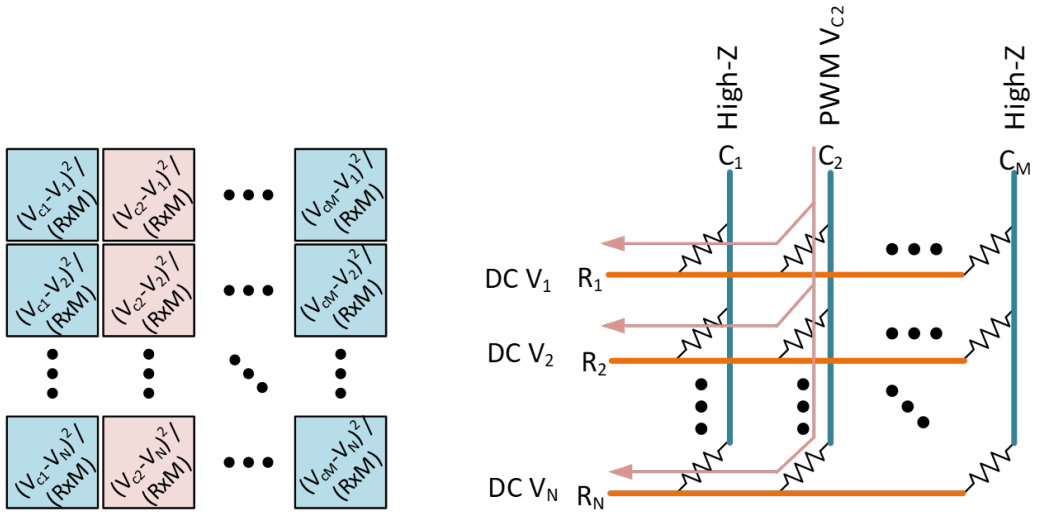

Figure 3.9: PAM programming of the thermo-optic phase shifter matrix. Each of the M columns draws current $1/M$ fraction of the cycle.

Co-Prime Radiating Element

A compact $2\mu m \times 5\mu m$ radiating element was optimized and implemented as the transmitter and receiving element (Fig. 3.10). This compact radiator has a 3 dB beamwidth of 22° with over 50% peak radiation efficiency at $1.47\mu m$ of wavelength. The 1 dB spectral bandwidth of the radiator was over 400 nm, making the radiators very robust to operation wavelength. The compact size of the radiating elements allows for the inter-element spacing of $9.2\mu m$ for the 8×8 radiating array in the transmitter OPA and $12.4\mu m$ for the receiver OPA. This dense integration required the radiating element to be placed in close proximity to the waveguides routing signals. This would result in the electromagnetic coupling between the radiating element and the adjacent routing waveguides that would disturb the radiation pattern (Fig. 3.10). The distribution waveguides are included in the design and optimization of the radiating element to account for their effect.

Co-Prime Beamforming Performance

The transmitter and receiver inter-element spacing, as well as the beam pattern of the radiators, results in the co-prime beamforming capability of this architecture in a 30° field-of-view. Per formulation of 3.7 and the size of the radiating element, here $d_{TX} = 9.2\mu m$ and, $d_{RX} = 12.4\mu m$ are chosen with 8×8 elements, making $N_{TX} = 8$ and $N_{RX} = 8$ (2 more than minimum required value of 6). The beamforming

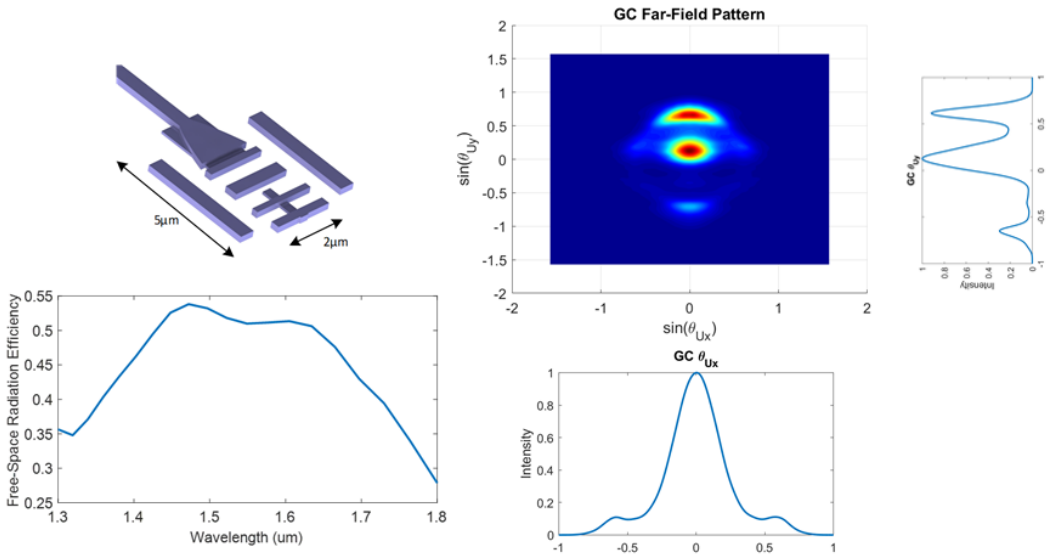

Figure 3.10: Far-field radiation efficiency and beamwidth of the radiating element.

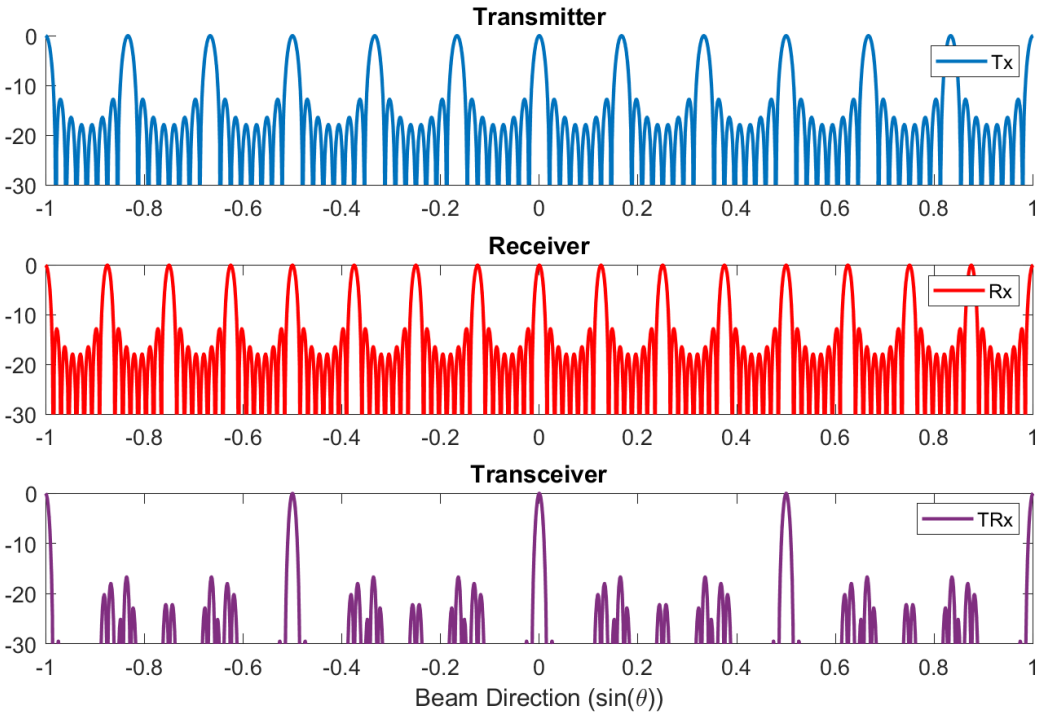

Figure 3.11: Design A OPA array factor for the transmitter, receiver, and the synthesized transceiver. While transmitter and receiver have 9.55° and 7.18° FOV, respectively, the transceiver can operate over a 30° FOV without any grating lobes and side-lobe levels below 15 dB.

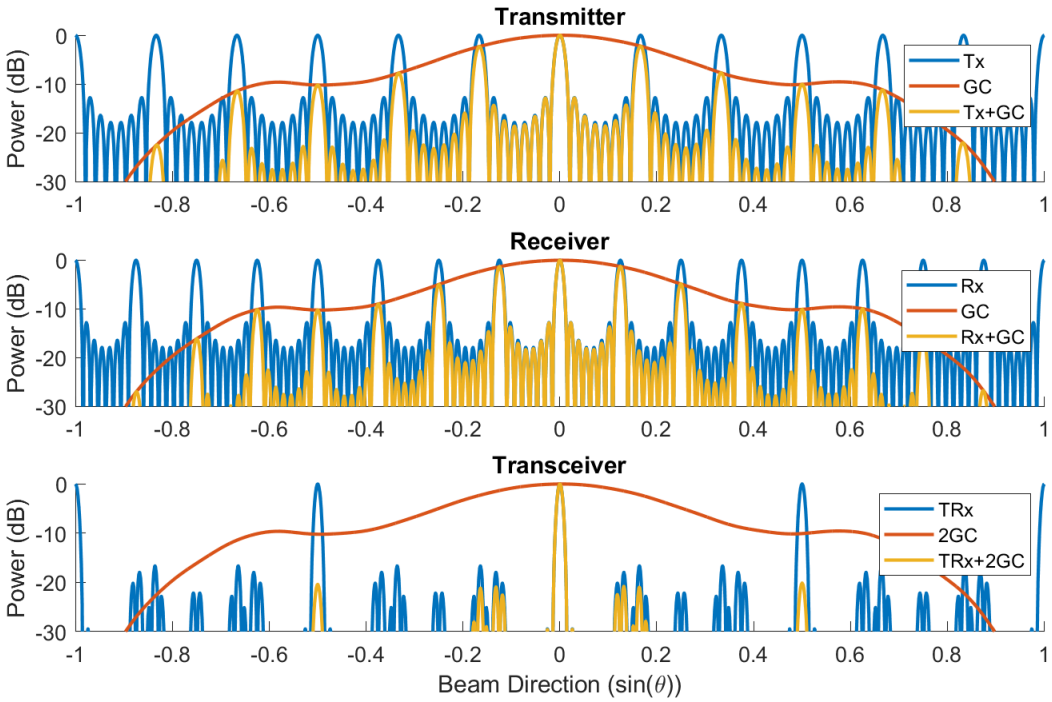

Figure 3.12: Design A OPA array factor including radiating element pattern. This results in a radiator-limited FOV of 22°.

performance assuming omni-directional elements is shown in Fig. 3.11. Finally, the combined effect of the transmitter and receiver along with the radiation pattern of the radiating element are considered, which showed a beamwidth of 0.64° with a FOV of 22° as shown in Fig. 3.12 and 3.13 which can theoretically resolve 1156 spots in the far-field with only 128 elements.

Co-Prime System Control

In addition to the dummy heater elements to remove temperature gradients across the phase shifter arrays, PTAT sensors are placed to monitor the relative temperature across the chip. Furthermore, sniffers were placed at the input of the system to monitor and calibrate for power fluctuations due to changes in laser intensity in power fluctuations in coupling to the chip. Moreover, a deep trench was included between the transmitter and receiver arrays to reduce the coupling of stray light between the transmitter and the receiver array.

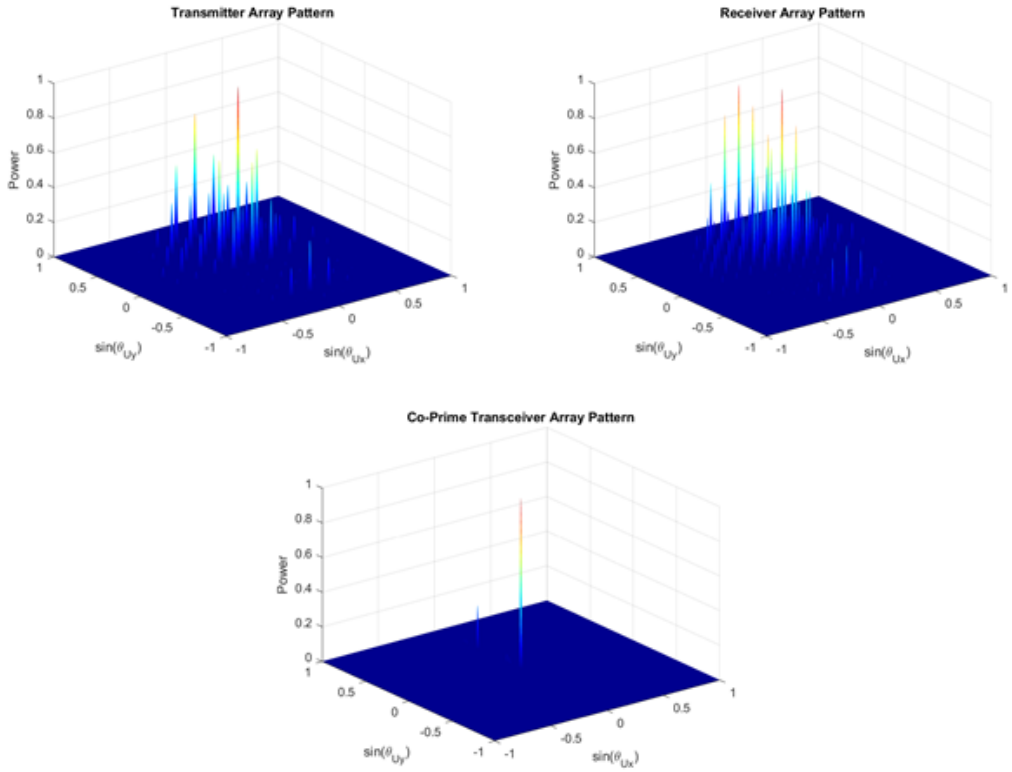

Figure 3.13: 2D radiation pattern of the transmitter and receiver and effective transceiver array.

Design B: 8x8 Transmitter/8x16 Receiver with Integrated Amplitude Modulators

The second iteration of the co-prime transceiver incorporates additional features to improve transceiver target detection sensitivity. A block diagram of the design is shown in Fig. 3.14.

The transmitter comprised of an 8×8 array of radiating elements that were placed with inter-element pitch of $d_{Txx} = 11\mu m$ and $d_{Txy} = 8\mu m$, with a compact $2\mu m \times 5\mu m$ radiators with peak efficiency of over 50% at $(\theta_x, \theta_y) = (0°, 9°)$. This resulted in a transmitter FOV of $(FOV_x, FOV_y) = (22°, 22°)$ and beamwidth of $(\theta x_{3dB}, \theta y_{3dB}) = (0.9°, 1.14°)$. The receiver comprised of 8×16 radiating elements that were placed at $d_{Rxx} = 28\mu m$ and $d_{Rxy} = 21\mu m$ spacing, with peak efficiency of 50% at $(\theta_x, \theta_y) = (0°, 9°)$. This resulted in a transmitter FOV of $(FOV_x, FOV_y) = (22°, 22°)$ and beamwidth of $(\theta x_{3dB}, \theta y_{3dB}) = (0.17°, 0.46°)$. As a consequence, the co-prime transceiver had a system FOV of $(FOV_x, FOV_y) = (22°, 22°)$ and beamwidth of $(\theta x_{3dB}, \theta y_{3dB}) = (0.16°, 0.49°)$, which resulted in a

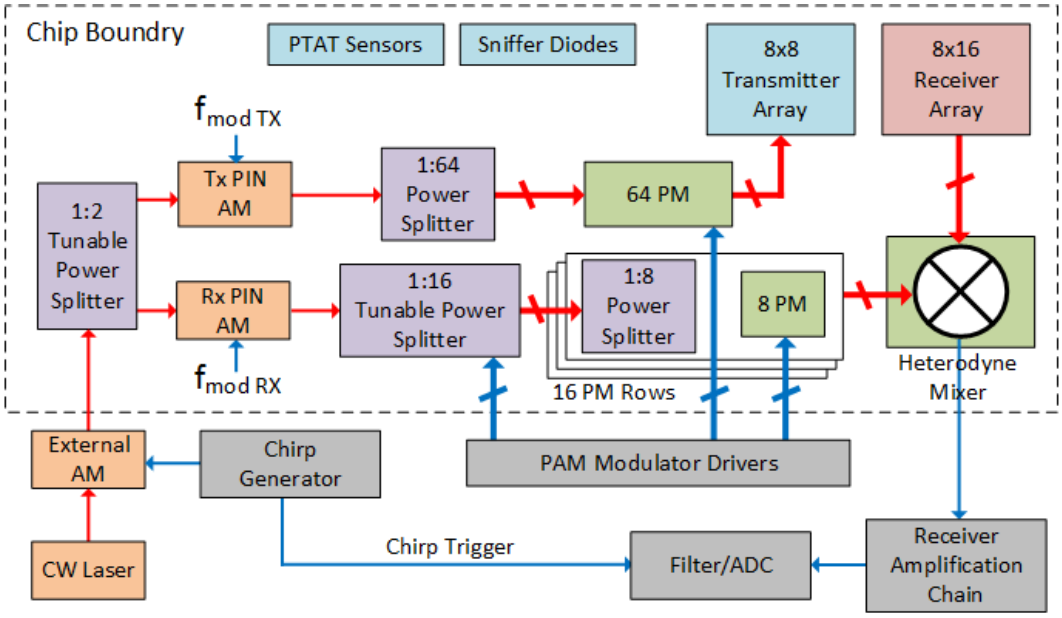

Figure 3.14: Block diagram of the second design. The number of radiators in the receiver is increased to 8x16 to improve the transceiver SNR. Integrated on-chip PIN modulators improve on-chip signal isolation and place strong LO chirp signal and the transceiver mixed-signal at different frequencies. Integrated tunable couplers in the receiver allow for apodized amplitude distribution, which further improves the receiver beam efficiency.

total of $137 \times 44 = 6028$ resolvable spots and highest SLL of -16 dB in the aperture FOV. Array beam pattern cross-section is shown in Fig. 3.15, and 2D beam patterns for the transmitter, receiver, and transceiver are shown in Fig. 3.16. The effective aperture of the receiver grating element was $4\mu m^2$, which, in conjunction with double the number of receiver elements compared to the first design, has 4 times more power collection capability. The design also included a tunable coupler to optimize the power distribution between the transmitter and receiver array. The nonlinearity of the silicon waveguides as well as total heat dissipation capacity of the silicon photonics platforms limits the total input power into the transceiver P_{tot}. This power needs to be shared between the transmitter array for illumination and the receiver array for LO path beamforming and homodyne detection. However, the LO path receiver's power can be limited to making shot noise the dominant noise source in the receiver, and the rest of the power can be diverted to the transmitter to improve system SNR. Hence, (3.12) and (3.13) need to be optimized based on the detector dark current as well as receiver chain noise sensitivity.

$$P_{tot} = P_{Tx} + P_{LO} \tag{3.12}$$

$$SNR = \alpha R^2 P_{Tx}/(2qR + (I_{dark}^2 + I_{elec}^2)/P_{LO}) \tag{3.13}$$

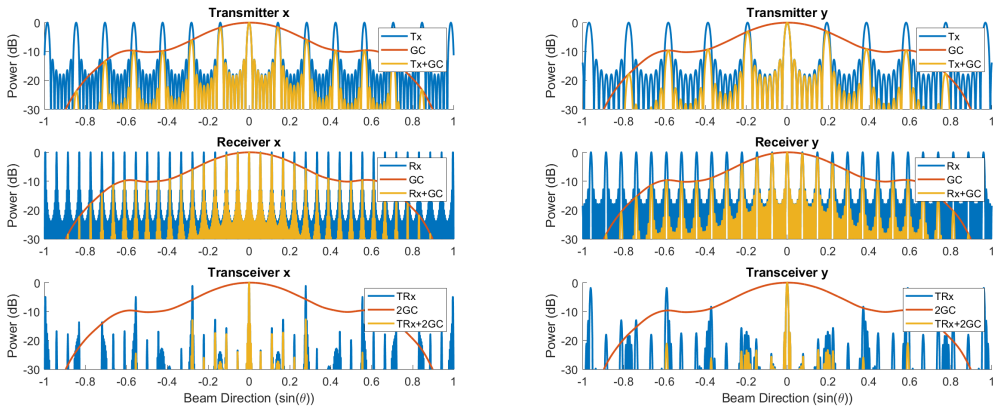

Figure 3.15: Radiation pattern cross-section for the transmitter and receiver and effective transceiver array including the effect of the grating couplers.

Integrated transmitter and receiver PIN modulators are implemented in the transmitter and receiver paths to allow for heterodyne detection of the target and isolation of the stray light that impinges on the receiver detector array from the laser coupling node to the OPA chip. A series of tunable directional couplers are set as a cascade of adjustable amplitude controls for the receiver array to allow for improved beamforming with nonuniform amplitudes for different columns. Cascaded amplitude modulator architecture conserves the total energy distributed between the different branches compared to a dedicated amplitude modulator per path, which radiates a fraction of the input power to achieve amplitude control. Furthermore, the cascade amplitude modulator architecture is less susceptible to fabrication imperfections. These cascaded amplitude modulators were put in conjunction with the receiver OPA phase shifters in a row-column fashion, as shown in Fig. 3.17.

A series of sniffer diodes are included in the cascaded amplitude modulator structure to calibrate and correct fabrication mismatches and chip-to-chip variations. In addition to dummy heaters to improve heat gradient in the receiver array, independent heaters were included to further improve the control of the temperature gradient on the chip using integrated PTAT sensors. The phase-shifter design was enhanced

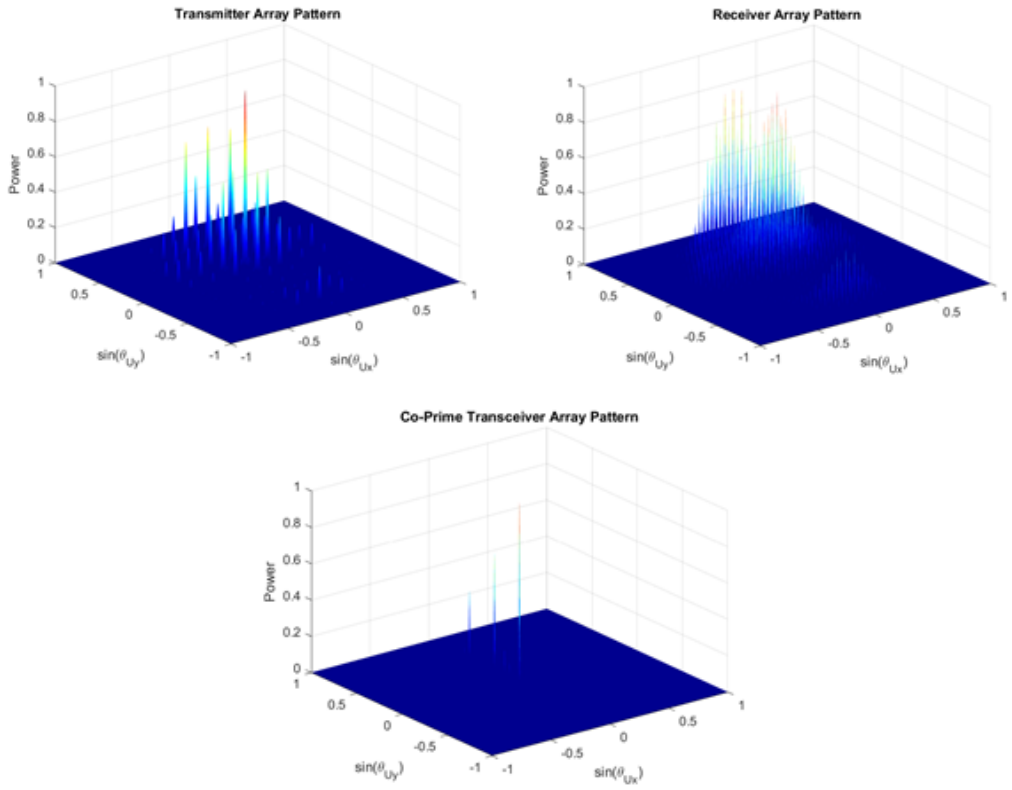

Figure 3.16: 2D radiation pattern of the transmitter, receiver, and effective transceiver array.

with a distributed diode structure to improve heat distribution in each phase shifter. The block diagram of the second chip is shown in Fig. 3.14.

3.4 Measurement Result

A photonic far-field pattern measurement setup using fiber for illuminating the receiver and a photodetector for collecting the transmitter pattern is constructed. This setup allows for independent transmitter and receiver optimization with high sensitivity. Transmitter beam pattern is measured by scanning the far-field radiated power from the chip (modulated at MHz frequency) at θ_x and θ_y directions. Far-field radiated power was collected by an InGaAs photodetector, amplified, filtered (10Hz bandwidth filter), and digitized. The transmitter beam pattern was optimized for several points demonstrating 2D beamsteering capability in both directions. Fig. 3.18 (a-d) demonstrates four beam patterns with clear grating lobes visible at around 9.5° spacing at both directions as expected. Perspective view of the beam pattern for the direction $(\theta_x, \theta_y) = (0, 1)$ is shown in Fig. 3.18 (e).

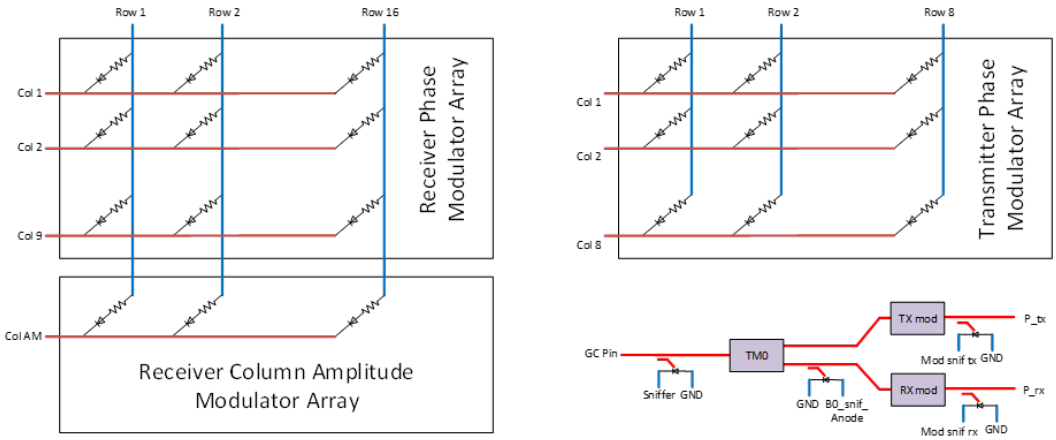

Figure 3.17: Electrical programming nodes of the row-column phase shifters and sniffer detectors for the cascaded amplitude modulator block. Control nodes for the amplitude modulators are wired as an additional column in the receiver phase shifter matrix. Integrated diodes in the phase shifter matrix prevent the reverse flow of current in the adjacent columns. Sniffer diodes before and after the tunable amplitude modulators can be used to calibrate the tunable amplitude modulator network.

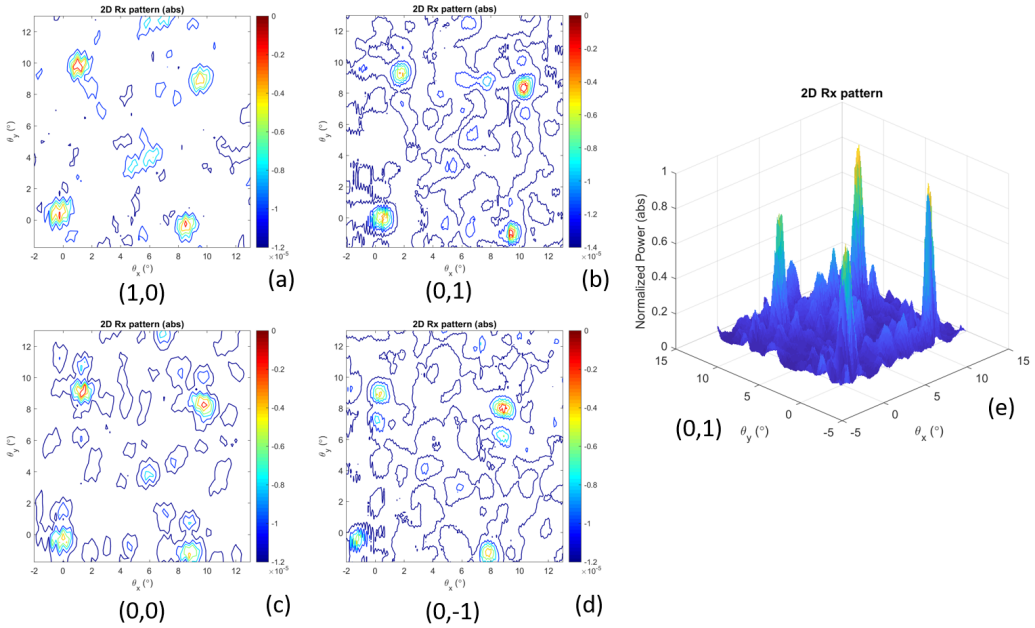

Figure 3.18: Co-prime transmitter beamforming and steering. Grating lobes are spaced 9.55° consistent with 9.2μm spacing of radiating elements. (a-d) Heat map for beamforming optimized for four directions. (e) Perspective view of the Normalized Optical Power for (b).

Subsequently, the receiver array is characterized by illuminating the receiver aperture using a fiber modulated at 10MHz while the reference LO for the receiver is modulated with 11.5MHz. The power collected by the aperture and LO power was mixed in an on-chip balanced mixer and the resulting signal was amplified, filtered (10Hz), and digitized. To remove the random phase fluctuations between the LO path and the illumination fiber path, The RF frequencies were modulated as carrier frequency offsets using external SSB modulators. This setup is used to optimize the receiver beam in several directions. Four such patterns are shown in Fig. 3.19 (a)-(d). The grating lobes were visible at 7.2° in both directions, consistent with the design of the OPA. Perspective view of the beam pattern for the direction $(\theta_x, \theta_y) = (0, 1)$ is shown in Fig. 3.19 (e).

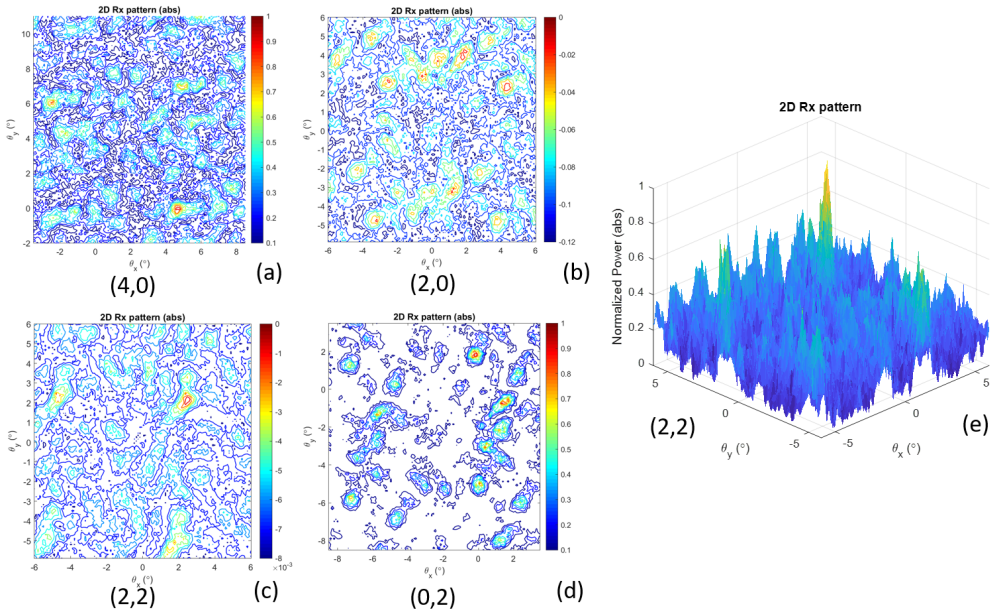

Figure 3.19: Co-prime receiver beamforming and steering. Grating lobes are spaced 7.2° consistent with 12.4μm spacing of radiating elements. (a-d) Heat map for beamforming optimized for four directions. (e) Perspective view of the Normalized Optical Power for (c).

Finally, the full system was characterized by concurrent transceiver beamforming. Fig. 3.20 (blue curves) shows a 1D scan of the formed transmitter and receiver beam over 16° FOV with the expected grating lobes. Programming the two phased arrays simultaneously showed that the thermal cross-talk between the two patterns causes less than 0.5 dB in main beam power of the transmitter and receiver with a

worst case of 5 dB increased side-lobe level for the transmitter array. The combined synthesized pattern for the transceiver array is calculated from the beam patterns and shown in Fig. 3.21. For the full scan range of 16°, the highest side-lobe level is at −12.2 dB with a transceiver beamwidth of 0.6°.

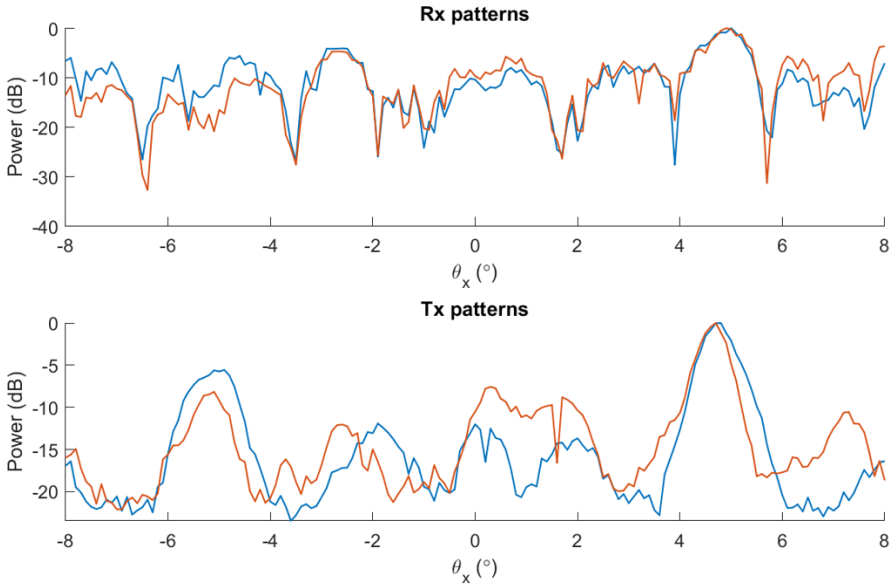

Figure 3.20: Overlap plot of the transmitter and receiver patterns. Beam patterns captured when the optimized settings are loaded separately are shown in blue. Beam patterns captured when both setting are loaded concurrently are shown in red.

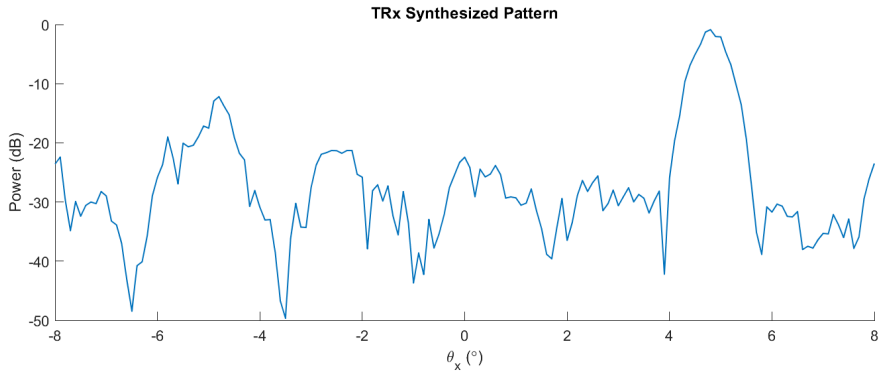

Figure 3.21: Synthesized transceiver pattern.

For Design B, the transmitter's far-field pattern was measured similarly using a rectangular grid scan of the modulated transmitter pattern (Fig. 3.22). The AC performance of the TO phase shifter is measured and shows around 1kHz bandwidth

for the chip (Fig. 3.23). The die photo of the first chip is shown in Fig. 3.24, and the die photo of the second design is shown in Fig. 3.25.

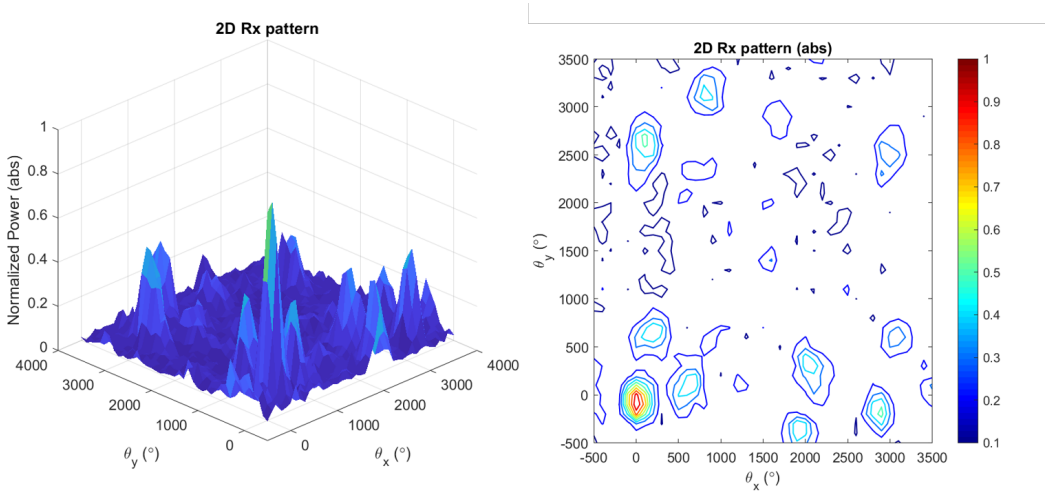

Figure 3.22: Co-Prime Design B tansmitter beamforming.

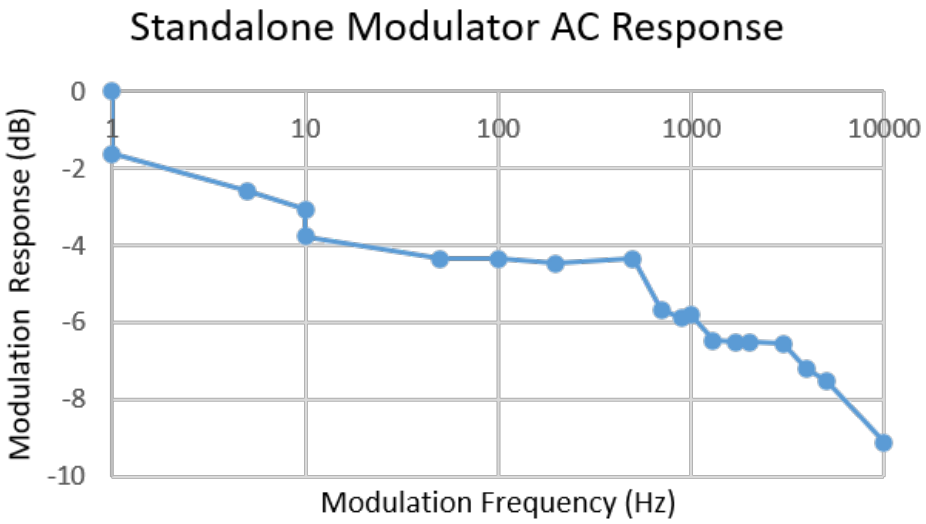

Figure 3.23: Measured bandwidth of the thermo-optic phase shifter.

3.5 Discussion

An important design note in the implementation of the integrated photonics co-prime array is the spacing of the transmitter and receiver arrays, which should be minimized. Projection of the grating lobes for the transmitter and the receiver aperture on the targets get larger as they get closer to the end-fire projection region. This could result in an undesired overlap between the transmitter and receiver

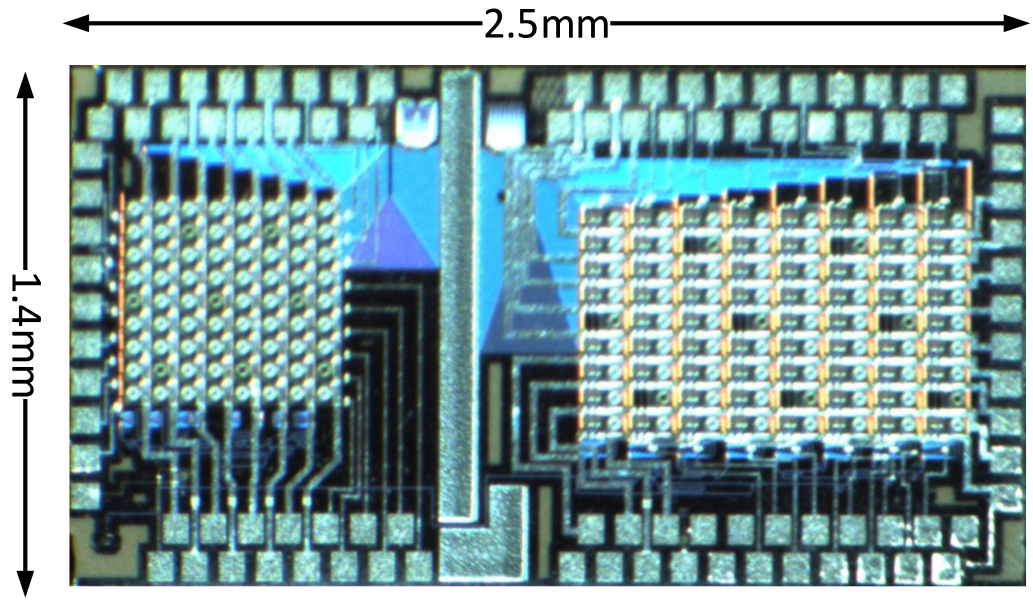

Figure 3.24: Design A die photo.

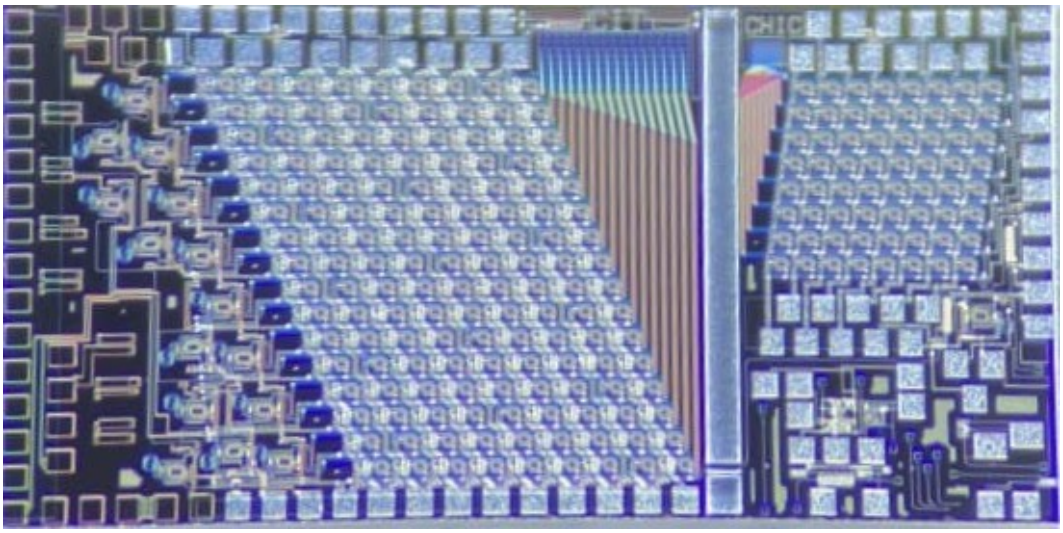

Figure 3.25: Design B die photo.

grating lobes. This is typically not a concern for targets sufficiently far from the transceiver array. However, for targets closer to the apertures, there is a minimum center-to-center pitch requirement between the transmitter and receiver arrays. In the current implementations, the two apertures are separated with only $100\mu m$ to reduce aperture cross-talk through the substrate without affecting the projected beam patterns. In addition, it is worth noting that given the heterodyne detection scheme used in the design and the low noise TIA and LNA chain used for signal

amplification this phased array transceiver, the system is operating to the shot noise limited regime. The noise of the system is given by:

$$SNR = \frac{R}{2e}\frac{P_{tx}\alpha_{OPA,TX}\alpha_{OPA,RX}\alpha_{gratinglobe}\alpha_{freespace}\alpha_{reflection}}{\Delta f} \tag{3.14}$$

Here, $\alpha_{OPA,TX}\alpha_{OPA,RX}\alpha_{gratinglobe}$ are functions of the system design parameters. Desired depth resolution and accuracy of target reflection intensity profile set the required transmitter power and per pixel integration time, $\tau_{pixel} = 1/\Delta f$.

For imaging and ranging applications where the target dimensions are comparable or larger than the projected transmitter grating lobe on the target, as is the case for short and mid-range imaging and automotive radars, the free-space loss is given by the one-way Frii's equation:

$$\alpha_{freespace} = \frac{N_{rx}Area_{pixel}}{2\pi R^2} \tag{3.15}$$

This analysis indicates a trade-off between the size of the aperture, which translates to higher resolution and received power versus transceiver efficiency. For larger arrays, more power is collected by the receiver but the inter-element spacing is increased, resulting in power loss in the transmitter grating lobes reducing the system SNR. Multi-beam receiver architectures can simultaneously collect power from different transmitter grating lobes and break this trade-off.

Chapter 4

LARGE-SCALE BEAMFORMING BASED ON ANNULAR-RING DIFFRACTION PATTERN

An integrated active beamformer inspired by an annular ring diffraction pattern is implemented in an integrated photonic platform. This circularly symmetric structure achieves a very narrow beamwidth with 13 dB side-lobe rejection using 255 radiating elements. Extending the aperture size reduces the beamwidth and peak SLL while maintaining radiation efficiency. As a result, this aperture collects more power for larger apertures, improving the active array's beamforming. Furthermore, the aperture's symmetric nature allows for centrosymmetric routing of the signals to the apertures permitting this architecture to be implemented in a planar silicon photonics platform[1].

4.1 Introduction

Unlike discrete photonic components such as lenses and parabolic mirrors that perform image reconstruction via a continuous frequency sampling of the iris and sample the image using discrete detectors, integrated optical beamformers reconstruct the image via discrete frequency sampling. For typical Cartesian grid OPAs where elements are placed on a rectangular grid, the dielectric waveguide and planar nature of the integration platform limit the FOV of the imagers by the introduction of grating lobes. A solution to this problem in the photonic domain has been explored in antenna array theory with selective removal of elements from the Cartesian grid. In phased-array theory, this is known as thinned arrays. These arrays typically trade sparsity with beam efficiency. The larger the aperture, the smaller the beamwidth and SLL, but the fraction of the main beam's power reduces. 1D-OPAs and 2D-OPAs incorporating thinned array have been demonstrated in the past [17], [65] and show great promise. These architectures synthesize an array by random placement of elements on a 2D grid in an iteration through various optimization methods such as genetic algorithms, etc., to achieve the desired beamwidth and SLL.

This work is a form of a thinned array that utilizes ordered symmetric structures for the systematic design of single beam and 180° FOV thinned arrays. It is inspired by the diffraction pattern of the annular aperture, which can be simply derived from

[1]This work was done in collaboration with Reza Fatemi and Artsroun Darbinian.

the diffraction pattern of a circular aperture. In the case of a circular aperture (Fig. 4.1 (a)) the far-field diffraction pattern (far-field beam pattern/array factor (AF) in phased-array terminology), when illuminated by a plane wave, is given by a Bessel function as shown in (4.1), and the beamwidth is determined by diameter of the aperture (D) [72]. Annular ring aperture (Fig. 4.1 (b)) can be directly calculated from that result and shows that the array factor for the annular ring is a Bessel function of order zero (4.2). This means that blocking the center of the aperture improves the beamwidth slightly, resulting in a narrower beamwidth for the same aperture size. The array plots for the ring and annular ring apertures for an aperture radius to wavelength ratio R/λ of two is shown in Fig. 4.1 (c). These demonstrates that a much smaller area of the aperture can achieve similar beamwidth as a circular aperture at the cost of reduced beam efficiency. Combining several annular ring apertures with different radii improves the beam efficiency and converges to the far-field pattern of the circular aperture at the limit. These two features (single radiating beam for an annular ring aperture and improved SLL for a combination of several annular ring apertures) are appealing from an integrated planar OPA design standpoint where coherent signal distribution is a challenge. We can further simplify the aperture while maintaining the beamwidth profile and keeping the side-lobe levels relatively low through discrete sampling on the annular ring, which is explained in the next section.

$$|AF_{Ring}(\theta)| = |FT[circ(x, y, D)]| = \frac{J_1(kD/2sin(\theta))}{kD/2sin(\theta)} \tag{4.1}$$

$$|AF_{AnnularRing}(\theta)| = |FT[circ(x, y, D) - circ(x, y, D - \delta)]| = J_0(kD/2sin(\theta)) \tag{4.2}$$

In this work, the methodology for the analysis of discretized annular rings is present. Next, a circular array comprised of 255 radiating elements with independent phase and amplitude control is implemented. A network of phase and amplitude modulators adjust the relative phase and amplitude of the element for active beamforming using row-column addressing to reduce electro-optic interconnect complexity. The amplitude control architecture maintains a constant power delivered to the aperture for any amplitude setting. A photonic far-field measurement setup optimizes the phase and amplitudes to achieve beamforming and beam steering. Finally, the performance of these discretized annular ring OPAs are examined for larger aperture OPAs.

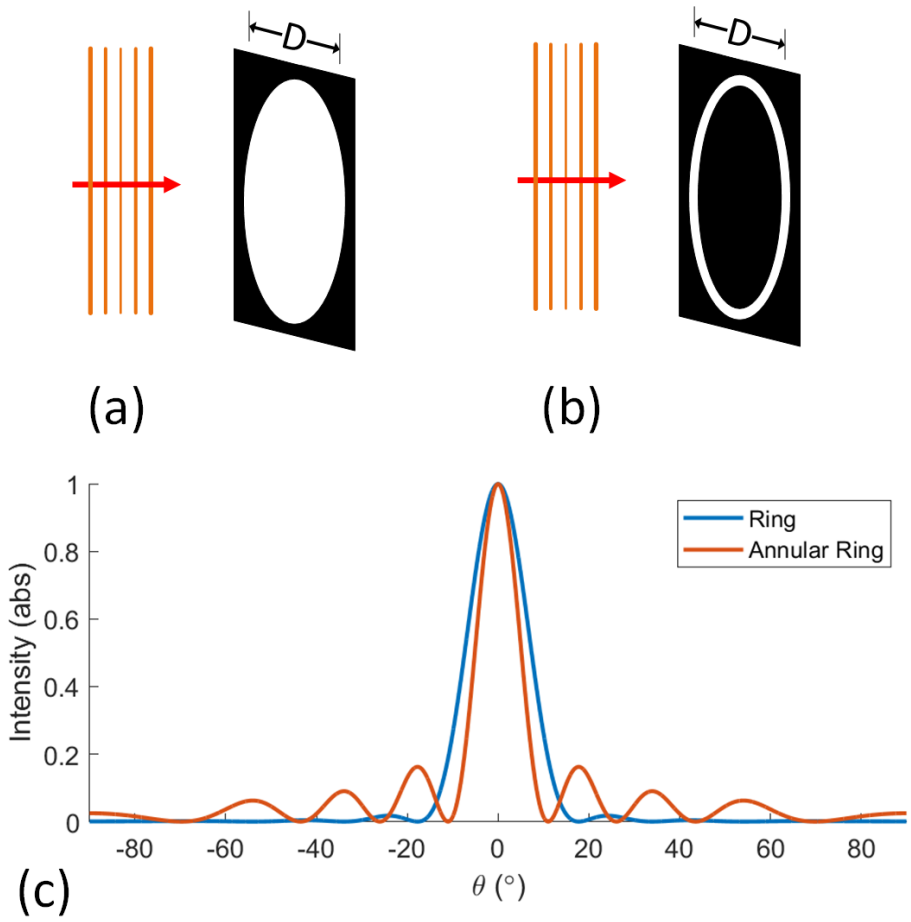

Figure 4.1: Comparison of circular and annular ring diffraction patterns. (a) A circular ring aperture of diameter D illuminated by a plane wave. (b) An annular ring aperture of diameter D and infinitesimal slit width illuminated by a plane wave. (c) Cross-section of the diffraction patterns of the ring and the annular ring apertures for aperture radius to wavelength ratio of two. The beamwidth of the annular ring is slightly narrower than a circular aperture, but the slide-lobe levels (SLL) are higher.

4.2 Theory

In this section, the far-field pattern for a discretized circular aperture OPA is derived, and the discretization grid where the beam pattern approaches the continuous aperture in the form of a Bessel function of order zero is analyzed. In effect, the beam pattern of a circular aperture for elements placed on a polar grid is derived. Polar grid arrays have been previously explored in RF domain [47], [73], [74]. It is assumed that elements are placed on M concentric circles. The pair (r_m, N_m) gives the ring radius and the number of the elements on the mth ring, as shown in Fig. 4.2. Assuming isotropic radiators $E(r) = \frac{C}{r}e^{-jkr}$ where C is the modulation coefficient,

k is the wave-number, and r is the distance to the observation point, we can write the coherent contribution of all radiating elements, as shown in (4.3), in which $R_{m,n}$ is the distance between m, nth element and the observation point.

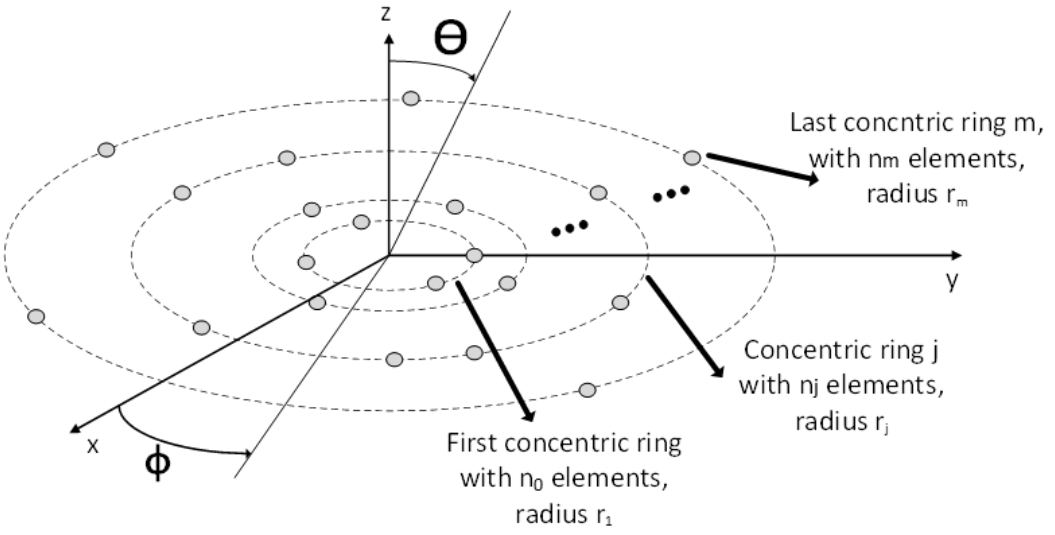

Figure 4.2: Circular array aperture with element placement on the polar grid.

$$|E_{PolarGridAperture}(r,\theta,\phi)| = \sum_{m=1}^{M}\sum_{n=1}^{N(m)} \frac{C_{m,n}}{R_{m,n}} e^{-jkR_{m,n}} \tag{4.3}$$

Assuming an observation point in the far-field, we can approximate $R_{m,n} \approx r$ where r is the center of the array resulting in the simplified expression given by (4.4).

$$|E_{PolarGridAperture}(r,\theta,\phi)| = \frac{1}{r}\sum_{m=1}^{M}\sum_{n=1}^{N(m)} C_{m,n}, e^{-jkR_{m,n}} \tag{4.4}$$

Carrying out the far-field approximation for the exponential term $R_{m,n}$, where (ϕ_m, n, r_m) present the radius and angle between the m, nth element, and the center of the aperture and the radius of the ring on which the m, nth element is placed, we will have $r^2 \gg r_m^2$. We can write

$$R_{m,n} \approx r - r_m sin(\theta) cos(\phi - \phi_{m,n}) \tag{4.5}$$

After plugging in (4.5) in (4.4), we get

$$|E_{PolarGridAperture}(r,\theta,\phi)| = \frac{e^{-jkr}}{r}\sum_{m=1}^{M}\sum_{n=1}^{N(m)} C_{m,n} e^{jkr_m sin(\theta) cos(\phi-\phi_{m,n})} \tag{4.6}$$

We can further simplify (4.6) by writing the modulation coefficient in polar form ($C_{m,n} = c_{m,n}e^{(}\beta_{m,n})$) and assume uniform amplitude excitation ($c_{m,n} = 1$). The $\beta_{m,n}$ term can be used for beamsteering and can be re-written as $\beta_{m,n}(\theta_0, \phi_0) = -jkr_m sin(\theta_0)cos(\phi_0 - phi_{m,n})$ for steering the beam in (θ_0, ϕ_0) direction. This will result in the general uniform excitation expression in (4.7) for the array factor of elements placed in a polar grid array (PGA) steered in the direction (θ_0, ϕ_0)

$$|AF_{PGA}(\theta, \phi, \theta_0, \phi_0)| = \sum_{m=1}^{M} \sum_{n=1}^{N(m)} e^{jkr_m(sin(\theta)cos(\phi-\phi_{m,n})-sin(\theta_0)cos(\phi_0-\phi_{m,n})} \tag{4.7}$$

To compare this result with the continuous annular ring aperture, we assume a single ring $M = 1$ in the broadside $(\theta_0, \phi_0) = (0, 0)$ as shown in (4.8).

$$|AF(\theta, \phi)| = \sum_{n=1}^{N(m)} e^{jkr_m(sin(\theta)cos(\phi-\phi_{m,n})} \tag{4.8}$$

Next, in the scenario where the elements on the ring approach infinity, the summation can be replaced by an integral for all $\phi_{m,n}$ between 0 and 2π and calculate the result for $\phi = 0$ since the pattern will be circularly symmetric, which is the zeroth-order Bessel function of the first kind consistent with (4.2).

$$|AF(\theta)| = \int_0^{2\pi} e^{jkr_m sin(\theta)cos(\phi_{m,n})} d\phi_{m,n} = 2\pi J_0(kr_m sin(\theta)) \tag{4.9}$$

Finally, based on the generalized array function (4.7), we can start considering the effects of integrated photonic routing constraints on this analysis and place radiating elements on each radius r_m further and further apart to provide enough room for the dielectric radiators as well as signal distribution network. We observe that for a large number of uniformly distributed elements on the ring, the Bessel discretization approximation holds for the entire FOV. For example, for a wavelength of $1.55\mu m$, 50 radiators on a $10\mu m$ radius ring ($1.25\mu m$ radially spaced elements), the discretization exactly matches with the continuous form as seen by the blue curve in Fig. 4.3. As the number of elements on the ring is reduced to 40 and then 20 radiators, the Bessel approximation holds for a narrower FOV of 58° and 23°, respectively, and SLL increases. Based on the element spacing, $1.6\mu m$ large dielectric radiators and $3.1\mu m$ large dielectric radiators can be placed on the two 40- and 20-element annular ring apertures for practical implementation. While these structures have an increased SLL, in practice, a fraction of those SLL will be suppressed with the limited FOV of the radiating elements.

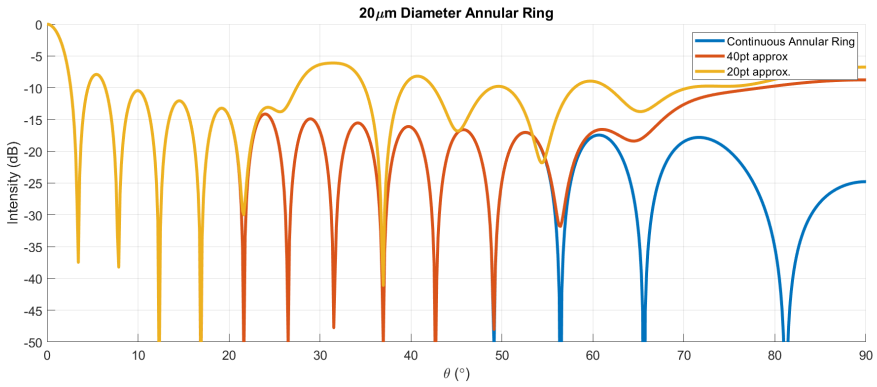

Figure 4.3: Effect of annular ring discretization on the far-field array factor. $20\mu m$ diameter ring is plotted for a continuous annular ring slit aperture, discretized with 40 omni-directional radiators ($1.6\mu m$ radially spaced elements and Bessel approximation valid up to 58°), and discretized with 20 omni-directional radiators ($3.1\mu m$ radially spaced elements and Bessel approximation valid up to 23°). As the number of elements is reduced, the SLL increase and the Bessel approximation holds for a narrower FOV.

4.3 Design

The discretized multi-annular ring OPA system has a $400\mu m$-diameter aperture with 255 radiating elements controlled by four groups of phase and amplitude controllers with the row-column drive. Annular-ring OPA array factor was optimized based on routing constraints of $1\mu m$ minimum pitch and $2\mu m \times 5\mu m$ compact photonics radiators. In addition, the linear density of the aperture is kept constant to maintain uniform power distribution and circular symmetry in the aperture. The 255 radiating elements of the aperture are placed on five concentric circles with the innermost circle $n_1 = 17$ radiators placed equidistant on a $r_1 = 40\mu m$ radius. The ring's radius increases with $40\mu m$ linear increments, and the number of radiators per ring increases linearly by increments of 17. This results in placing $(17, 34, 51, 68, 85)$ radiators on $(40\mu m, 80\mu m, 120\mu m, 160\mu m, 200\mu m)$ radius rings, respectively. The annular ring aperture maintains the Bessel form for 2° FOV. This aperture has a theoretical beamwidth of 0.2° with no grating lobes and a full 180° FOV. The largest side-lobe level is at -10.5 dB for omni-directional radiators. The radiating element is the same structure as the radiator in co-prime array (Fig. 3.10) with 22° FOV and over 50% peak radiation efficiency at the optimum angle of 9°. When considering the radiating elements' far-field pattern, the FOV of the aperture is limited to the FOV of the radiating element (22°). This analysis suggests that the total theoretical resolvable spots for this aperture is 12,100. The largest side-lobe level with the FOV

of the aperture is below −15.6 dB.

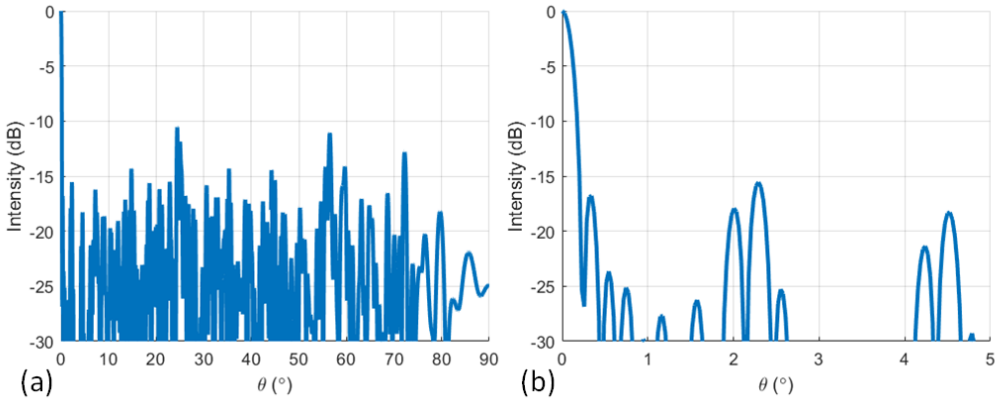

Figure 4.4: 255-element annular ring OPA AF assuming isotroptic radiators. (a) Full AF of the aperture for $\phi = 0$. (b) Close-up AF of the aperture for $\phi = 0$. This aperture has a theoretical beamwidth of 0.2° with no grating lobes with the highest SLL at −10.5 dB.

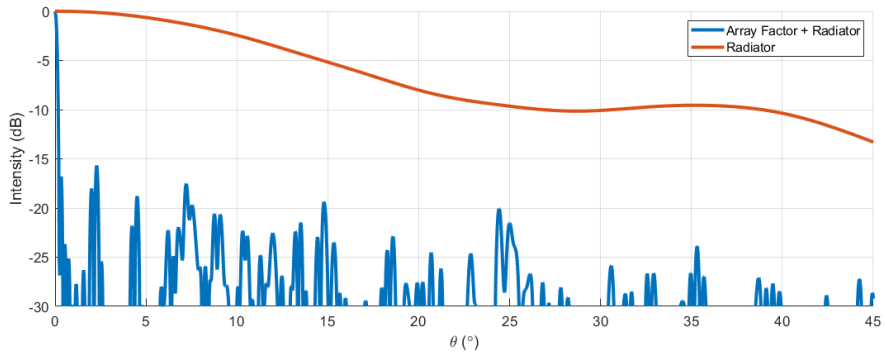

Figure 4.5: 255-element circular OPA AF including the radiator far-field pattern. The grating coupler-based radiator limits the FOV of the aperture to 22° with the highest side-lobe level of −15.6 dB resulting in a total of 12,100 resolvable spots using this aperture.

The phase and amplitude modulators for 255-elements are grouped into four blocks. Within each, there are 16×4 amplitude modulators and 16×5 phase modulators (Fig. 4.6). The amplitude modulators are placed in a distributed tree structure as a series of tunable couplers that maintain a constant power output through the aperture for all amplitude modulator array configurations compared to the scenario where each signal path contains an amplitude modulator. In the latter case, if it is desired to modify the amplitude of a signal path from a maximum to a lower value, the difference in the power value will be radiated out of the chip. In contrast,

in the tunable coupler distribution tree, the power is diverted from one signal path to the other. For each block, the columns of the phase and amplitude modulators are shared resulting in a 16×9 row-column block that needs to be driven with external circuitry with a pulsed-amplitude modulation (PAM) drive circuit. This reduces the drive circuit complexity from $O(N^2)$ to $O(N)$. An array of $N \times M$ phase and amplitude modulators placed in a rectangular grid requires only $N + M$ driver voltages. This is critical for large OPA designs. In the case of this design, 25 drivers can independently address 144 phase and amplitude modulators. 100 drivers are required to control 510 phase and amplitude modulators. A PIN modulator is placed in the input path that helps distinguish between the light coupled into the waveguide and the uncoupled stray light from the fiber that reflects off of the substrate and interferes with the measured far-field signal. A 1% sniffer photodiode, after the input fiber grating coupler, helps in monitoring the total power coupled into the chip, while another 1% sniffer photodiode is used to monitor the extinction ratio of the PIN modulator. Several proportional to absolute temperature (PTAT) sensors are placed throughout the chip that can be used to monitor temperature gradients across the chip. Furthermore, the path mismatch between different signal paths, especially the path mismatch between four modulator blocks, is compensated with on-chip spirally delayed lines.

A series of duty-cycled pulsed-amplitude-modulators periodically cycle through 16 pre-set values stored in a series of DACs for the row-column drive. During each time-slot (1/16 of the cycle), one column is forward biased to the desired value while the remaining columns are in reverse bias. Each column is active only 1/16 of the cycle, and hence the power delivery to that particular column is 16 times the target value. Since thermal modulators operate at low kHz range frequencies, a PAM signal in the order of a few MHz is sufficient to maintain desired values in all phase and amplitude modulators. A diode in series with the heater element prevents the reverse flow of current in the undesired branches. This allows for independent programming of all 510 phase and amplitude modulators. The spiral phase modulator with oxide-etched isolators in this design (used as phase and amplitude modulator) is similar to the phase modulator in co-prime OPA (Fig. 3.7). A series of dummy heaters is placed in the phase modulator blocks that help to maintain a constant thermal profile on the chip.

As mentioned earlier, a novel feature of this row-column amplitude distribution block is the incorporation of a tree-distributed tunable amplitude modulator with

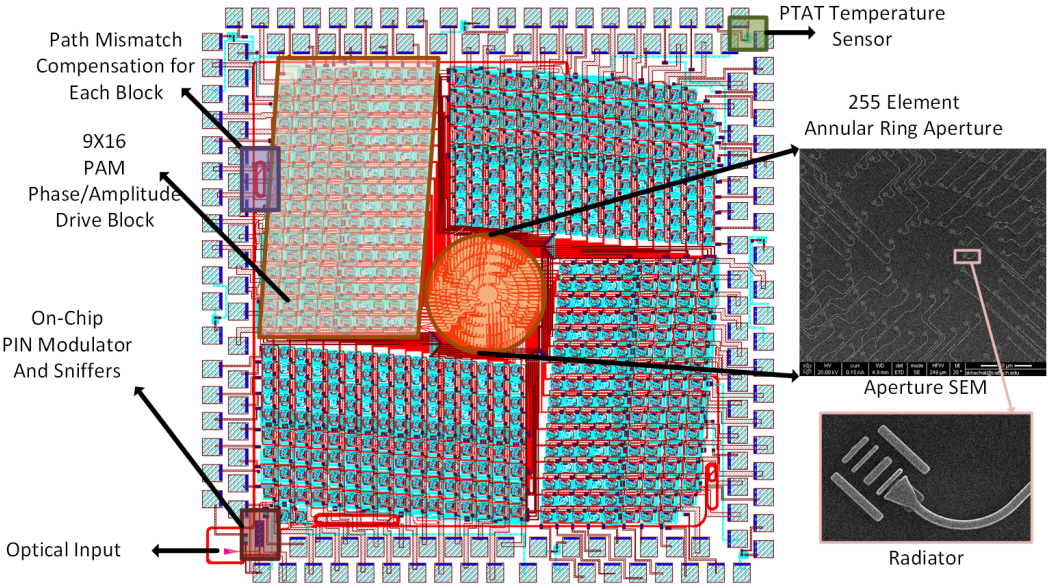

Figure 4.6: Circular OPA layout. 255-element aperture is controlled by four blocks of 9×16 phase/amplitude modulators. Integrated PIN modulator, as well as sniffers, help monitor the power coupled into the chip. Low-loss on-chip delay light compensates for the path mismatch between different blocks of the aperture. Distributed PTAT sensors can be used to track the on-chip thermal gradient. An SEM image of the 255-element aperture, as well as the unit radiator, is shown on the right.

calibration photodiodes (Fig. 4.7). This architecture can be used to compensate for path mismatch between different paths due to initial fabrication imperfection. A one-time calibration can be done for each chip and use N sense nodes to adjust a $1:2^N$ tunable power splitters with 2^{N-1} sniffer photodiodes. A $1:8$ power splitter is depicted in Fig. 4.8 to explain the calibration flow. PD0 can be used to determine the total input power to the structure. AM0 output can be swept between minimum and maximum using the row-column drive circuit, and the power division ratio can be tracked with PD1. This power distribution curve can be stored and be used for calibration and tuning of AM0 during OPA beamforming operations. Afterward, the total power will be switched to path one, which results in PD2 reading only the power in the top branch. Afterwards, AM11 can be calibrated similarly to AM0 using PD1 and PD2 power levels. In the next step, the full power will be diverted to the lower branch for calibration of AM12. This process is repeated until all amplitude modulators are calibrated. In addition, compared to the conventional design of one amplitude modulator per branch, this tree-distributed approach can get a better extinction ratio when switching the power entirely off in particular branches. If the available tunable splitter can get a maximum ratio of one to nine, the cascaded

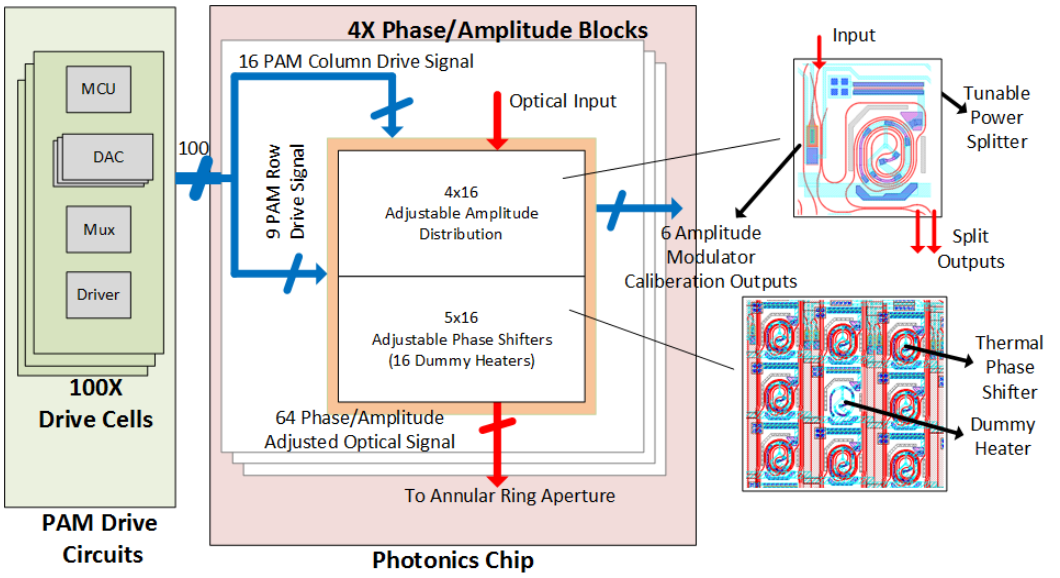

Figure 4.7: Block diagram for independent drive and control of the on-chip phase and amplitude modulators. A tunable MZI power splitter can be used to divert signal from one signal path to the other. 16 DACs, in conjunction with a multiplexer and a high voltage amplifier, construct each of the 100 PAM signals on the chip. Dummy heaters are distributed in between the phase shifter to help with stabilizing the on-chip thermal gradient.

tunable splitters can better isolate the desired signal path.

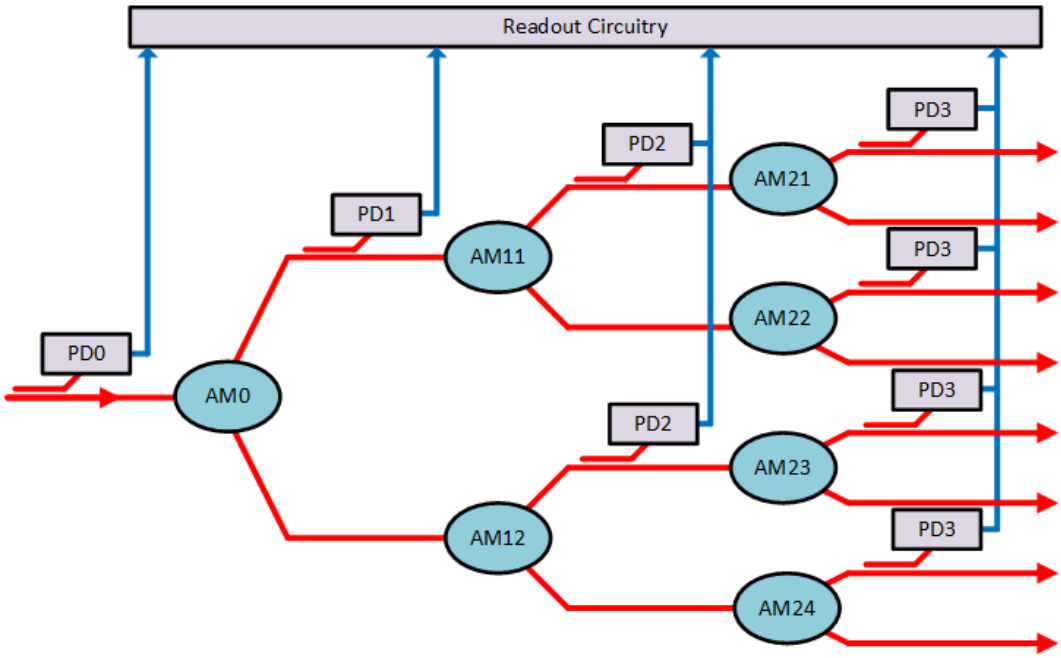

Figure 4.8: Circular OPA amplitude control block diagram.

4.4 Measurement Result

The row-column drivers apply a variable amplitude pulse of 15v with 10-bit resolution with 10ns rise and fall time. The pulse width can be set to as small as 40ns. Henceforth, the driver can switch between 16 different values at a 1.56MHz repetition rate for different column settings. Since the thermal modulators have a 30ms thermal time constant, reprogramming them at a 1.5MHz rate is sufficient for the thermal modulators to maintain the desired value. To calibrate for the phase and amplitude variation from fabrication mismatch and to form a beam in the desired direction, a combined optimization scheme was used. Due to the high number of phase and amplitude modulators, first, a randomized search algorithm searches the entire solution space for potential optimum beams, as shown in Fig. 4.9 (green), where the optimum point is 4 dB higher than the scenario when all DACs were off. After two-hundred iterations, the optimizer finds several potential optimum points. After verifying the best outcome, a modified gradient descent algorithm is employed where several DACs are randomly modified in a random direction. If the optimum point is obtained, the optimizer progresses in that direction till a maximum is found. Afterward, this process is repeated. Typically after another 250 iterations, the optimum point is improved slowly by another 1-2 dB as seen in Fig. 4.9 (purple region).

The dynamic beamforming stability and repeatability of this circular OPA are captured by recording the normalized beam power in the broadside direction when the OPA phase-shifter setting is toggled between the case when all drivers are off, and all drivers are set at the optimum value. As shown in Fig. 4.10, the optimized setting increases the radiated power in the broadside direction by around 6 dB in optical beam power. It takes around 2 seconds to program the phase shifters. The thermal gradient on the chip and all the amplitude and phase shifters settle thermally in approximately 8 seconds when switching from driver off state to optimum beam setting. The ripple in the optimized setting is less than 0.4 dB between several cycles of tuning of the PAM drivers and setting them to the optimum setting, which shows high reliability of the measurement.

An on-chip modulator separates between the power coupled into the chip and the uncoupled optical power reflected from the surface of the chip or the silicon substrate, and a narrow-band filter on a spectrum analyzer isolates the signal with high SNR similar to a lock-in amplifier system. A custom two-axis stage, moving an InGaAs photodiode in (θ_x, θ_y) directions at a 5cm constant distance from the chip is used

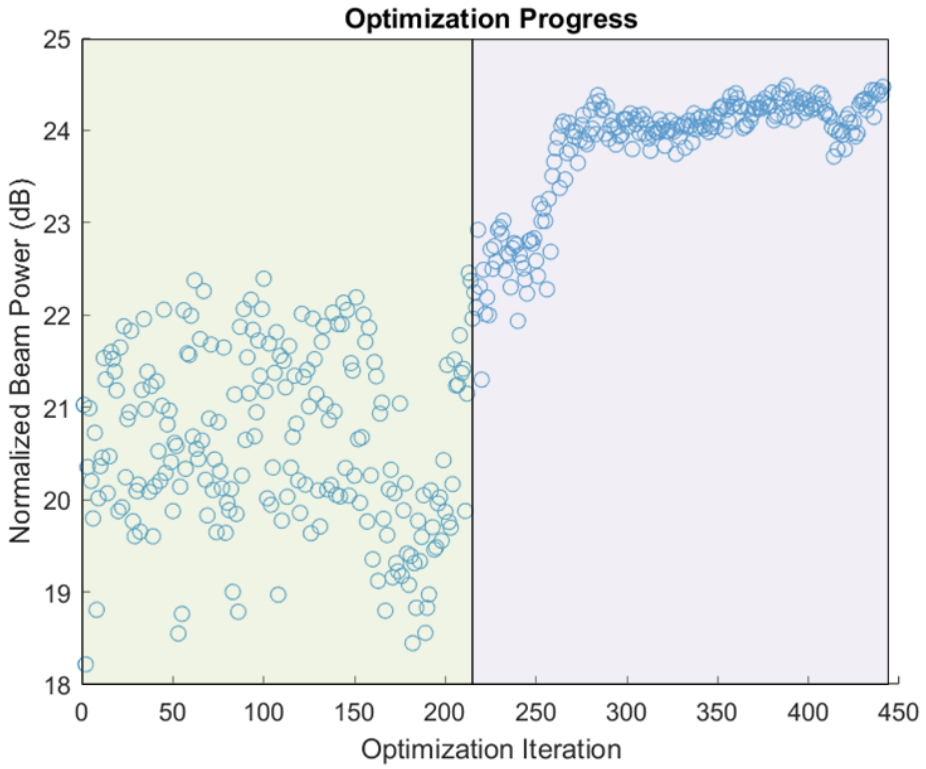

Figure 4.9: Optimization progression after 450 iterations. The first 200 iterations are random searches in the solution space looking for the potential optimum points. Afterward, the most optimum point is verified, and modified gradient descent algorithms find the optimum solution.

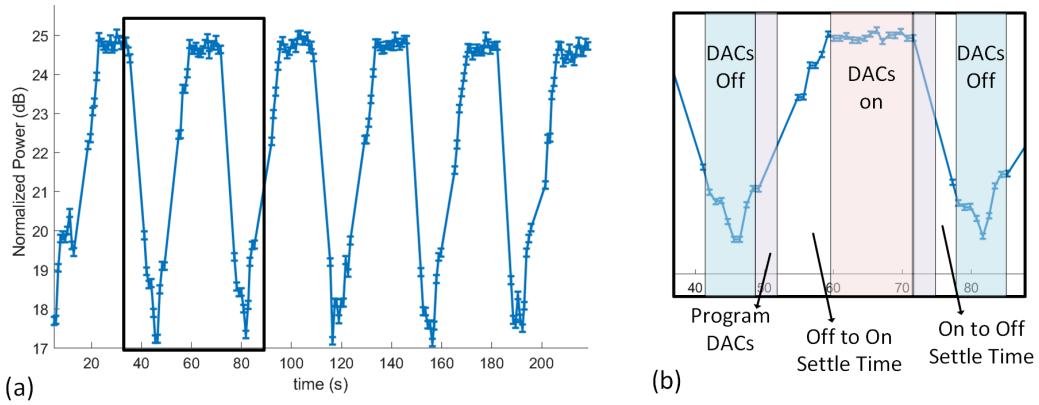

Figure 4.10: Dynamic stability of circular OPA from one setting to another: Here, the system setting is toggled between the initial unoptimized setting (All DACs off) and optimized beam pattern for the direction $(0, 0)$. It takes $10 - 12$ seconds for the thermal gradient to stabilize between different settings. The optimizer is able to increase main beam power by a minimum of 6 dB from the initial setting.

to measure the far-field beam-pattern of the optical phased array. A 2D scan of the beam pattern (Fig. 4.11 (a)) using this far-field measurement system shows no visible grating lobes in $(10°, 10°)$ FOV. The highest measured SLL is 4 dB in optical beam power below the main beam showing beamforming with no grating lobes. Each point is measured three times, and the resulting average is plotted. The cross-sectional scans show the power fluctuations is less than 1 dB at peaks and a maximum of 2 dB at minimum points as it is seen in Fig. 4.11 (b) and (c). The annular ring OPA is re-optimized in three other directions, $(\theta_x, \theta_y) = (-1.2, 0)$ and $(\theta_x, \theta_y) = (-3.4, 0)$ in θ_x direction (Fig. 4.12 (a)) and $(\theta_x, \theta_y) = (0, 2.2)$, to demonstrate beamsteering in θ_y directions (Fig. 4.12 (b)). The best measured beamwidth for the demonstrated annular ring OPA is around 1°, and the entire chip area is $2.2mm \times 2.2mm$.

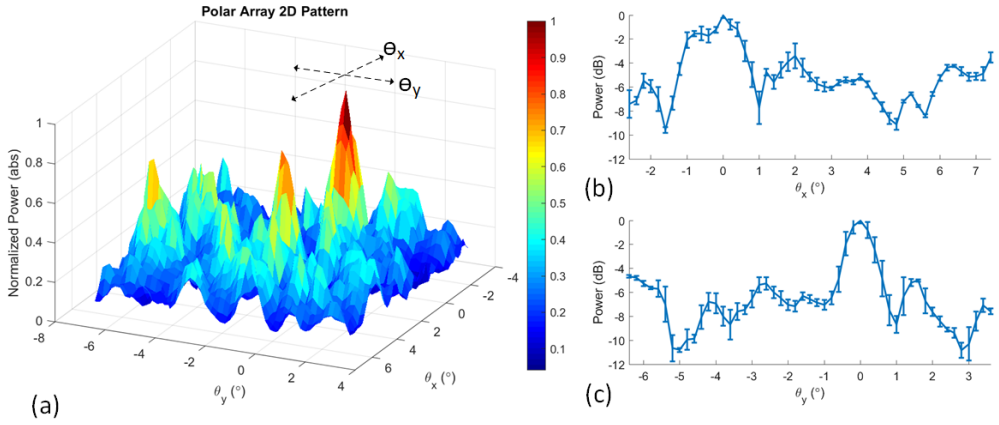

Figure 4.11: 2D beamforming demonstration: (a) Two-dimensional beam pattern was measured for the optimized direction $(0, 0)$. (b) and (c) are 1D cross-sections of the beam pattern in θ_x and θ_y directions. The measurement standard deviation shows high repeatability of the measurement results.

4.5 Discussion

The beamforming capability of this OPA was demonstrated over a 10° FOV with 1° beamwidth. Given the radiation pattern of the individual radiator, this will result in 22×22 = 484 resolvable spots for this aperture. It is worth discussing possible factors that contributed to the discrepancy between the expected beamwidth of 0.2° and SLL of 15 dB compared to the measured result. First, the large solution space for the optimum setting of 510 phase and amplitude modulators with 10-bit resolution each makes it difficult to find the optimum solution by calibrating out the possible path mismatches on the chip. The customized design of the spiral MZI helps in thermal

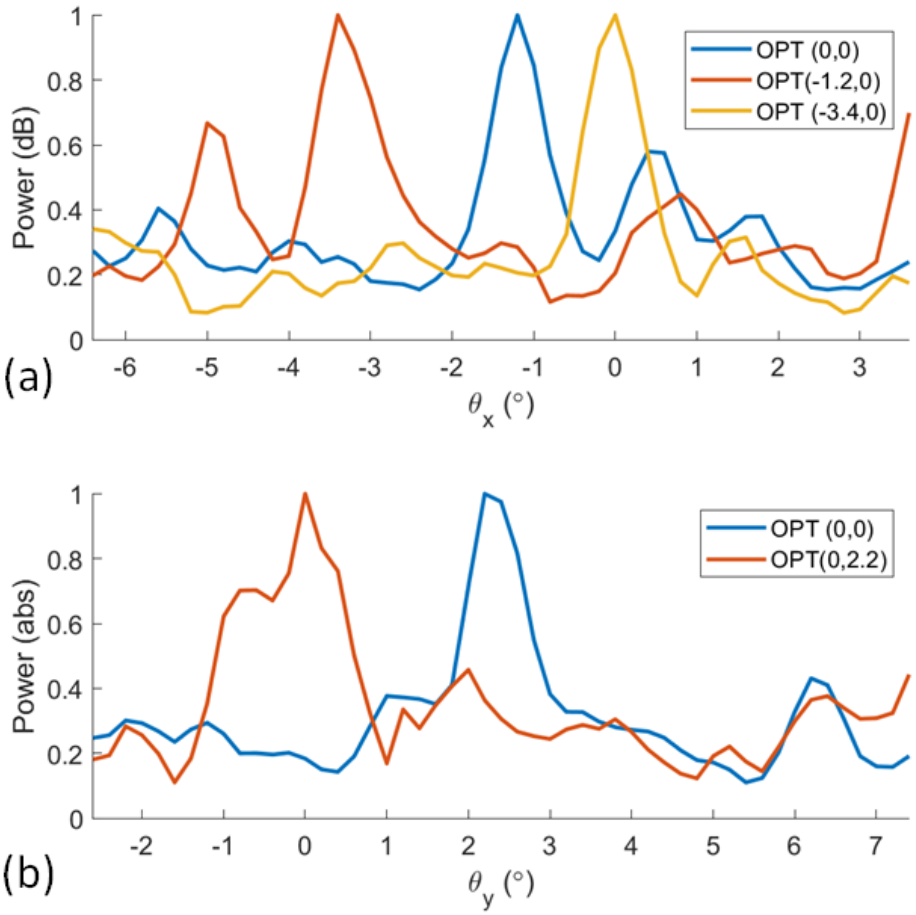

Figure 4.12: 1D beam pattern for several directions. (a) Integrated beamforming in θ_x was demonstrated by optimizing the beam in two additional directions, $(\theta_x, \theta_y) = (-1.2, 0)$ and $(\theta_x, \theta_y) = (-3.4, 0)$ in θ_x. (b) Beamforming in θ_y was demonstrated by re-optimizing the beam in $(\theta_x, \theta_y) = (0, 2.2)$ direction.

isolation of the modulation as well as reduction of the cross-talk, but it is unable to completely eliminate it, and precise control of the phase and amplitude modulators is hindered. Both of these potential problems can be addressed with much more complicated designs. First, incorporating electro-optic modulators, despite their large foot-print compared to the spiral MZI modulator, do not suffer from cross-talk [43]. In addition, integrated interferometers and sniffer photodiodes can be used to precisely measure out the relative phase and amplitude of the signals in different paths and can be used to bypass the large search space of the optimizations required for beamforming [52]. With fabrication mismatches corrected using integrated interferometers and amplitude control sniffers, the direction of the desired beam can be computed and applied to the OPA.

Three observations from the results of this analysis of this annular-ring OPAs are worth noting here. First, this aperture is highly efficient for signal distribution to and from the aperture due to its circularly symmetric nature. Second, the linear density of the array, which is a function of the process node, sets the beam efficiency of the OPA, and it is possible to implement a radiating-element limited FOV optical phased array even in single-layer silicon photonics process. Finally, given a density limitation for a particular process, which is a function of the number of the dielectric layers, simulation of larger aperture shows that by increasing the aperture size, aperture size can increase as needed to its constant linear density in the array, the beam efficiency remains relatively constant, but the relative SLL and the FWHM decreases. In addition, the effective coherent receiver area increases linearly with the size of the aperture, which results in higher signal sensitivity for a directive receiver. A comparative plot for changes in the beamforming characteristics of different aperture diameter OPAs is shown in Fig. 4.13. Die-photo of the chips is shown in Fig. 4.14.

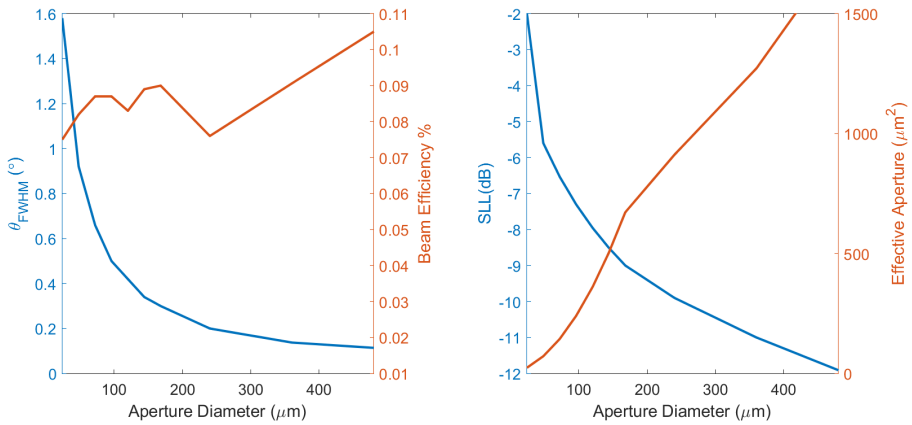

Figure 4.13: Beam efficiency, FWHM, SLL, and aperture area for different diameters of annular-ring OPAs.

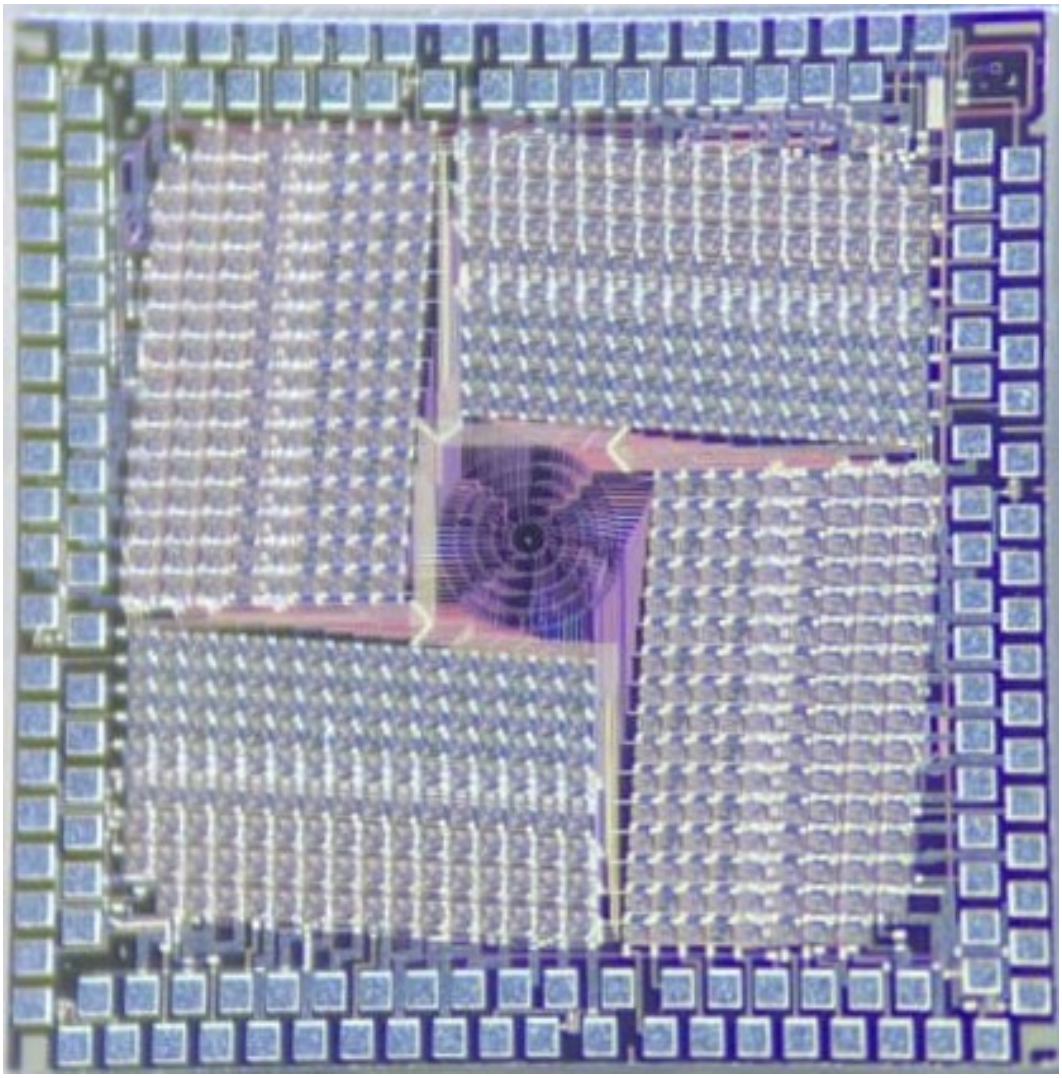

Figure 4.14: Die-photo of the annular-ring OPA chip.

Chapter 5

LARGE-SCALE COHERENT IQ IMAGER

A coherent imaging system using IQ signals capable of rejecting undesired relative phase fluctuations between the illumination and LO path is presented. This aperture incorporates a novel row-column read-out architecture capable of reading N^2 signals from photonic chips using only N adjustable voltage nodes as well as N amplifier chains. A hybrid 90° coupler in conjunction with balanced detectors enables high sensitivity and dynamic range and improves signal acquisition speed[1].

5.1 Introduction

Compared to traditional CCD and CMOS image sensors, coherent homodyne detection offers improved sensitivity due to the perceived gain of the reference path. In surface metrology applications, homodyne photonic image sensors offer high spatial and depth resolution compared to their RF counterparts. Coherent image sensors can also be utilized for remote sensing via loss and refractive index measurements [11]. These characteristics enable coherent imaging systems to have a wide range of applications in 3D imaging, target tracking and detection, robotics, remote sensing, and medical devices [43], [75]. In a typical setup, the imaging target is either illuminated point by point via mechanical or solid-state beam steering [13], [76] or the entire target is illuminated simultaneously using flash or CW illumination. In the latter case, the receiver creates an image of the target via a lens and an array of detectors sample and reconstruct the target [77] (Fig.5.1).

Coherent imagers have two parts: signal detection using a receiver array and signal processing that allows the receiver to perform the desired task (time-of-flight, loss, and refractive index measurements). A lot of work has been done to explore various signal processing schemes as well as analyzing the limitations of these coherent systems. Ranging is done with either direction laser frequency modulation [78] or amplitude modulation of a constant frequency laser [11]. Furthermore, dual and multi-frequency ranging architectures [11], [76], [79], optical frequency comb based ranging [80], [81], comb calibrated FMCW lidar [47], complex waveform modulation for simultaneous range and velocity detection [82]–[86], and pseudo-

[1]This work was done in collaboration with Reza Fatemi and Behrooz Abiri.

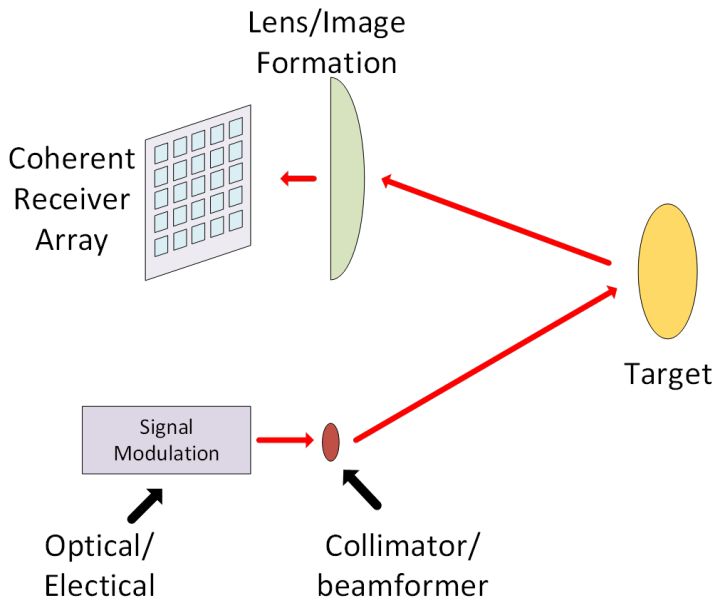

Figure 5.1: In this coherent imaging system, the target is illuminated using a collimated beam, the returned signal is captured via a lens, and the image is formed on the sensor array.

random code modulated lidar [84] are some of the methods for coherent image signal processing.

In this work, an external amplitude modulator is used to apply the chirp signal. Compared to stabilizing a chirped laser signal, analog and digital synthesis methods are much simpler to implement and reduce the system complexity. Here the focus is on improving the performance, similar to [11], which suffers from random phase fluctuation between the illumination and reference paths. Random phase fluctuations acts as an amplitude modulation for the mixed frequency component signal that contains the coherent signal. Every measurement point needs to be sampled continuously until the amplitude of the received signal is maximized (relative phase error between the transmitter and receiver paths becomes zero, and the mixed-signal is maximized). An architecture using in-phase and quadrature signals is proposed that cancels out the LO and signal path's relative phase fluctuation, resulting in a faster and more robust signal acquisition for coherent imaging systems.

5.2 Background

In this section, the lidar signal in [11] is examined, and a solution is proposed to address the shortcomings of said design. The general amplitude-modulated signal

is denoted by $E_s(t)$, and the RF modulation term is denoted by $A(t)$. In the case of FMCW chirp modulation, $A(t) = cos(1/2\zeta t^2 + \omega_0 t)$. Therefore, we have

$$E_s(t) = A(t)cos(\omega_{opt}t + \phi_{opt}), \tag{5.1}$$

where ϕ_{opt} is the random optical phase. In photonic coherent homodyne detection, the reference and signal paths are combined and squared using a photodiode, which is a square-law detector. If the light travel time is denoted by τ, and the illumination to receiver total path loss is denoted by α, the resulting simplified output signal will be

$$I_{mix}(t) = |\alpha E_s(t - \tau) + E_{LO}(t)|^2, \tag{5.2}$$

which simplifies to

$$I_{mix}(t) = \alpha^2 E_s^2(t - \tau) + E_{LO}^2(t) + 2\alpha E_s(t - \tau)E_LO(t)cos(\Delta\phi) \tag{5.3}$$

Here, the time of flight information can be extracted from the third term $E_s(t)E_{LO}(t-\tau)$. Assuming that the first two terms are negligible compared to the mixed term, we can evaluate the system's signal-to-noise ratio (SNR) at the output. We observe the effective signal gain in these coherent imaging systems due to the LO signal and improved detection sensitivity compared to direct detection systems.

$$SNR = \frac{R^2\alpha P_s P_{LO}}{2qRP_{LO} + I_{PDdark} + I_{elec.}} \tag{5.4}$$

$$SNR = \frac{R\alpha P_s}{2qR + (I_{PDdark} + I_{elec.})/P_{LO}} \tag{5.5}$$

Here R denotes the responsivity of the detector. Compared to the direct detection schemes where the system loss is typically limited by the dark current of the photodiode I_{PDdark} or the noise contributions from the electronics I_{elect}, coherent homodyne systems can operate in the shot noise limited region where the SNR is limited by the total power budget ($P_s + P_{LO}$) and round-trip signal path loss α.

In the previous work [11], the coherent imager used direct homodyne mixing of the illumination signal $E_s(t)$ and the reference signal $E_{LO}(t - \tau)$, where single germanium detectors act as square law power detectors for extracting the cross term

with the coherence information. Denoting the amplitude attenuation factor in the signal path with α, the detector's output is shown in Eq. (5.6).

$$I_{PD}(t) = |\alpha E_s(t) + E_{LO}(t-\tau)|^2 \tag{5.6}$$

$$I_{PD}(t) = \alpha^2|E_s(t)|^2 + |E_{LO}(t-\tau)|^2 + 2\alpha E_s(t)E_{LO}(t-\tau)cos(\phi_s - \phi_{LO}) \tag{5.7}$$

The desired signal used for coherent imaging is in the third term, $(E_s(t)E_{LO}(t-\tau))$. In such an imaging system, the first two terms constitute undesired signals and need to be filtered. For imaging scenarios where there is sufficient power in the received signal or there is a significant path difference between the reference and signal path, the strong undesired reference path signal can be attenuated using electrical filters or time-domain multiplexing techniques. The filtered cross-term signal is denoted by I_{PDfilt}. In realistic scenarios where the return signal is weak or the path difference between the signal and reference path is small, it becomes more difficult to filter out the undesired signal degrading the signal quality.

Another challenge with this system is the random phase fluctuations between the signal and the reference path. Due to the thermal variations and mechanical vibrations' differences between the reference and the signal path, there is a random undesired phase mismatch component $\phi_{fluct}(t)$ that randomly modulates the mixed term at kHz frequencies.

$$I_{PDfilt}(t) = 2\alpha E_s(t)E_{LO}(t-\tau)cos(\phi_s - \phi_{LO} + \phi_{fluct}(t)) \tag{5.8}$$

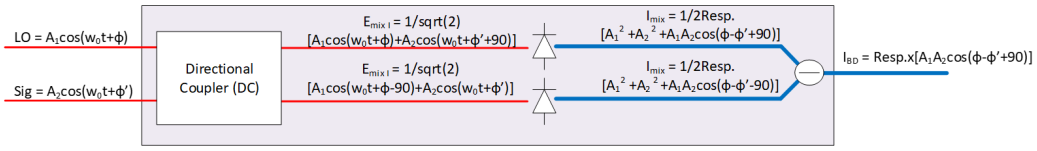

Figure 5.2: Balanced homodyne detection rejects the un-mixed chirp signal.

Since the random phase fluctuations in the signal and LO path are zero mean processes, the effect can be alleviated using averaging and time-domain sampling techniques. The mixed signal is continuously sampled, and only signals above a certain amplitude threshold are used for data extraction. This comes at the cost

of increased signal sampling time to capture high amplitude signals with sufficient SNR that can be used to extract TOF information. In this system, all coherence imaging information needs to be stored in the mixed-signal phase since the amplitude information is unreliable due to the signal capture method. In addition, the strongest signal is the intensity of the reference signal, which can saturate the signal in the electrical amplification chain (Fig. 5.2). Furthermore, in this architecture, the photodiodes are individually interconnected to external electronic circuits for amplification. In the absence of costly monolithic platforms, this system has scaling challenges set by the number of available metal layers and the interconnect pitch used for signal routing. As as result, this architecture increases the cost and complexity of the electronics needed for signal readout.

To address the phase fluctuations challenge as well as the signal saturation caused by the higher undesired signal power, [82] has demonstrated incorporating balanced detectors as well as hybrid 90° couplers in a discrete setup (Fig. 5.3). This topology outputs both the in-phase and quadrature forms of the mixed optical signal, and the contributions from the random phase fluctuations are canceled in the sum-squared of the two outputs. As a result, the desired signal can be sampled much faster since the random path mismatch, and phase fluctuations do not affect the SNR and output signal form, as shown in Fig. 5.4.

$$I_{in-phase}(t) = 2\alpha E_s(t)E_{LO}(t-\tau)cos(\phi_s - \phi_{LO} + \phi_{fluct}) \tag{5.9}$$

$$I_{quadrature}(t) = 2\alpha E_s(t)E_{LO}(t-\tau)sin(\phi_s - \phi_{LO} + \phi_{fluct}) \tag{5.10}$$

$$I_{I^2+Q^2}(t) = 4\alpha^2 E_s^2(t)E_{LO}^2(t-\tau) \tag{5.11}$$

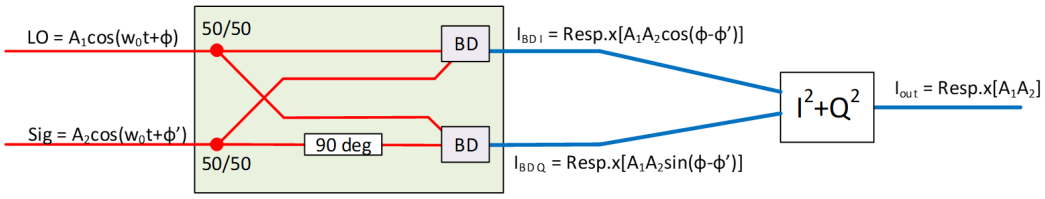

Figure 5.3: Balanced homodyne detection with 90° hybrid can reject random phase fluctuations between the LO and signal paths.

5.3 Design

Here, a hybrid 90° coupler is implemented in a silicon photonics platform for the first time in an 8×8 array with $100\mu m$ element pitch. It is also demonstrated that this

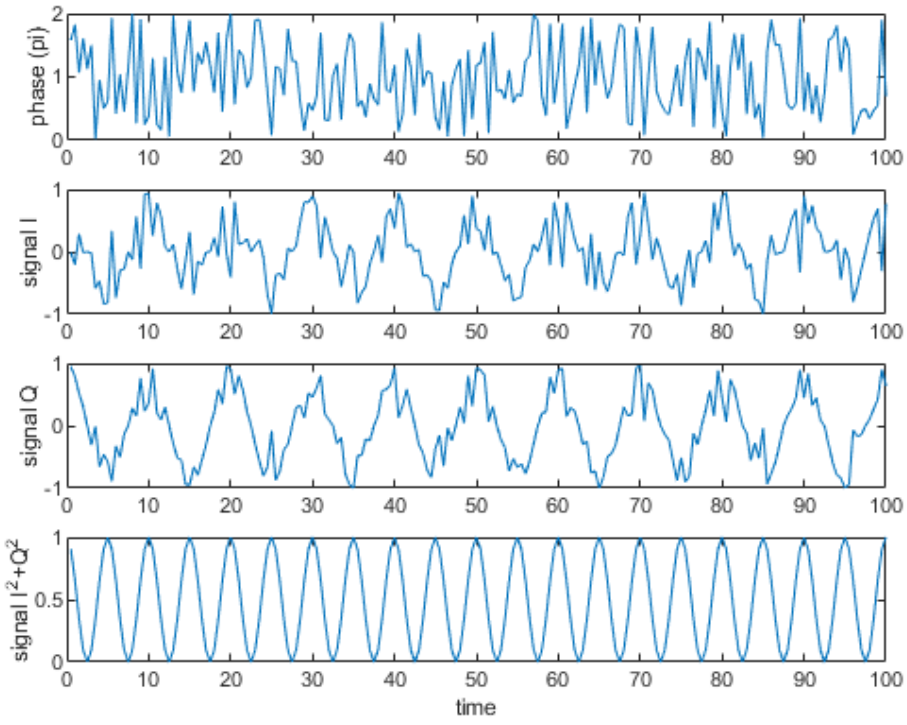

Figure 5.4: Suppression of the path mismatch phase fluctuation using 90° hybrid structure and computing the sum squared term.

architecture can be expanded to any arbitrary aperture size $N \times M$ without running into SNR limitations or optical and electrical routing bottlenecks. Furthermore, this architecture simultaneously captures both the optical phase and amplitude from multiple pixels. Henceforth, it can be used as a complex (real and imaginary) optical imaging system. It can be used with previously demonstrated complex modulation methods, or it can be used to extract the relative optical phase between the adjacent pixels, which has applications in phase microscopy or coherent tomography.

This imaging system has an adjustable reference distribution system feeding an array of 8×8 balanced IQ unit cells with row-column readout and row-column tuning circuitry. The unit pixel cell contains a grating coupler as a receiving element and mixes the received signal with the reference signal using a hybrid 90° coupler that feeds the in-phase and quadrature output to two balanced detectors. The layout of the system is shown in Fig. 5.5 (b).

There are two thermal tuning nodes per cell and three-bias connections per pixel. The balanced detectors cancel out the strong reference signal and allow a higher

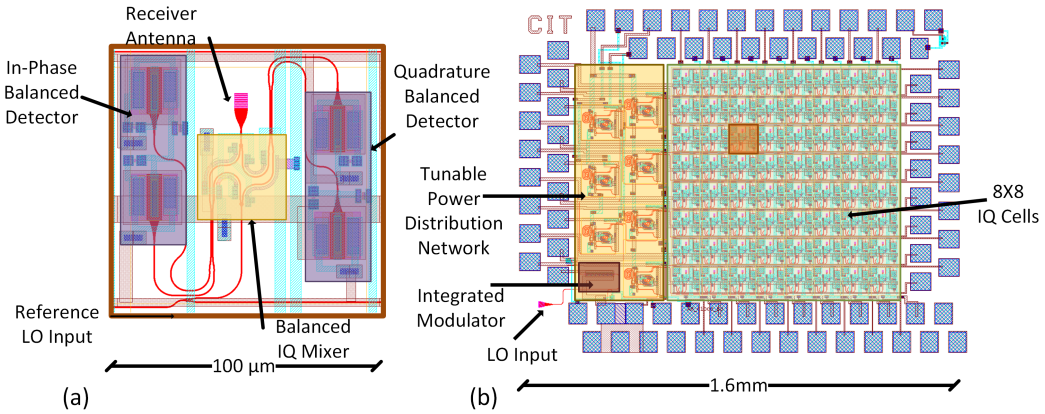

Figure 5.5: IQ chip layout. (a) The layout of the IQ unit cell. (b) Layout of the full chip with 8×8 IQ unit cells and adjustable LO distribution network.

dynamic range. This cancellation relies on the perfect fabrication of the directional coupler and the matched responsivity of the two photodiodes. The consistency and maturity of the CMOS grade photonic fabrication make this possible. The hybrid 90° coupler is a four-port device that produces in-phase and quadrature outputs by incorporating 90° optical phase difference between the mixed signal of the two output ports. The design of the 90° coupler is shown in Fig. 5.5(a). To ensure the reliable fabrication of the 90° hybrid against wafer-level fabrication mismatches and etch gradients, the 90° path length difference was implemented as two 45° phase delays in opposite arms of the 90° hybrid. Any deviation from the ideal 90° phase (ϕ_{error}) can be calibrated per device.

$$I_{in-phase}(t) = 2\alpha E_s(t) E_{LO}(t-\tau) cos(\phi_s - \phi_{LO} + \phi_{fluct}) \tag{5.12}$$

$$I_{quadrature}(t) = 2\alpha E_s(t) E_{LO}(t-\tau) cos(\phi_s - \phi_{LO} + \phi_{fluct} + \pi/2 + \phi_{error}) \tag{5.13}$$

In addition, two small series diode resistors are incorporated in each arm of the hybrid 90° coupler that can be used to correct the phase error term ϕ_{error}. To reduce temperature gradient on chip, each thermal tuner has been broken into two serially connected thermal tuners on opposite arms, as shown in Fig. 5.5(a). Since the thermal tuners only correct for small phase error resulting from the fabrications, the required phase shift and thus the thermal tuner power consumption is significantly reduced. In addition, the number of bends and waveguide lengths is matched in the two paths. Finally, the two outputs of the unit pixel cell have a parallel resistor with

each photodiode and a silicon photodiode in series that allows for the row-column readout of the pixel outputs.

To operate the structure in a row-column fashion with an expandable aperture, three architectures are used: a row-column thermal tuning architecture (Fig. 5.6), a row-column readout architecture (Fig. 5.7), and an adjustable reference signal distribution (Fig. 5.8). A row-column thermal tuning structure incorporating a matrix of series diode-resistors interconnected in a row-column fashion is utilized. Each unit heater shares a common row and column signal with the thermal tuners in the same row and column, respectively (as shown in Fig. 5.6).

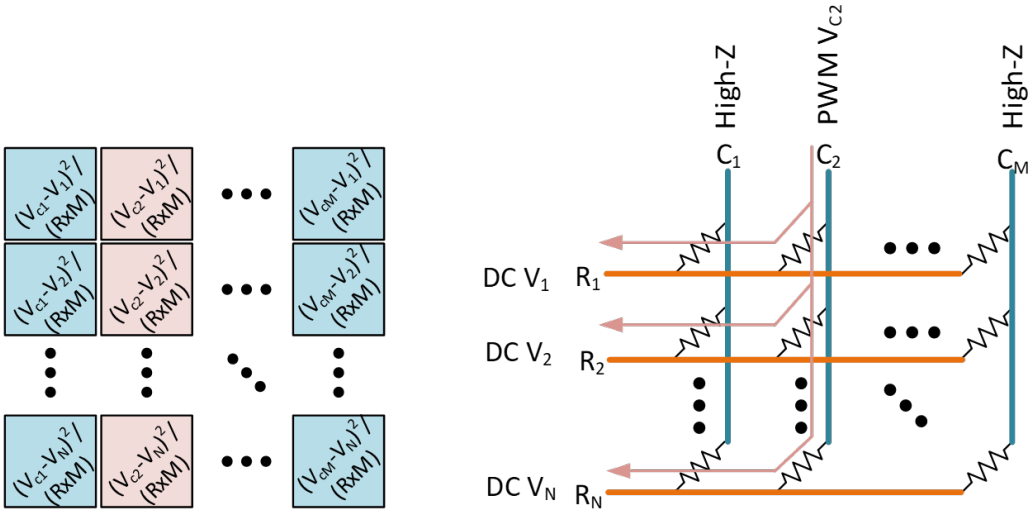

Figure 5.6: Row-column thermal tuners.

Thus, for an array of $N \times M$ heaters, only $N + M$ electrical connections are needed. The thermal time constant of these thermal tuners provides the additional degree of freedom required to independently program these $N \times M$ heaters by incorporating pulse modulation techniques. The thermal tuners are cyclically programmed one column at a time. In each time cycle, each column of thermal tuners receives M times the target power while other columns receive no power. On average, during each cycle, any column receives the target power. A thermo-optic phase modulator has a typical thermal bandwidth response in the order of 10kHz (100μs time constant). An additional factor of 10 was assumed for the thermal modulator bandwidth to reduce ripple in the thermal modulator response. High-speed electronic driver boards are designed to toggle between different settings corresponding to different columns of the row-column thermal tuner matrix. Since the number of columns (M) is 8, a driver board with a switching speed of 2MHz is more than sufficient to toggle

between setting for different columns and allow for independent control of all $N \times M$ heaters. Since there are two thermal heaters per unit cell, the thermal tuning matrix is interleaved, and for every row signal, there are two column signals corresponding to the two heaters per unit cells that are simultaneously programmed per cell.

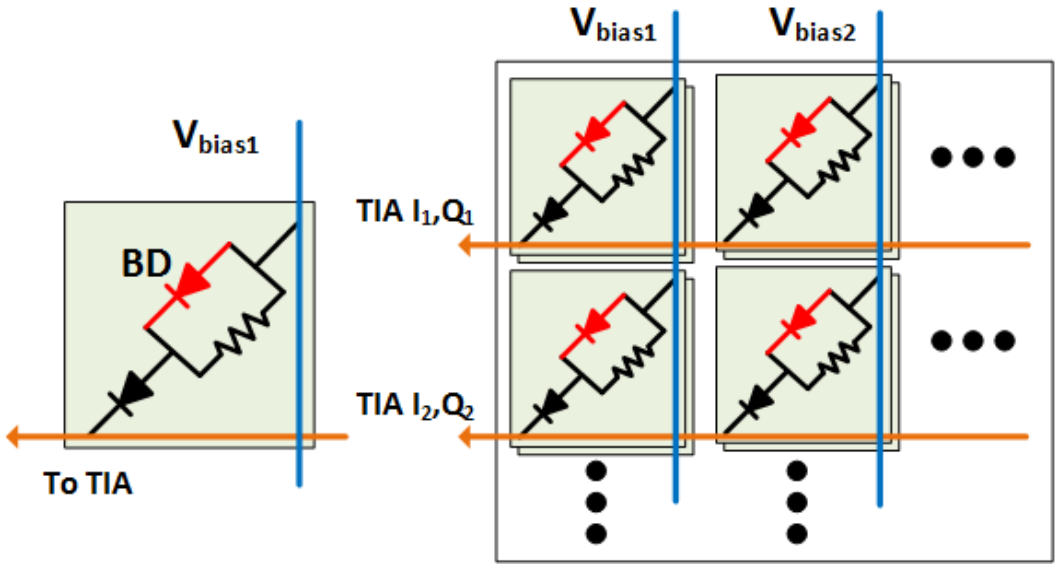

Figure 5.7: Row-column readout architecture.

In addition, a row-column readout architecture is implemented. For an $N \times M$ array of photodetectors, only $N + M$ electrical connections are required. The balanced detectors are reverse biased using two bias voltages common between all the elements in the row. A series silicon diode is put at the output of the balanced detector and is connected to the column signal, which allows one to turn any row of IQ cells on or off, as shown in Fig. 5.7. A parallel resistor is included with each photodiode to prevent charge build-up during the off state, which can degrade the photodiode performance. A set of switches toggle the bias voltage on the row signals. All the rows, except the target readout row, are put in reversed bias, and the silicon diode blocks the balanced photodiode pair's signal from flow in the column signal, which is connected to a low noise trans-impedance amplifier (TIA). Since there are two signals (in-phase and quarature) per unit cell, the row-column readout also incorporates an interleaved row-column matrix with two common photodiode reversed-bias signals per row and two (in-phase and quadrature) signals per column connected to two TIAs. This architecture allows concurrent readout of all the photodiodes in a row, which means that the relative optical phase between adjacent photodiodes can be extracted. This shows the architecture has potential for phase

retrieval applications.

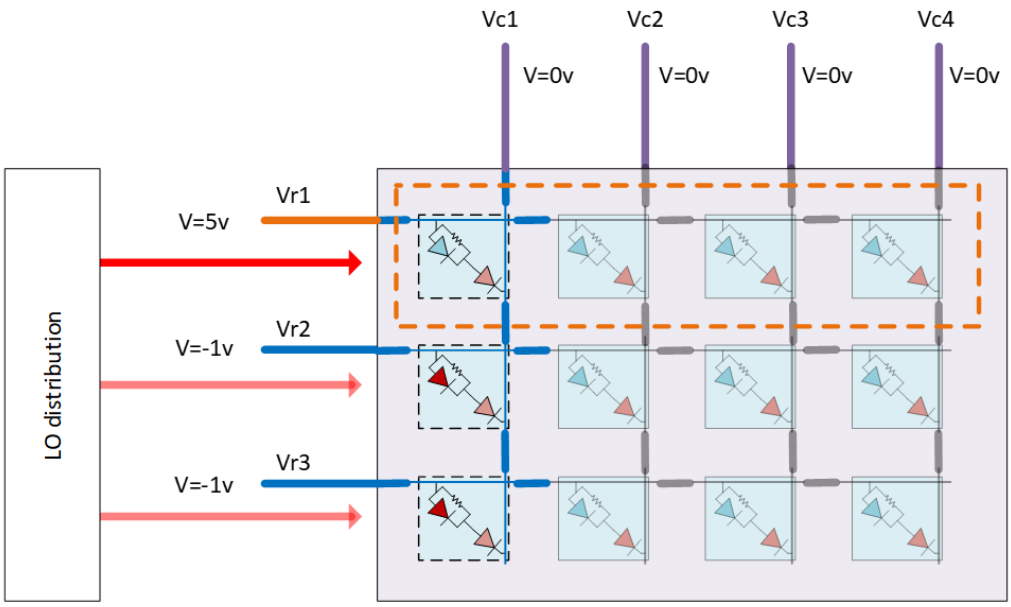

Figure 5.8: LO distribution network for undesired signal suppression from the leakage of other IQ cells in the row.

Finally, given the row-column readout architecture, the residual current leakage from the rows of IQ cells that are inactive at any given time will pose a bottleneck for a large-scale coherent IQ receiver aperture since the cumulative leakage will degrade the SNR. To address this issue, a tunable LO reference distribution network is implemented. A tree-style switching network can redirect the LO power to a given row (Fig. 5.8). This means that the mixed coherent signal from the other rows will be attenuated by the same amount that the reading row is amplified (in terms of LO gain). Furthermore, this tunable LO distribution network reduces the total required power for measurement and operating in the shot noise limited region to the minimum optical LO power required for one row of IQ unit cells. This architecture allows for the expansion of this aperture to a very large size without running into LO power delivery or noise leakage challenges.

5.4 Setup and Measurement

IQ chip was illuminated with a collimated fiber from a 20cm distance, and RF modulated THz/s chirp (2GHz/ms) was generated with an arbitrary waveform generator and applied to the external amplitude. Here ζ=2THz/s and ω_{RF0}=500MHz.

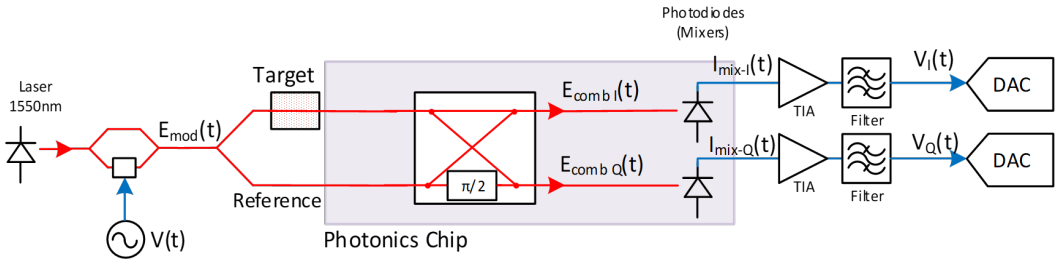

Figure 5.9: The amplitude is modulated using FMCW waveform with 2GHz/ms chirp rate.

$$V_{mod}(t) = cos(\frac{1}{2}\zeta t^2 + \omega_{RF0}t + \phi_{RF}) \tag{5.14}$$

$$E_s(t) = V_{mod}(t)cos(\omega_{opt}t + \phi_{opt} + \Phi(t)) \tag{5.15}$$

$$E_{LO}(t) = E_s(t - \tau) \tag{5.16}$$

$$\sqrt{I_{I^2+Q^2}(t)} = 2\alpha E_s(t)E_{LO}(t - \tau)2\alpha V_{mod}(t)V_{mod}(t - \tau) \tag{5.17}$$

The distance of the illuminated fiber with respect to the chip was varied over 3.5 mm range. The sum term in the mixed component is in the GHz range and is filtered out by the photodetectors. The received signal is amplified and the time-domain signal is captured by an oscilloscope. Chirp reset trigger signal is also connected to the oscilloscope and used as a trigger signal for the mixed received signal.

$$\sqrt{I_{I^2+Q^2}(t)} = 2\alpha cos(\zeta\tau t + \Delta\phi_{RF}) \tag{5.18}$$

The resulting range measurement result is shown in Fig. 5.10.

SEM photos of the IQ imagers' amplitude tuning cell is shown in Fig. 5.11(a). SEM of IQ unit cell is shown in Fig. 5.11(b). SEM image of the hybrid 90° balanced coupler is shown in 5.11(c). Die photo of the chip is shown in Fig. 5.12.

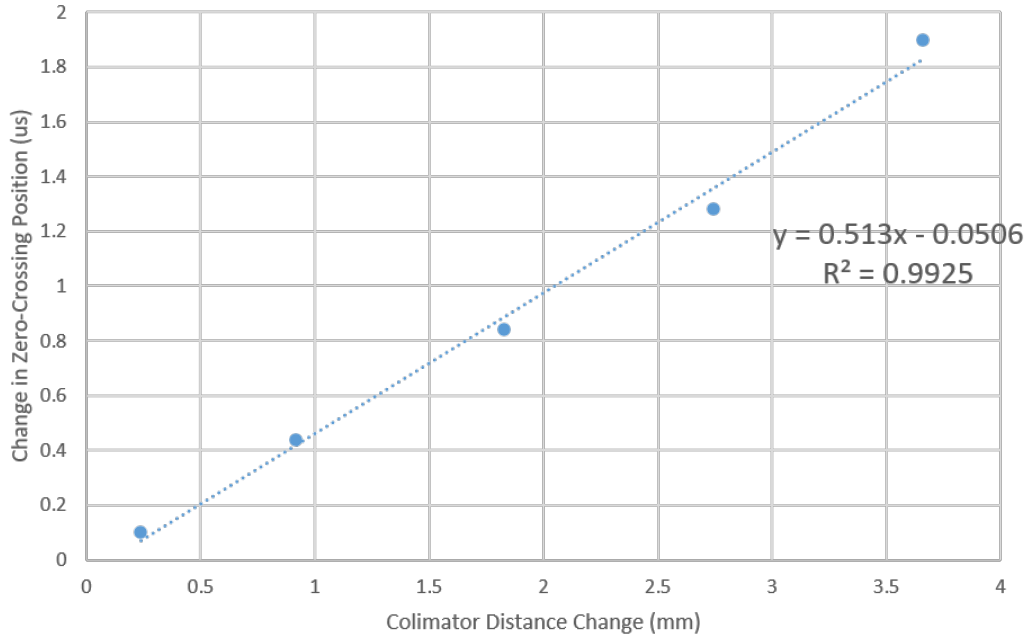

Figure 5.10: Range data. Path length difference between the LO and illumination was increased in linear increments of $600\mu m$.

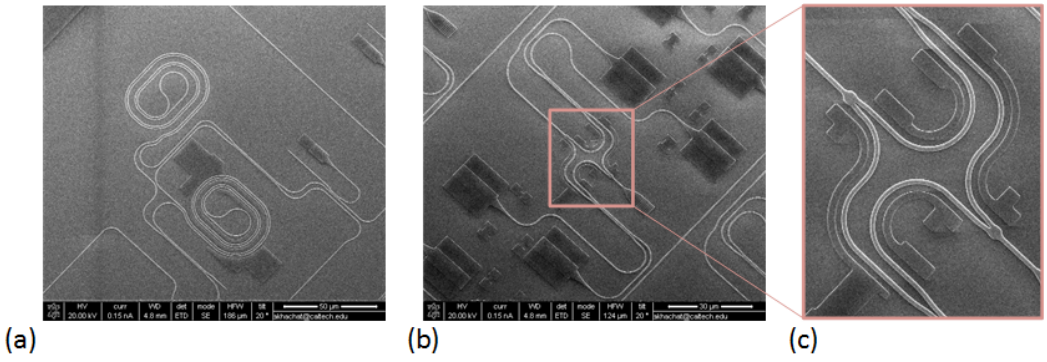

Figure 5.11: SEM images of IQ imager's building blocks. (a) Unit cell of tunable amplitude coupler in the LO distribution network. (b) IQ unit cell. (c) Hybrid 90° balanced coupler.

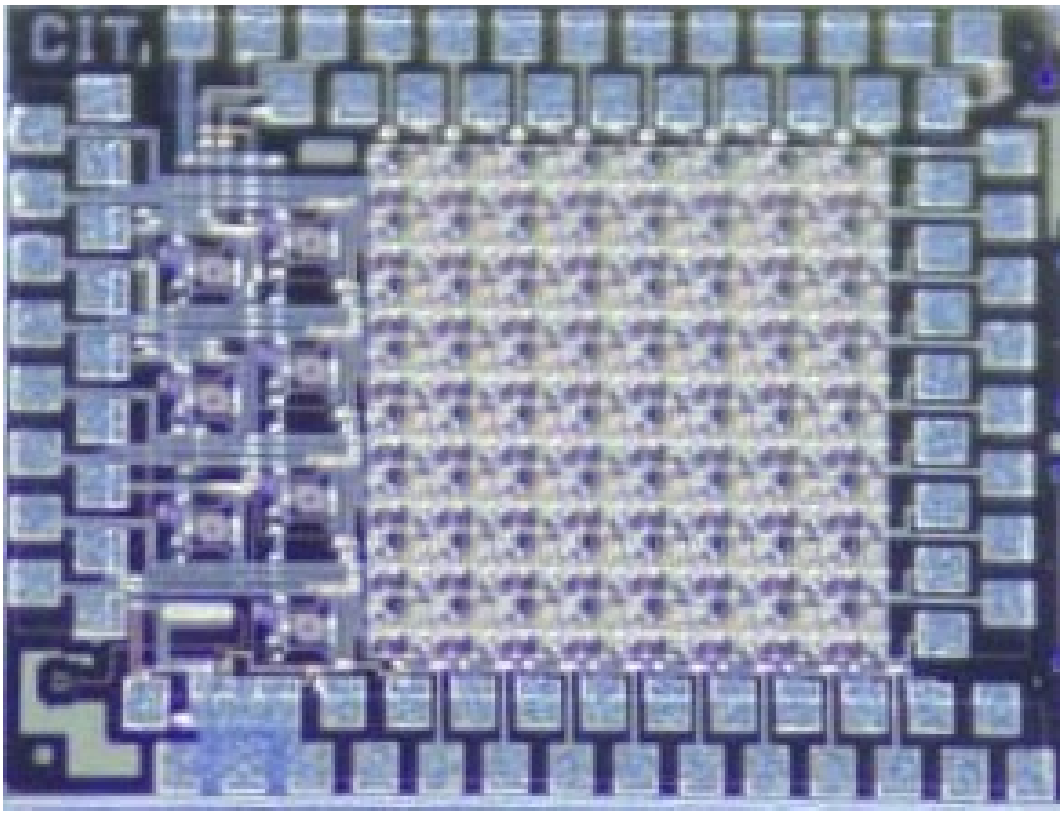

Figure 5.12: Die-photo of the 8×8 IQ coherent imaging chip.

Chapter 6

A COMPACT SPIRAL MACH-ZEHNDER INTERFEROMETER MODULATOR ON SOI PROCESS

Here a small-footprint spiral Mach-Zehnder Interferometer Modulator is designed in a photonics process. This modulator archives 9GHz 3dB-bandwidth using two 3mm-long spirally-wrapped MZI arms in a compact $550\mu m \times 650\mu m$ area, which demonstrated its potential for high-density integration[1].

6.1 Introduction

In high-speed communications, due to the long modulator dimensions, the propagation difference speed of the optical and electrical signals becomes critical and negatively affects the modulator performance. Mach-Zehnder interferometers (MZI) address this issue and are widely used in optical communication networks for high-speed optical signal modulation. Integrated photonics systems typically use PN modulators. These PN structures implemented as traveling-wave modulators are several millimeters long [87], [88], which causes the MZI structures to have high aspect ratios and consume a large silicon area. This is problematic for high-density silicon-photonics integration where total signal routing on-chip and the entire chip area are expected to be minimized. In addition, at least one dimension of the chip is required to be several millimeters, which makes them impractical from a electrical drive perspective. Our proposed architecture created a compact, area-conserving spiral MZI modulator with an aspect-ratio of 1.2, making it practical for high-density integration. This is achieved by wrapping the 3mm-long modulator from a straight form into a spiral shape.

6.2 Design

Figure 6.1 (a) shows the die-photo of the proposed spiral MZI. The input and output ports of the MZI are placed on the outside of the spiral MZI for high-density integration. The 90nm slab is alternatively doped as p-type and n-type doped regions in between the 220nm optical waveguides for compact routing. p- and n-doped regions are reverse biased to form PN carrier-depletion type phase shifters in each interferometer arm. The two PN diodes are connected serially to

[1]This work was done in collaboration with Behrooz Abiri.

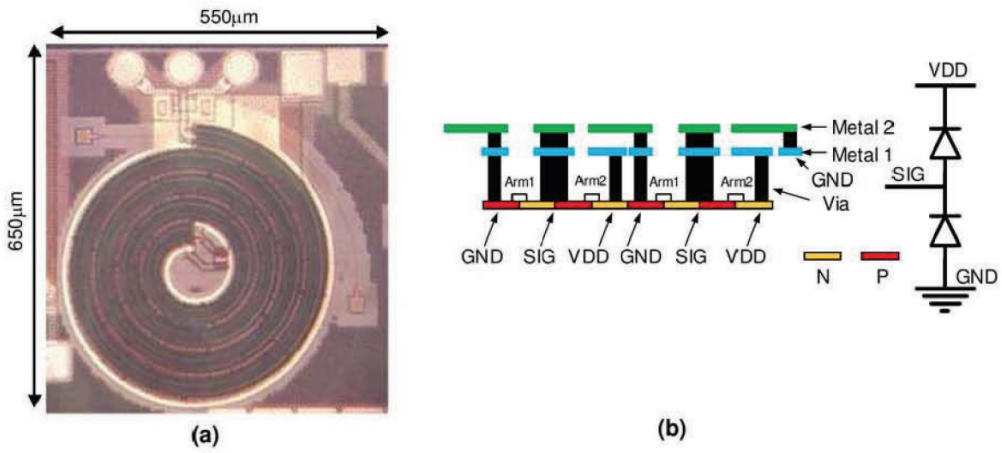

Figure 6.1: (a) Die photograph of the fabricated chip. (b) Partial cross section of the MZI structure demonstrating the capacitance between VDD and GND. The spiral MZI allows for a push-pull operation of the phase shifters.

allow for modulator push-pull operation with a single external driver. The partial cross-section of the MZI structure for two turns of the spiral is shown in Fig. 6.1(b). A co-planar electrical transmission line, which is capacitively loaded by the PN junction, delivers the electrical drive voltage to the modulator. This capacitive loading of the transmission line reduces the propagation speed of the electrical signal. It is taken into account in the design to reduce velocity mismatch between electrical and optical waves. Furthermore, to reduce the cross-talk between co-planar adjacent signals in the spiral, each signal is shielded by two grounds from each side. Finally, the ground plane is extended over the supply (VDD) line to act as a distributed bypass capacitor reducing the supply voltage ripple. The electrical wave is terminated at the center of the chip via an integrated 50Ω resistor.

6.3 Measurements

The chip was fabricated in the IME process via OpSIS. The fabricated test chip, shown in Fig. 6.1(a), confines two parallel 3mm-long PN phase shifters in an area less than $550 \times 650 \mu m^2$. The DC response of the modulator is shown in Fig. 6.2(a) with $V_{\pi L}$ of $2.27\,\mathrm{V} \cdot \mathrm{cm}$ An electrical VNA with a calibrated 35GHz photodiode is used to measure the AC response of the spiral MZI (Fig. 6.2(b)). We measured a 3 dB modulation bandwidth of 9GHz. The mismatch between the impedance of the traveling wave electrical transmission line and the integrated on-chip termination results in the ripple in the frequency response of the modulator. NRZ data transmission eye diagrams for 12.5Gbps and 20Gbps are shown in Fig.

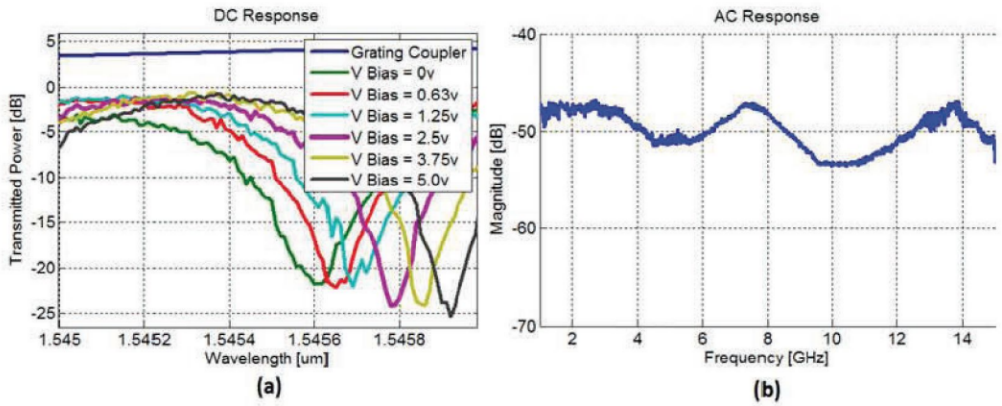

Figure 6.2: (a) Measured DC response of the modulator. (b) Measured frequency response of the modulator.

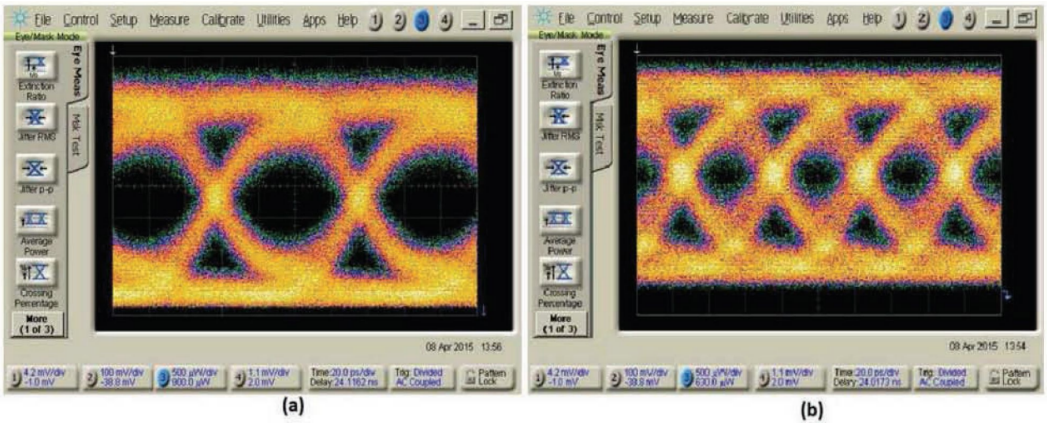

Figure 6.3: (a) l2.5Gbps eye diagram, (b) 20Gbps eye diagram.

6.3(a) and Fig. 6.3(b).

Chapter 7

MONOLITHIC MACH-ZEHNDER INTERFEROMETER MODULATOR IN AN UNMODIFIED CMOS PROCESS

In this work, a compact, monolithically-integrated MZI modulator operating using PIN phase shifters is demonstrated to operate above 1Gbps. This device is implemented in an unmodified 180nm CMOS electronics SOI process. This compact $50\mu m$-long structure allows for high-density integration of high-speed photonics modulators and electrical driver circuitry on a single standard CMOS chip for data communication applications[1].

7.1 Introduction

Integrated data communication solutions are typically implemented using electronic and photonic chips that are integrated on different platforms. In this situation, each process is optimized for each sub-system performance independently but suffers from interconnect parasitics problems. Monolithic solutions can remove chip-to-chip interconnect parasitics and reduce system packaging complexity [89]. Monolithic integration of silicon photonic devices with electronics has been previously demonstrated in 45nm IBM SOl process [90]. However, this process has a $100nm$-thick bottom oxide layer and requires post-processing to remove the silicon substrate to allow for optical wave propagation in O and C bands. The CSOl7RF process with $1\mu m$ bottom oxide layer has an insignificant optical coupling to the substrate at communication wavelengths of 1550nm and 1310nm [91]. For this process, grating couplers for coupling light into and out of the modulator have been previously demonstrated [91]. No active devices have been presented on the platform. Mach-Zehnder interferometers (MZI) are widely used in optical high-speed communication systems. For the first time, a compact MZI modulator has been designed in 180nm CS0I7RF process with 510MHz bandwidth and 1.25Gbps data transmission rate.

7.2 Design

Fig. 7.1(a) shows the die-photo of the proposed compact MZI structure. Laser light at 1550nm wavelength is coupled into and out of the chip via grating couplers. Each

[1]This work was done in collaboration with Behrooz Abiri and Andy Zhou.

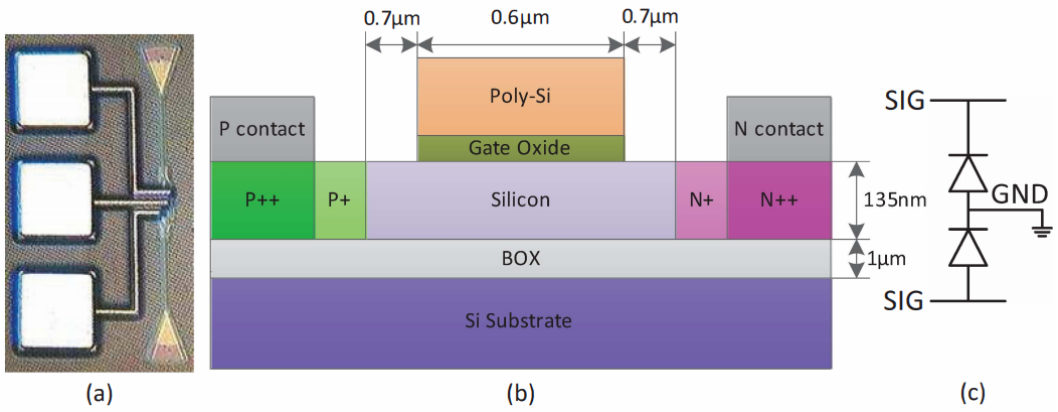

Figure 7.1: (a) Die photograph of the 50μm-long amplitude modulator. (b) Cross-section of the MZI structure depicting the doped regions as well as the dimension of the modulator device. The poly-silicon layer on silicon structure confines the optical mode in the PIN structure. (c) Electrical connectivity of the PIN diodes. Back-to-back diodes allow the modulator to operate in a push-pull fashion.

arm of the interferometer modulator is a PIN diode, as shown in Fig. 7.1(b). The core of the waveguide is minimally doped to reduce the insertion loss. The process's poly-silicon layer helps contain the mode in the core of the waveguide. The thin gate oxide of a few nanometers has a negligible effect on the optical field. Forward-biasing the PIN diodes results in current flow through the silicon that changes the refractive index of the interferometer arm for modulation. PIN modulators are connected back-to-back as shown in Fig. 7.1(c) to operate in a push-pull fashion. The common node of the modulators is grounded while the the other two terminals are driven via two external RF sources. Alternatively, the two outer nodes can be biased, and the center node can be operated using a single RF source.

For this structure, we measured a propagation loss of 14 dB/cm for the 500nm-wide waveguides, 10 dB/cm for the 600nm-wide waveguides, and 8 dB/cm for the 1.5μm-wide waveguides. Surface roughness of the waveguides is the primary cause of loss in these waveguides. The standalone poly-silicon layer has an insertion loss of 55 dB/cm. The high loss of the polycrystalline silicon is due to grain boundary scattering. Y-junctions for power splitting and combining introduces 0.47 dB of excess loss.

7.3 Measurements

DC and AC response of this modulator and high-speed data transmission is characterized for this modulator. The DC response of the modulator is shown in Fig.

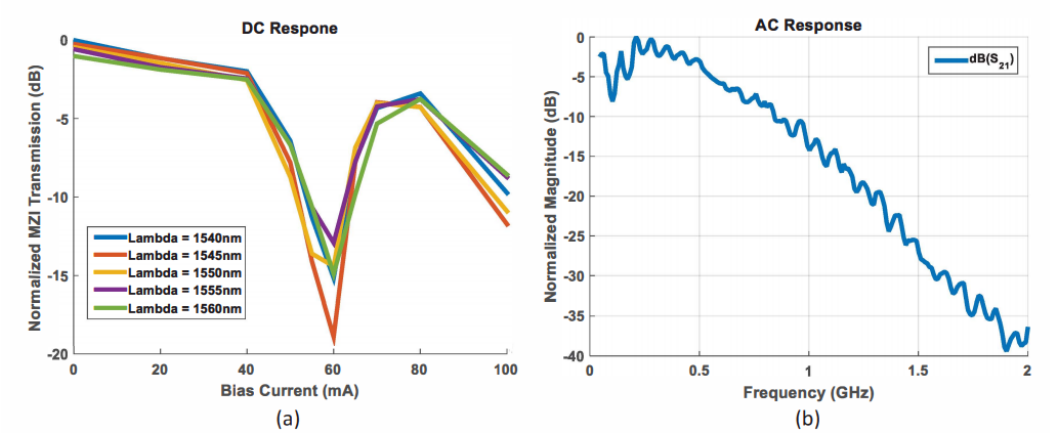

Figure 7.2: (a) Measured DC response of the modulator. (b) Measured frequency response of the modulator.

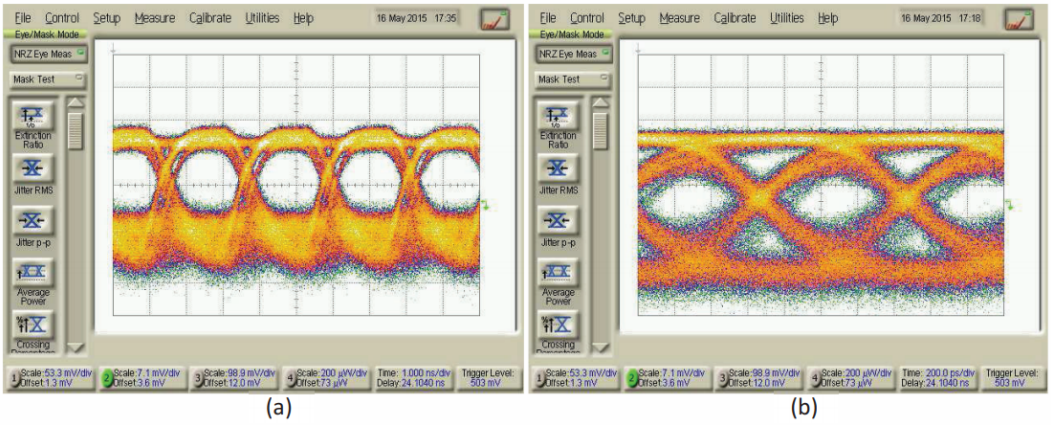

Figure 7.3: (a) 900Mbps eye diagram without pre-emphasis. (b) 1.2SGbps eye diagram with pre-emphasis.

7.2(a). Equal-length modulator arms of the interferometer result in less sensitivity to the operation wavelength. AC response is characterized using an electrical VNA and a 35GHz external photodiode. The measured frequency response is shown in Fig. 7.2(b). The 3dB bandwidth of the modulator is 510MHz. Without pre-emphasis, we demonstrate the NRZ modulation eye diagram at 900Mbps, as shown in Fig. 7.3(a). With pre-emphasis and adjusting the first and second post-tap coefficients, we demonstrate an open eye at 1.25Gbps, as shown in Fig. 7.3(b).

Chapter 8

HIGH-SPEED SLOW-WAVE MODULATOR USING CORRUGATED WAVEGUIDES

In this chapter, a compact MZI modulator using corrugated waveguides employing slow-wave architecture is used to reduce modulator $V_{\pi L}$. This structure exhibits 80% enhancement in extinction ratio in slow-wave operation and achieves 14GHz bandwidth for 1 mm-long structure[1].

8.1 Introduction

Improving the size, power consumption, and modulation efficiency of integrated modulators is important in meeting the demand of exponentially growing traffic in data-communication and telecommunication. Integrated ring and interferometric modulators can be integrated at a low cost with high production yield in standard CMOS compatible photonic processes to meet this growing demand [92], [93]. MZM modulators offer a higher extinction ratio, high bandwidth, and high tolerance to process and environmental changes [94]. However, the modulation efficiency of these structures is very low (high $V_{\pi L}$), resulting in a large footprint. This results in a design trade-off between the modulator length and electrical driver complexity. To break this trade-off, we incorporate a slow-wave waveguide in a traveling wave MZI modulators. Previously, slow-light modulators have been used to improve modulation efficiency [95], [96]. In this work, corrugated waveguide modulators utilizing the band-edge slow-light effect are designed to improve the modulator extinction ratio at a reduced electrical drive voltage.

8.2 Design

The slow-wave MZM is fabricated in BiCMOS monolithic IHP microelectronics. The corrugated waveguide, modulator cross-section, as well as the perspective view of the modulator is shown in 8.1(a). The dimensions of the corrugated waveguide are as follows: main rib width 340nm, corrugated rib width 170nm, period 300nm, corrugated period 150nm, rib height 220nm, and slab height 120nm. The electrical bandwidth of the structure is simulated by using an equivalent circuit model for

[1]This work was done in collaboration with Reza Hoesseini, Mircea Catuneanu, Parham Porsandeh Khial, Reza Fatemi, and Professor Kambiz Jamshidi.

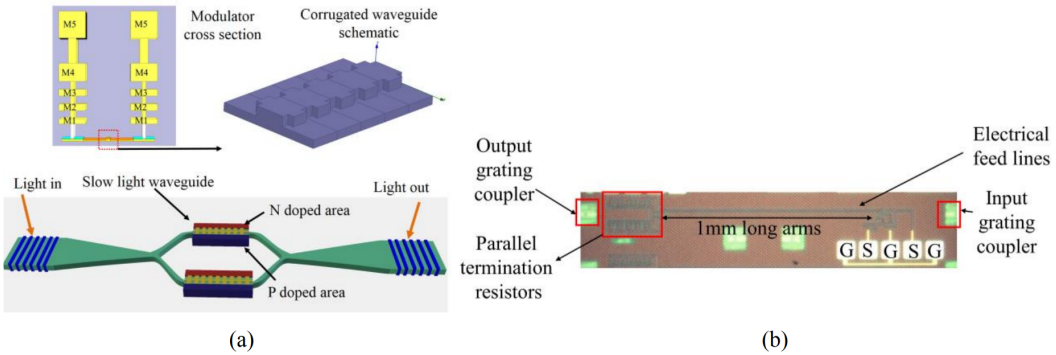

(a) (b)

Figure 8.1: (a) Schematic of the proposed corrugated-base slow-light modulator, modulator cross-section view, and schematic of corrugated waveguide. (b) The die photo of the modulator.

the slow-wave PN modulator incorporated into the traveling wave structure for the modulator [97], [98]. The increased effective index in the corrugated waveguide region results in an increased modulation efficiency and reduced drive voltage requirements.

This modulator uses a concentration of $5 \times 10^{17} cm^{-3}$ acceptors and donors to create the 1mm long PN junction. An electrical drive signal is applied to the modulator via GSGSG probe. The traveling-wave is terminated using integrated parallel resistors to prevent back-reflection of the electrical wave. The termination resistors are implemented as a bank of several resistors that can be trimmed for post-fabrication tuning. Simulation results [99] indicate 15GHz bandwidth with $2\ \mathrm{V} \cdot \mathrm{cm}$ modulation efficiency for the short 1mm-long modulators.

8.3 Measurements

The optimum operation bias voltage and wavelength for the modulator is extracted via DC measurement, as shown in Fig. 8.2. This device requires 2.49V to achieve 2π phase shift at 1532.1nm while requiring 1.76V at 1533.7nm, which is the center frequency of the slow-wave operation regime. A calibrated 40GHz photodiode in conjunction with an electrical VNA is used to measure the AC response of the modulator 8.2(b). The electro-optical bandwidth of the modulator was measured to be 14GHz, as shown in Fig 8.2(c). A sampling oscilloscope in conjunction with an PRBS signal generator was used to capture the modulated eye-diagram. The eye diagram for NRZ PRBS7 modulation at 5Gbps without applying pre-emphasis is shown in Fig. 8.2(e). The modulation output extinction ratio for constant drive voltage was measured at several wavelengths, as shown in Fig. 8.2(d).

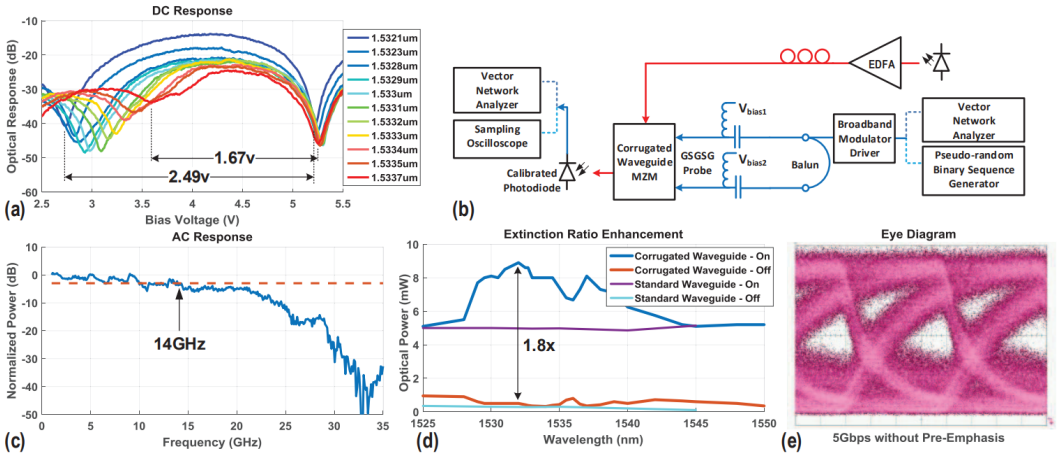

Figure 8.2: (a) DC response of the corrugated waveguide modulator. (b) Characterization setup. (c) AC response of the modulator. (d) Measured extinction ratio of the modulator at 1.25GHz. (e) Eye diagram for NRZ data transmission at 5Gbps.

This measurement shows an 80% enhancement in extinction ratio in the slow-wave operation region compared to standard rib waveguide modulators.

8.4 Discussion

We demonstrated extinction ratio enhancement of 80% in the corrugated waveguide modulator while maintaining 3dB bandwidth of 14GHz. The modulation efficiency improved by 67% in the slow-wave operation region of the modulator at 1533.7nm because of the enhanced group index. The dominant pole of the modulator was beyond 14GHz, revealing that the bandwidth of this structure can be further enhanced in future designs by reducing the impedance mismatch between the optical and electrical paths.

Chapter 9

HIGH-EFFICIENCY POLYMER-BASED MODULATORS

A compact, high-speed silicon-organic hybrid modulator based on active electro-optic chromophore with a novel low-loss and high-fabrication tolerance mode-adapter is designed and implemented for high-complexity photonic signal processing. A high-speed complex waveform modulator and two OPA systems are designed using this modulator[1].

9.1 Introduction

Hybrid integrated electro-optic signal processing has revolutionized the field of high-speed optical fiber data transfer for data-communication and telecommunication applications (Fig. 9.1), resulting in 10X fiber capacity improvement every five years. Furthermore, this platform holds the potential to transform optical coherent imaging and sensing systems for autonomous vehicles, robotics, automation, and medical imaging applications. Typically, these hybrid optical-electrical systems include many components and sub-systems such as coherent laser sources, electrical drivers, photonic waveguides, detectors, modulators and photonic signal splitters and combiners. Each of these components needs to be optimized and co-designed to achieve an overall low loss since amplification in photonics is very power-hungry and will reduce system efficiency significantly. Each of these components and sub-systems is actively investigated and improved. However, despite good advancement in laser efficiency and stability, advanced driver architectures, and high efficiency passive photonic components and photodetectors, electro-optic signal modulation performance is still limited and poses a bottle-neck for high-complexity signal processing.

While for optical fiber communications, the goal is to maximize the capacity of data transmission per fiber (Fig.9.2(a)), high-density integration faces a different set of constraints. In dense photonic integration – where a large number of these photonics devices will be interconnected electrically and optically – chip footprint, power consumption, electrical driver requirement, and insertion loss are the performance metrics that need to be optimized simultaneously, as shown in Fig. 9.2(b)).

[1]This work was done in collaboration with Reza Fatemi, Dr. Delwin Elder, and Professor Larry Dalton.

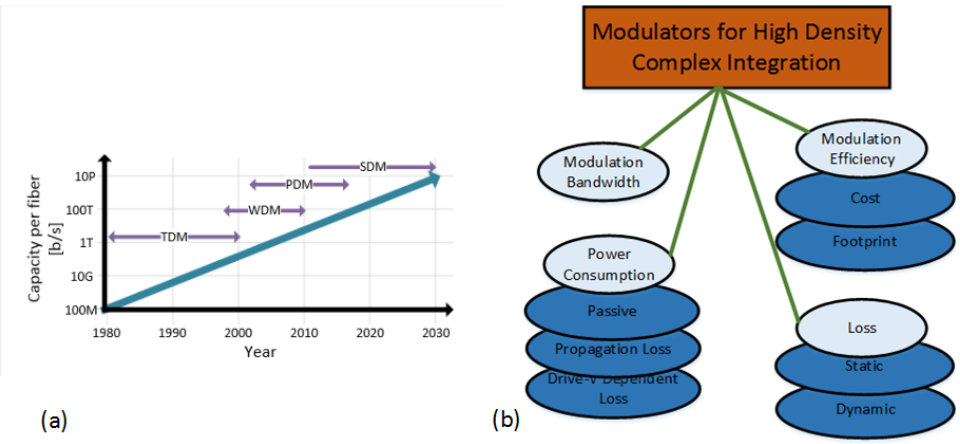

Figure 9.1: High-bandwidth modulation. (a) Trends in high-bandwidth optical modulation [100]. WDM, multi-level coherent modulation, and now SDM have enabled exponential growth in fiber data capacity. (b) Block diagram of factors important for complex high-density modulation.

Henceforth, modulators that consume static DC power such as thermal and forward-bias PIN modulators [17], [101] or have a limited modulation bandwidth such as liquid crystals modulator [102], are poor candidates. Furthermore, modulators that efficiently operate only as amplitude modulators such as electro-absorption modulators based on Franz-Keldysh effect [36] are not suitable for the most complex, high-density applications.

In the first category, the modulators are fabricated as part of the CMOS-compatible integrated photonic process without any post-processing and wafer-bonding requirements. The most common family of these modulators is silicon modulators operating based on plasma dispersion (charge injection, depletion, or accumulation) [101], [103], [104]. These modulators suffer from an inherent coupling between amplitude and phase modulation due to Kramers–Kronig relations and large footprint [43], [105]. Some recent developments are using reverse-biased PIN modulators (based on 3rd-order nonlinearity in silicon which can operate as induced $\chi^{(2)}$ nonlinearity) [106]. Despite their large footprint, they satisfy the remaining requirements for high-density integration. Finally, despite having better performance compared to silicon modulators, InP modulators are not directly CMOS-compatible [107].

On the other hand, several silicon hybrid structures incorporating high second-order non-linearity (Pockel's coefficient) materials have been considered in industry and

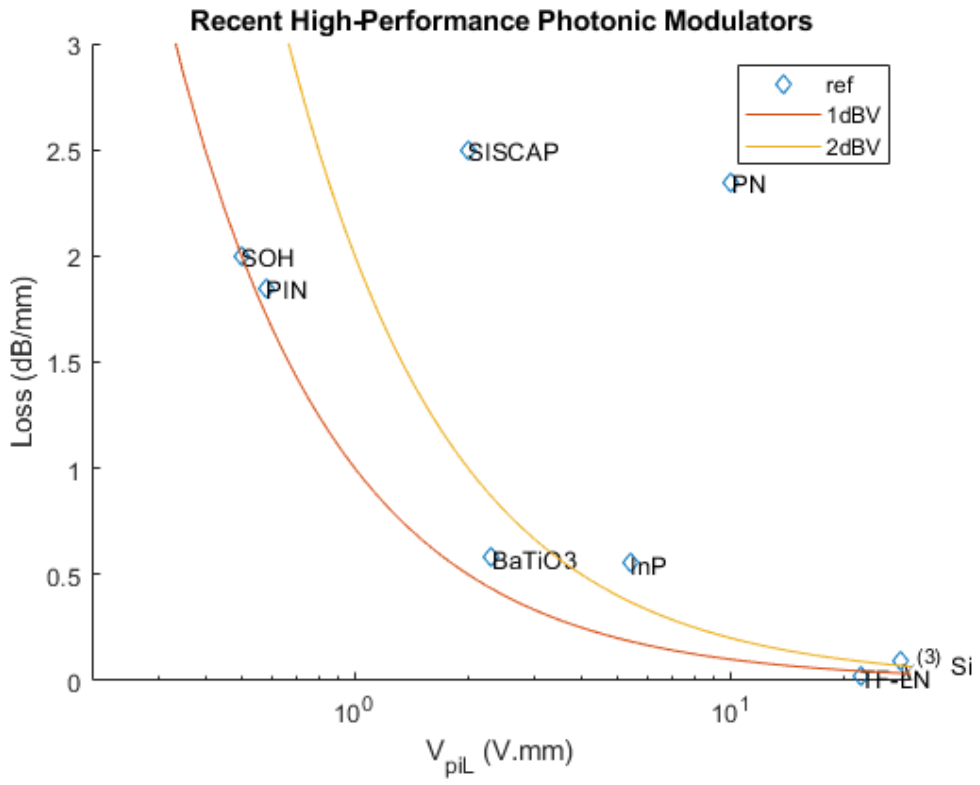

Figure 9.2: Comparison of recent modulator trends. It is desirable to operate below the 1dBV line while maintaining a low $V_{\pi L}$ to ensure small footprint drive voltage product. It is important to note that PIN modulators, despite being close to the performance of SOH modulator, have static power consumption. On the other hand, thin-film Lithium Niobate (TF-LN) [108] requires e-beam lithography for fabrication and hence is not suitable for large-scale CMOS-compatible platforms. High-performance InP modulators cannot be co-integrated with silicon photonics devices in the same fabrication process [109].

literature. These materials are integrated by either flip-chip or wafer-bonding InP, BaTiO3, and Lithium Niobate onto silicon [110]–[112], or they are spin-coated, such as liquid crystal and organic polymers. From the aforementioned hybrid structures, liquid crystals have the highest Pockel's coefficient but, as mentioned earlier, have slow modulation speeds (typically in 100kHz range) [102]. Spin-coated SOH modulators [113] are the only modulators that satisfy all the requirements for high-density integration and don't require complex wafer bonding and post-processing. Various challenges with the long-term stability of silicon-organic-hybrid modulators have been addressed (such as crosslinking in post-poling for long-term stability) [114]. Several studies have examined the long-term stability and tolerance of these modulators under stress and environmental variations [115], [116]. A

summary of the performance comparison of the best performing modulators appears in Fig. 9.2. In this work, SOH modulators using a novel strip-to-slot mode converter with lower loss and better fabrication tolerance are designed. Two variations of this SOH modulator have been proposed. The first kind with higher series resistance and lower optical loss is used for sub-GHz applications such as high-speed optical phased array beamforming. The second kind is designed as a traveling-wave structure for high-speed applications with higher optical loss, and is used to demonstrate complex optical waveform generation capability.

In this chapter, SOH modulator propagation mode and efficiency are examined. Then, the design of the strip-to-slot mode adapter is explored. Various sources contributing to SOH modulator loss are analyzed. Finally, several system designs implemented in this platform are described.

9.2 SOH Modulator Implementations and Modulation Efficiency

Polymer material can serve as an integrated modulator core (Fig. 9.3 a,b) [117], clad in a strip waveguide (Fig. 9.3 c), or, as mentioned earlier, slot dielectric in slot waveguides (Fig. 9.3 d).

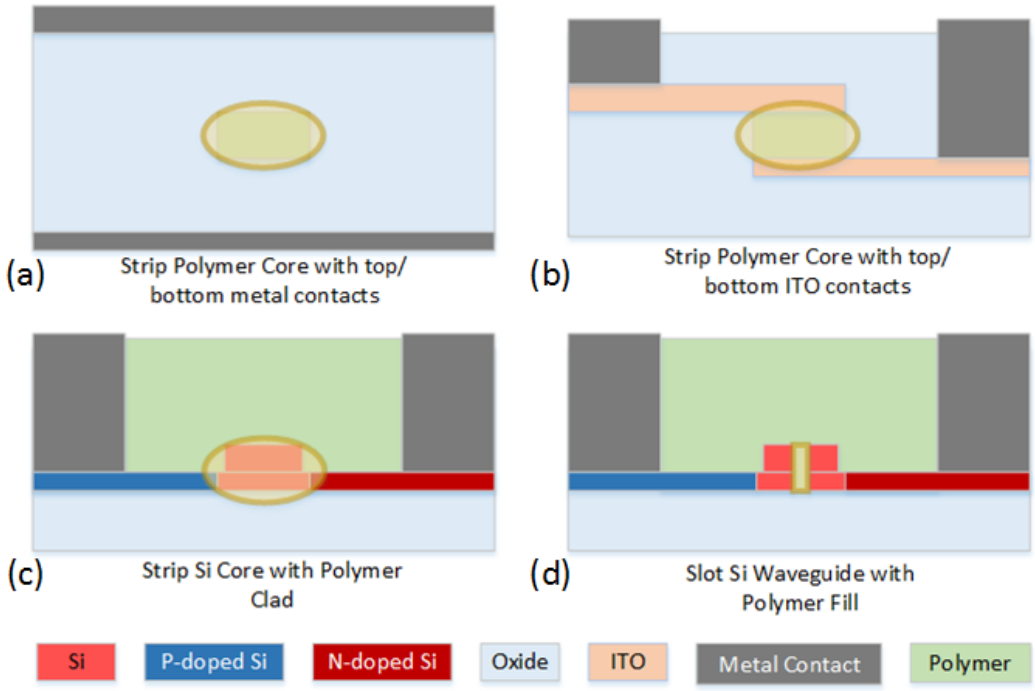

Figure 9.3: Examples of SOH modulator topologies. (a) and (b) polymer is the core of the propagation waveguide, (c) polymer is the clad above the waveguide, and (d) polymer is in the slot of the polymer waveguide.

A standard method of SOH modulator implementation, used for industrial applications [118], is to create a polymer core with oxide cladding with top and bottom electrodes to apply the electric field. Here the electric field strength is reduced since there is a minimum spacing requirement between the electrodes and the optical core to reduce optical loss, which reduces the strength of the applied electric field, resulting in high $V_{\pi L}$. Another method involves improving the electric field using ITO as top cladding [119]. Furthermore, a waveguide core using intrinsic process material such as silicon can be covered with polymer as cladding material. These devices are suitable for silicon photonic integration; however, due to the low field-confinement factor in the clad or even in the core, these devices exhibit high-drive voltage requirements. However, the polymer slot waveguide modulator offers good modulation efficiency due to the high confinement of the electrical and optical fields [120]. These type of SOH modulators exhibit low $V_{\pi L}$ (0.5 V $\cdot$ mm) values.

The propagating mode for the slot waveguide can be calculated in the simplified 1D version to understand the propagation modes [121]. For the target materials in integrated silicon photonics ($n_{Si}(3.4) > n_{Polymer}(1.8) > n_{Oxide}(1.4)$), the slot supports both even and odd modes of propagation. It is desired for the even mode to propagate since the overlap between the optical and electrical fields are maximum. An example of the 1D cross-section of the mode solution for typical slot dimensions (Fig. 9.4) and a 2D mode solution for fundamental even TE mode of the slot modulator is shown (Fig. 9.5 (b)). Fig. 9.5(c) depicts the electrical field profile in the slot region. Comparing Fig. 9.5 (b) and (c) shows that both electric and optical fields overlap in the same region.

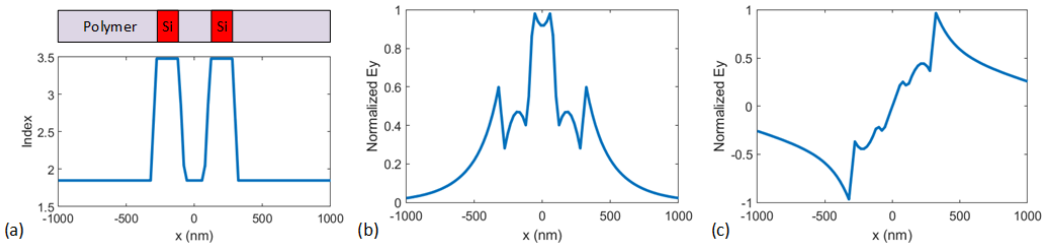

Figure 9.4: 1D cross-section of slot waveguide mode confinement [121]. (a) 1D cross-section of relative refractive-indexes. (b) Even propagation mode in the slot waveguide. (c) Odd propagation mode in the slot waveguide.

The relative efficiency of mode confinement in the slot waveguide can be quantified by the field-interaction factor (Γ) [39], which is a metric for the overlap of the optical and electrical fields.

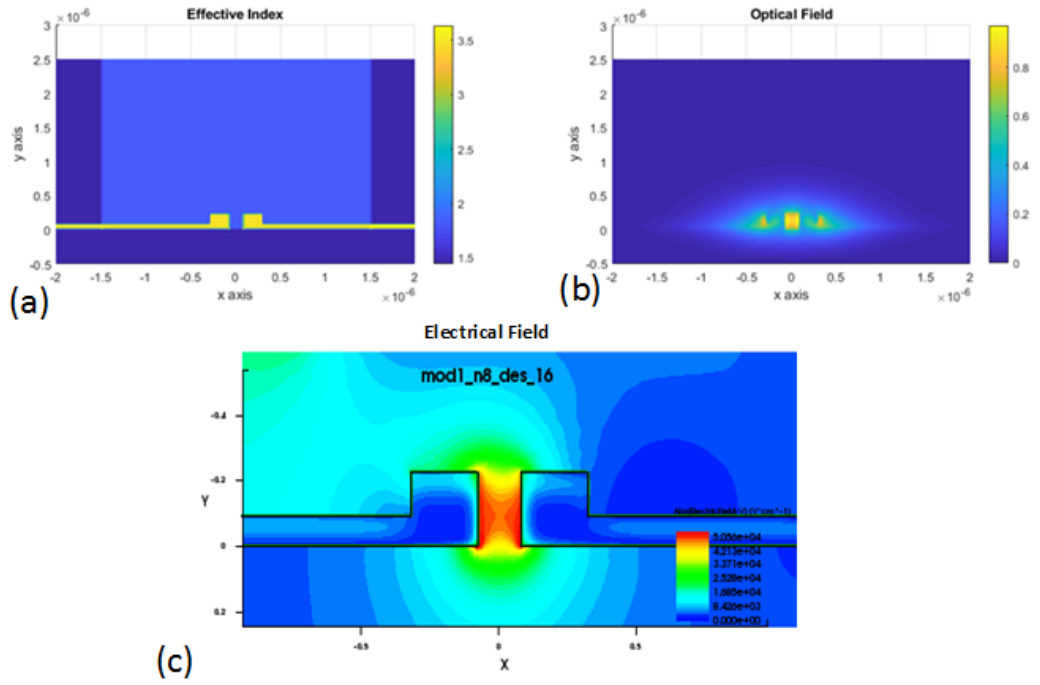

Figure 9.5: 2D electrical and optical mode solution for slot waveguide with slab boundary conditions. (a) Refractive index profile of the slot modulator, (b) optical field profile, and (c) electrical field profile in the slot region.

$$\Gamma = \frac{\int_{Ufieldarea} n/Z_0 |E_x|^2 dV}{\int \alpha R (E \times H^*).e_z dA} \tag{9.1}$$

The higher the Γ value, the higher the modulation efficiency. $V_{\pi L}$ of the modulator is inversely proportional to Γ (9.2).

$$V_{\pi L} = \frac{\lambda W_{gap}}{n^3 r_{33} \Gamma} \tag{9.2}$$

This enhanced modulation efficiency from high optical field confinement in the slot region comes at the cost of increased propagation loss (induced by the surface roughness).

9.3 Strip-to-Slot Mode Adapter

Typical silicon photonic platforms utilize strip waveguides. A mode adapter is required to incorporate a slot waveguide modulator in a standard process. A very high-efficiency strip-to-slot mode adapter with loss of 0.02 dB is previously re-

ported [122]. This low-loss asymmetric strip-to-slot mode converter with adiabatic logarithmic tapering assumes a 120 nm slot width, which is not accessible in all foundry-based photonics platforms. This mode converter starts as a strip waveguide, converts into a one-sided rib waveguide, and finally to a rib-slot waveguide at the end of the adapter region, as shown in Fig. 9.6.

Figure 9.6: Strip-to-slot mode adapter with slab.

Given the parameters of standard foundry-based CMOS photonics platforms (160 nm minimum feature size), the architecture in [122] was proven to be lossy in simulation. At the end of the strip-to-slot mode adapter, there was a significant fraction of odd propagation mode in the waveguide. This will impact the modulation efficiency. However, removing the 90 nm slab region results in low-loss strip to even-slot mode conversion, as shown in Fig. 9.7. After achieving even mode in the strip-slot region, a symmetric taper converts the mode to rib-slot mode, where the electric field can be applied to the modulator.

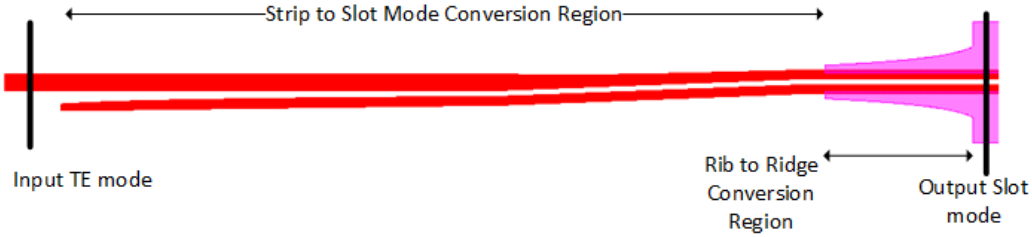

Figure 9.7: Modified strip-to-rib-slot mode adapter.

The insertion loss of this adapter is simulated using two back-to-back mode adapters. The z-cross-sectional electric field profile in log and linear scale is shown in Fig. 9.8.

In this design, with 24μm-mode-adapter length, an insertion loss of 0.6dB for two back-to-back mode adapters (0.3dB for a single-mode adapter) is simulated.

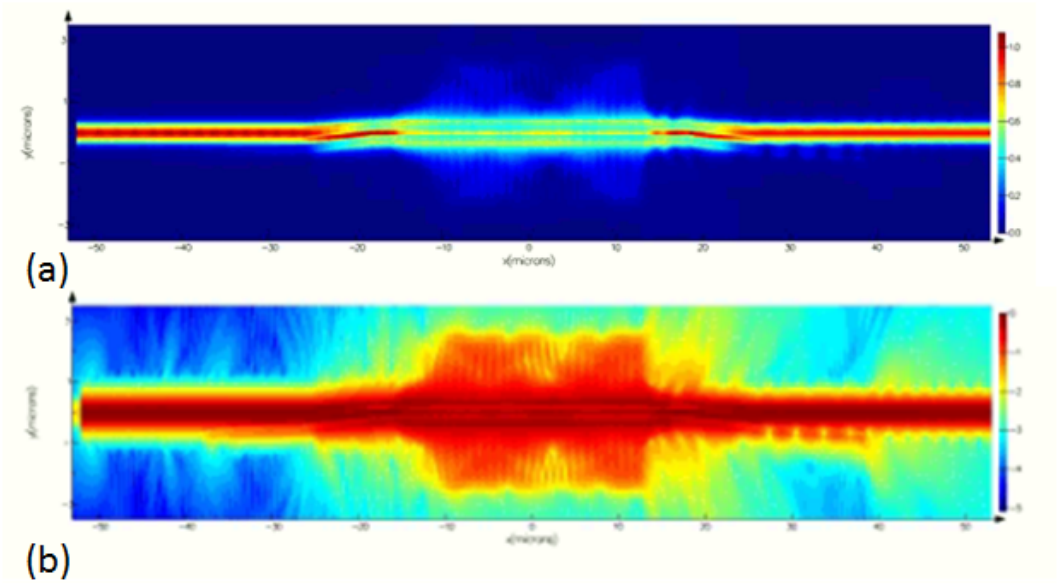

Figure 9.8: End-to-end insertion loss simulation for slot-mode modulators (z-axis cross-section). (a) Electrical-field distribution in linear scale. (b) Electric-field distribution in logarithmic scale.

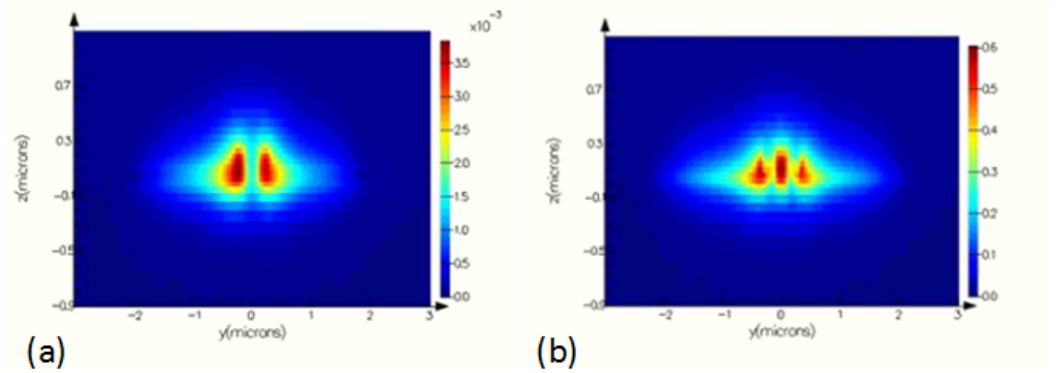

Figure 9.9: Resulting H-field (left) and E-field (right) after the strip-to-slot mode adapter in the modulation region.

The resulting E and H fields in the slot region are shown in Fig. 9.9 (a) and (b) respectively. This modulator has 0.7dB/mm propagation loss in the slot-mode region due to modulator doping and leakage. For a 5V drive voltage requirement for 2π phase shift assuming 1 V $\cdot$ mm modulation efficiency, a $400\mu m$-long modulator is required. The combined effect of coupling and propagation loss aggregates to a total of 0.88dB insertion loss in this modulator. This loss can be further reduced by utilizing a lower lithography node (100nm feature size/slot width) and longer

strip-to-slot mode adapter length.

9.4 Sources of Insertion Loss

While SOH modulations offer phase modulation without any amplitude chirp, several factors contribute to the insertion loss of these modulators. The insertion loss of the strip-to-slot mode converter can be as low as 0.2 dB [122]. The work in this design has 0.88dB insertion loss due to the coupler, assuming no surface roughness on the slot waveguide. Here we break down the sources contributing to the total insertion loss. Since the slot waveguide mode is a leaky waveguide, it has an intrinsic loss of 0.1dB/mm in the absence of any doping. Adding the surface roughness of the modulator increases the loss of the modulator to 0.5dB/mm. The doped waveguides in the rail and slab region add 0.6dB/mm additional loss to the modulator. Thus, for an ideal structure, the waveguide will have 1.2dB/mm loss. Furthermore, fabrication imperfections in the slot regions, such as incomplete etch of the slot region or contamination can add more loss. Simulations have shown that the presence of nano-scale particles in the slot region in an extreme case adds 5dB/mm loss. However, in reality, waveguide imperfections are rare, and careful handling of the chips in a cleanroom environment can result in negligible imperfections in the waveguide. SEM inspections show that a maximum of two defects for every $400\mu m$-long modulator is expected, resulting in a total propagation loss of 1-2dB/mm. Improving the process and chip handling steps can eliminate this source of loss. Finally, mask misalignment can introduce additional loss. For the low sensitivity strip-to-slot coupler, this translates to 0.2dB additional insertion loss for the worst-case misalignment.

9.5 High-Speed SOH Modulator Design

A traveling-wave SOH modulator with > 50GHz bandwidth is designed as shown in Fig. 9.10. This modulator will have less than 0.6dB loss from the mode adapters and has 1.35dB/mm optical propagation loss in the modulator. The total length of the modulator is $550\mu m$. The strength of the applied electric field in the slot region is $2 \times 10^5 V/m$. RF simulations using HFSS and the extracted Y parameters are used to calculate the effective electrical model of the device. The extracted series resistance and capacitance of the modulator are 10kOhm/mm and 100fF/mm respectively. The cross-section of this traveling-wave modulator is shown in Fig. 9.11. This modulator can operate in a push-pull configuration with a distributed decoupling capacitor between the RF ground and the DC bias node, which helps in

suppressing any ripple along the bias line.

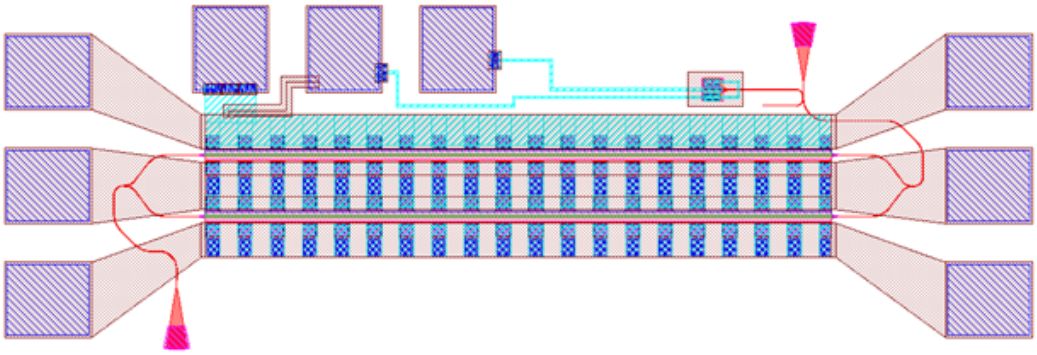

Figure 9.10: Layout of high-speed traveling-wave SOH modulator.

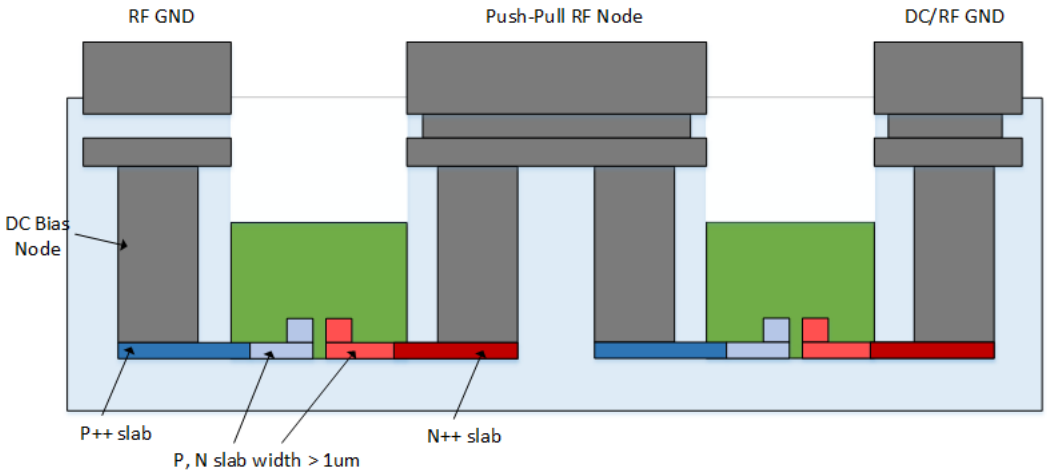

Figure 9.11: Cross-section of high-speed modulator. Oxide layer between the DC bias electrode and RF ground electrode acts as a distributed decoupling capacitor.

9.6 Dual-SSB LIDAR Signal Generator

Using the high-speed complex waveform generation capability of SOH-based modulators, a dual SSB complex waveform generator is implemented. This modulator takes in two electrical signals of $A_1(t)$ and $B_1(t)$, and, through an SSB modulator, produces the complex optical waveform of $E(t) = A_1(t) \times cos(\omega_{opt}t + \phi_{opt} + B_1(t))$, where both phase and amplitude of the optical wave are modulated. Two such SSB modulators can be used for implementing a LIDAR system for simultaneous distance/velocity measurement. Layout of this system is shown in Fig. 9.12. Each modulator arm is designed as a traveling-wave structure with the group-velocity of

optical and electrical fields matched having on-chip 50Ω terminations. A series of low-frequency and high-frequency photodetectors in conjunction with small thermal tuning nodes are incorporated for tuning and calibrating the generated complex waveform. SEM images of the traveling-wave SOH modulator are shown in Fig. 9.13, where the slot cavity and the mode adapter are clearly formed. Die-photo of this design is shown in Fig. 9.14.

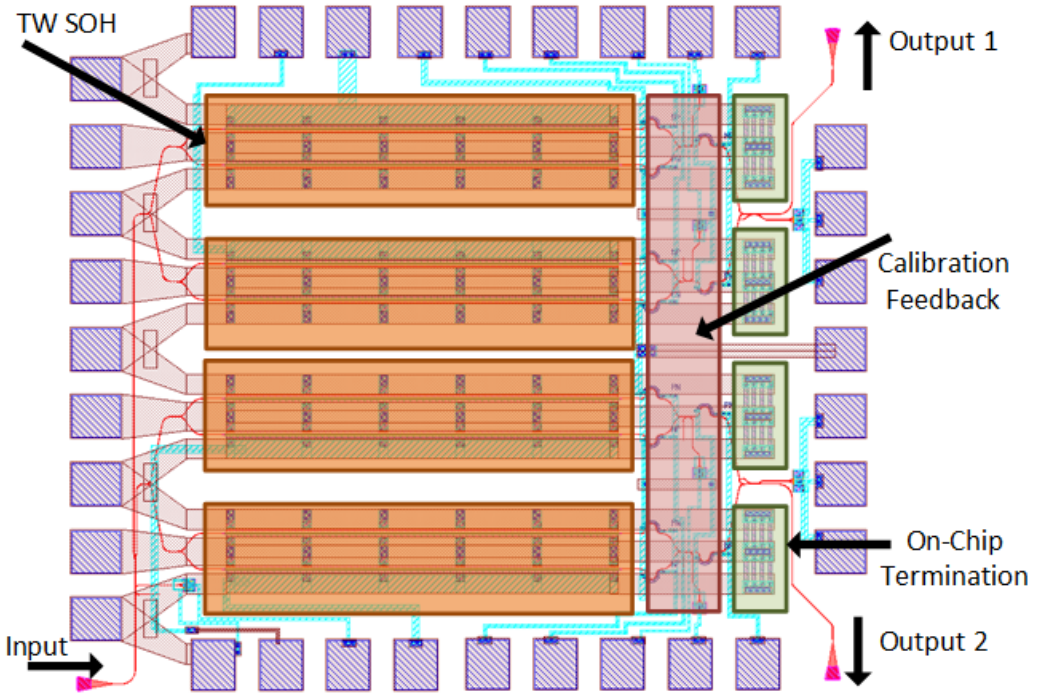

Figure 9.12: Layout of high-speed dual SSB modulator. Integated SSB modulators allow for complex waveform modulation of the optical signal. A series of thermal tuners as well as photodetectors allows for dynamic calibration and modification of the generated complex waveforms.

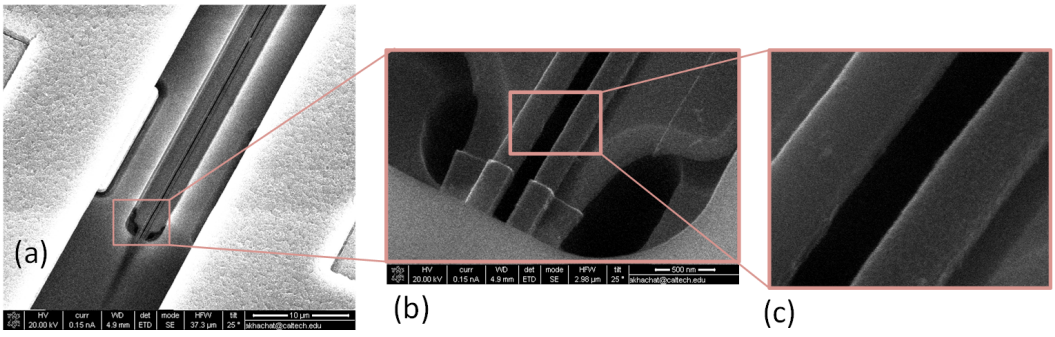

Figure 9.13: SEM images of the traveling-wave slot waveguide modulator.

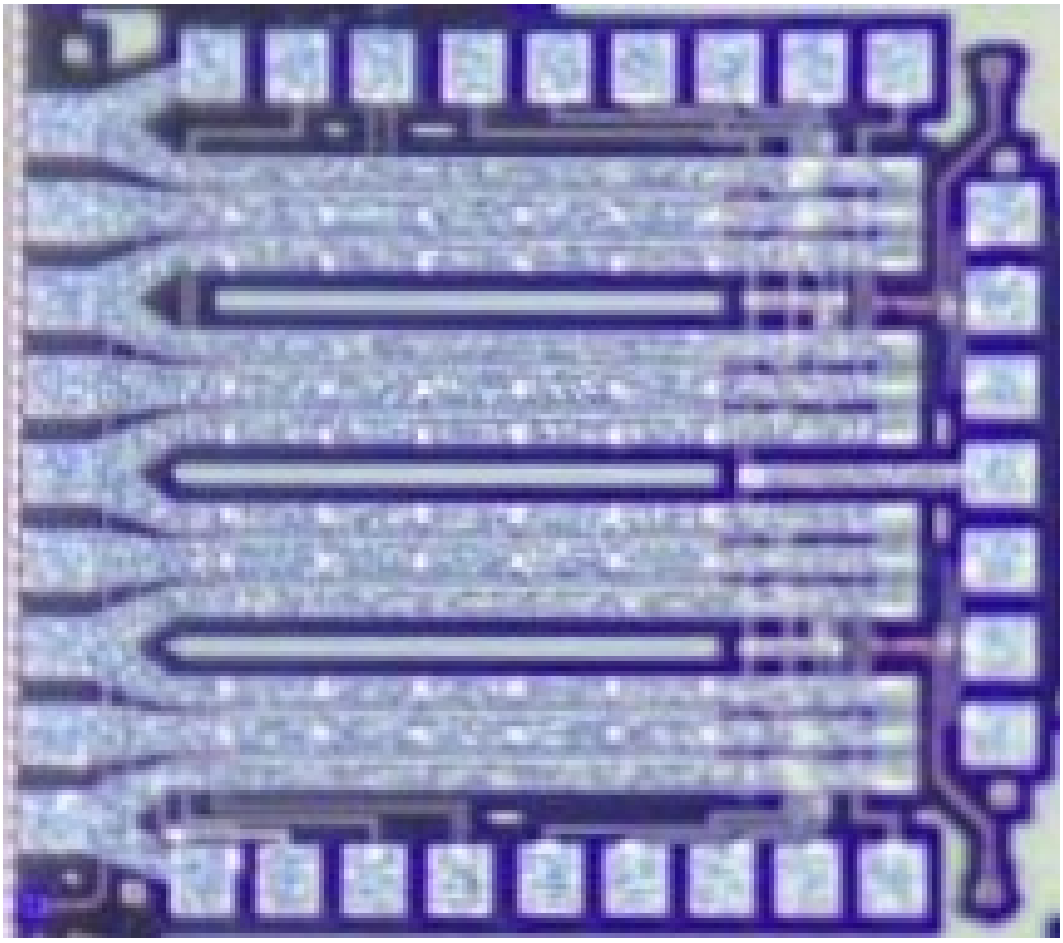

Figure 9.14: Die-photo of dual high-speed dual SSB SOH traveling-wave modulators.

9.7 SOH 1D OPA Design

A compact four-element phased array with SOH phase modulators and integrated phase control feedback system is implemented Fig. 9.15. Integrated phase modulators allow for on-chip calibration of the beam direction without requiring any external calibration mechanism. Furthermore, these capacitive SOH modulators offer sub-dB insertion loss and do not require static power for maintaining the beam direction. Furthermore, these modulators offer very little modulator capacitance, which means they can be steered at GHz frequencies. Expanding on this design, a large-scale 128-element OPA with phase and amplitude control is implemented (Fig. 9.16).

This architecture utilizes row/column addressing for the capacitive modulators to reduce the number of required electrical drivers (Fig. 9.17(a)). It also incorporates interferometric phase detectors as well as sniffer diodes to monitor the relative phase

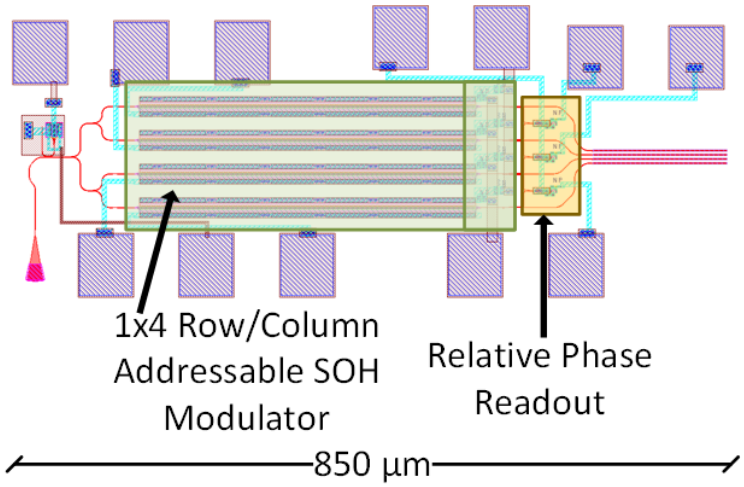

Figure 9.15: Layout of four-element OPA with SOH phase modulators and integrated phase control feedback.

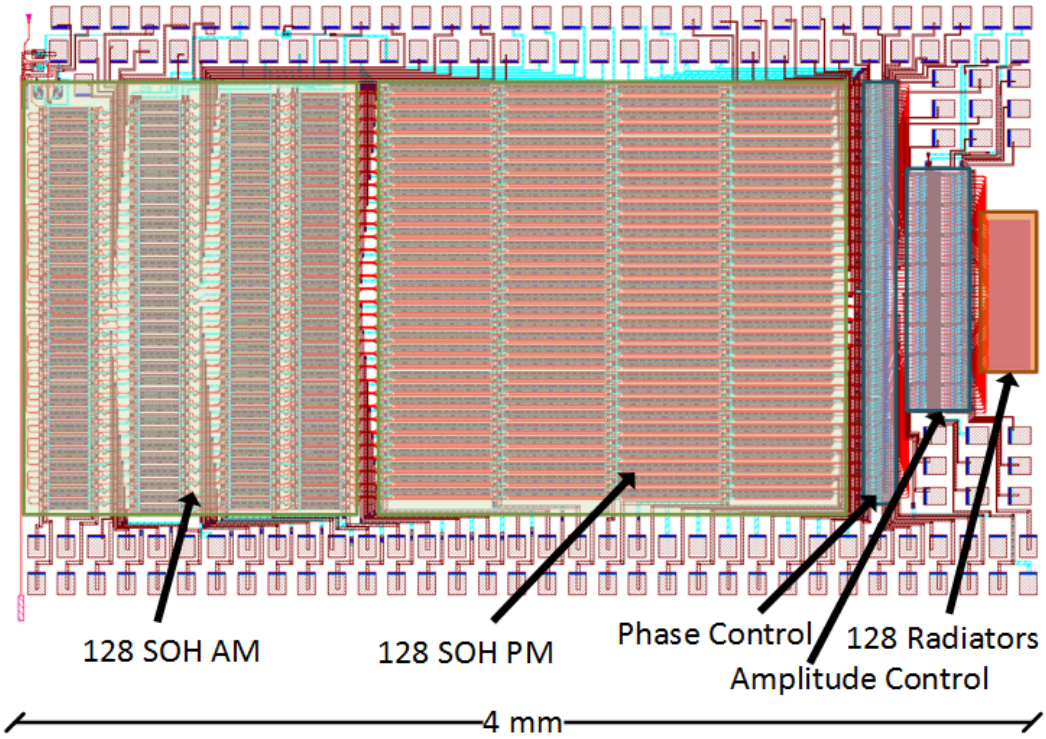

Figure 9.16: 128-element OPA with SOH phase and amplitude modulators and integrated phase and amplitude control.

and amplitude between the radiators as shown in Fig. 9.16. These detectors are read using a row-column readout architecture as shown in Fig 9.17(b)). This structure

employs a total of 256 SOH phase and amplitude modulators, which is the highest density integration for any SOH-employing photonics system. Die photo of the design is shown in Fig. 9.18.

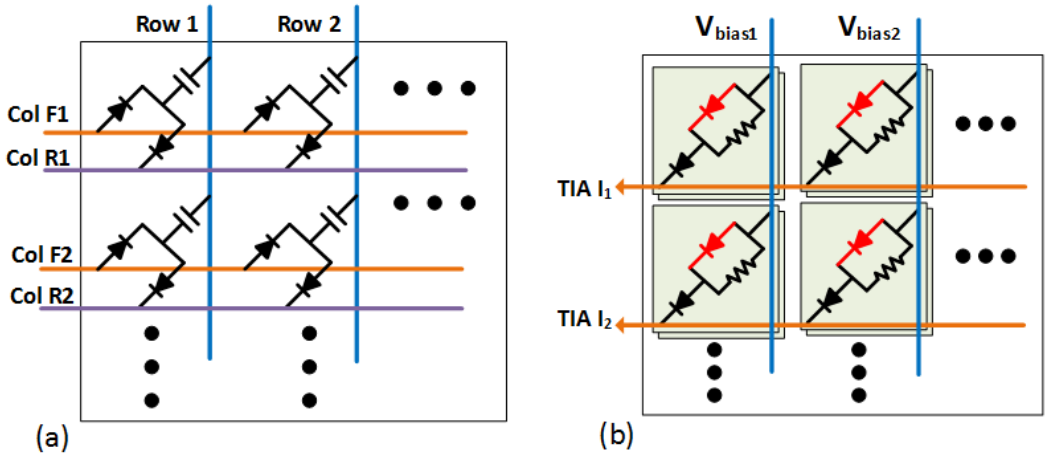

Figure 9.17: 128-element OPA row-column control. (a) Row-column programming of the capacitive modulators. (b) Row-column readout of the phase and amplitude detectors.

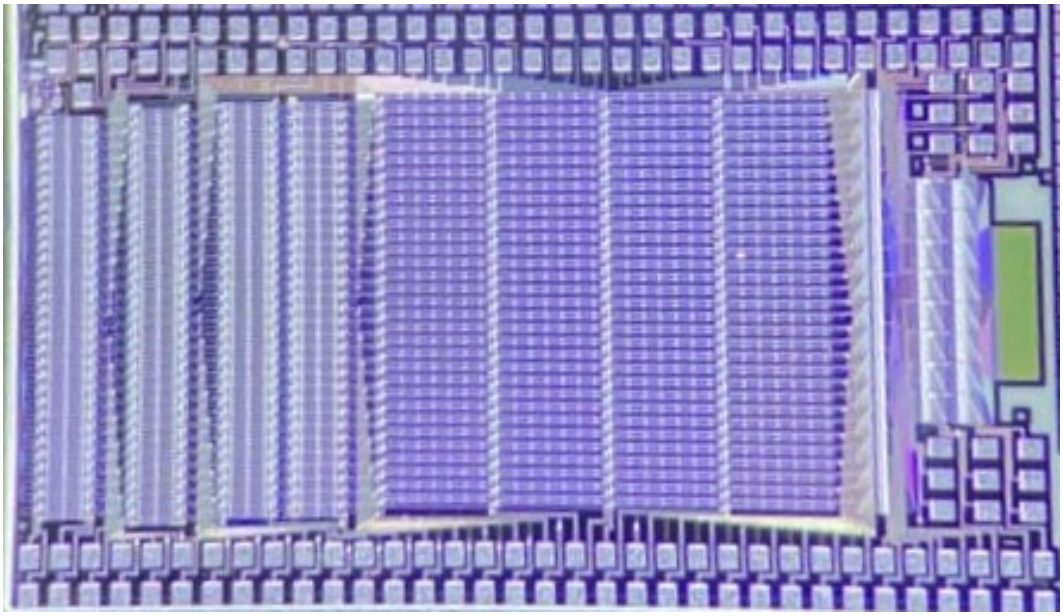

Figure 9.18: Die-photo of the 128-element SOH modulator OPA.

Chapter 10

HIGH-SPEED NESTED-RING-ASSISTED MZI MODULATOR

A multi-ring-assisted MZM is designed and demonstrated here. This modulator uses maximally-flat multi-ring filter structures to act as a phase modulator with a linear response and reduces voltage requirements. The larger the number of rings, the sharper the phase response, and the smaller the required drive voltage. The resulting MZI modulator can be used as a compact amplitude modulator. Furthermore, this modulator can operate with a low quality-factor. This reduces the system's sensitivity to environmental variations compared to standalone ring resonator modulator (RRM) or ring-assisted MZI (RAMZI)[1].

10.1 Introduction

Integrated photonics modulators are the critical components for creating complex, high-density, and high-speed electro-optic systems. In designing a system incorporating a complex network of photonic modulators, two choices need to be made: modulator type and modulator architecture. Different modulator types and their performance were explored in the previous chapter. Standard silicon photonic modulators such as PN, PIN, or SOS modulators rely on the plasma-dispersion effect with inherently coupled phase and amplitude modulation through the Kramers-Kronig relations [123]. Hybrid platforms such as silicon-organic-hybrids operating based on $\chi^{(2)}$ Pockel's effect show great promise for improving modulator size and bandwidth [39], [106]. Regardless of the modulator's choice, which affects the system's overall phase and amplitude response, the architecture's choice also plays a role. It impacts the size, operation bandwidth, and sensitivity of the system to environmental variables and process variations.

For instance, Mach-Zhander Modulators (MZMs) have a large bandwidth and are less susceptible to environmental variations. However, they are large and require a large drive voltage for operation. Resonance-based modulators such as ring and disk resonators have a much smaller footprint and require a lower driver voltage but have a quality factor-bandwidth trade-off, limiting the modulation efficiency for a given modulation bandwidth. In addition, they require resonance stabilization against environmental variations. Previously, architectures that break quality-factor-

[1]This work was done in collaboration with Parham Porsandeh Khial.

bandwidth trade-off have been demonstrated [124], [125], but they still require resonance stabilization. On the other hand, complex modulation formats such as PAM4 or QAM4 can increase the data-rate even further. However, to maintain acceptable SNR and EVM for data transmission applications, these complex modulations rely on increasingly complex data equalization techniques such as pre-emphasis and pre-distortion [126]. Henceforth, it is crucial to create a high-bandwidth, high-linearity modulator. Previously, ring-assisted MZI modulators as a hybrid architecture of resonance and MZI structures have been used to improve the linearity of the modulators [127]–[130]. These modulators improve the linearity but still suffer from all the problems in resonance-based systems, such as temperature sensitivity and drive-voltage requirements.

An improvement on this ring-assisted architecture can be made using several ring resonators placed on the modulator in a cascaded form [131]–[133]. These architectures achieve high modulation efficiency at the expense of increased insertion loss and reduced modulation bandwidth. In this work, instead of cascading RRMs in an MZI, complex higher-order ring-resonator filters [134], [135] are used as phase modulators in an assisted MZI architecture. This novel architecture, named nested-ring-assisted MZM (NRAMZM) uses ring filters with a flat pass-band region while maintaining a linear phase response in the operation region. The slope of the phase response for this phase modulator increases linearly with the filter order (number of rings in the chain). As a consequence, these types of modulators offer improved modulation efficiency. Furthermore, the MRAMZM has a wide pass-band region in frequency and maintains a low quality-factor even for higher-order (five nested rings). Hence, it is less susceptible to environmental variations.

A nested-ring-assisted MZM using a three-stage maximally flat filter response is implemented in a standard silicon photonics process based on three-stage flat ring parameters in [135]. Section II will analyze the theory of the operation for modulation architectures mentioned above. The response of single-ring amplitude modulators, ring-assisted MZIs, cascaded ring-assisted MZIs, and the presented nested ring-assisted MZIs is examined. Section III will discuss the implemented design in the silicon photonics process.

10.2 Background and Theory

A standard intensity modulator MZI is modulated (Fig. 10.1(a)) by an input voltage $V_1(t)$ where the modulation coefficient is denoted by a_1. The modulator is driven

in a push-pull fashion with only a single electrical driver and reduces drive voltage requirements (10.1).

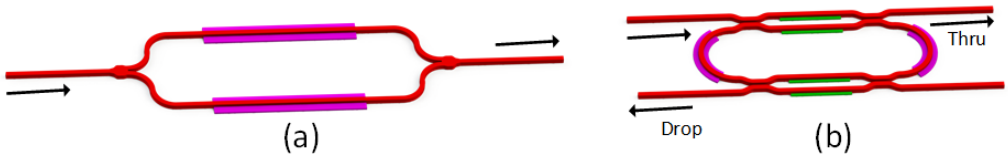

Figure 10.1: Basic ring resonator and interferometric modulators.

$$E_{out}(t) = 1/\sqrt{2}[cos(\omega_o t + \phi_o + a_1 V_1(t)) + cos(\omega_o t + \phi_o - a_1 V_1(t))] \quad (10.1)$$

In an ideal scenario, the differential phase induced in each arm is achieved using linear phase modulators without any additional induced loss. The resulting output signal can be simplified to

$$E_{out}(t) = 2/\sqrt{2}cos(a_1 V_1(t))cos(\omega_o t + \phi_o) \quad (10.2)$$

For a sinusoidal voltage modulation, the modulator's output has many high-order harmonic terms (10.3).

$$V_1(t) = cos(\omega_{RF} t + \phi_{RF})cos(a_1 V_1(t))cos(\omega_{opt} t + \phi_{opt}) \quad (10.3)$$

In a first-order simplification using the Jacobi-Anger expansion, the output signal can be approximated by (10.4).

$$E_{out}(t) = 2/\sqrt{2}b_1 cos(\omega_{RF} t)cos(\omega_o t + \phi_o) \quad (10.4)$$

As mentioned earlier, implementing this architecture in an integrated platform using standard waveguide phase modulators will have a large footprint. Alternatively, it is possible to use a more complex structure such as a ring resonator to achieve the desired phase shift in each arm. Here, it is assumed that the ring's dynamic settling time is much shorter than the modulation frequency of the structure. Henceforth, only the steady-state response of the ring modulator structure is analyzed in the frequency domain. A time-domain analysis can be performed based on [125], [132]. The steady-state ring resonator modulator response at the output of the two ports is given by (10.5) and (10.6), where α and ϕ are the round-trip loss and phase accumulation; κ_1, σ_1 are the coupling and transmission coefficients near the

through-port coupler; and κ_2 and σ_2 are the coupling and transmission coefficients for the drop-port coupler in the ring structure (Fig. 10.1(b)) [136].

$$E_{Thru}(\phi) = \frac{\sigma_1 - \sigma_2^* \alpha e^{j\phi}}{1 - \sigma_1^* \sigma_2^* \alpha e^{j\phi}} \tag{10.5}$$

$$E_{Drop}(\phi) = \frac{-\kappa_1^* \kappa_2 \alpha^{1/2} e^{j\phi/2}}{1 - \sigma_1^* \sigma_2^* \alpha e^{j\phi}} \tag{10.6}$$

Here, the intensity and phase response of the ring drop-port and changes in intensity and phase response with respect to the wavelength is plotted for various drop-port coupling coefficients (Fig. 10.2) under critical coupling conditions ($\alpha = \sigma_1/\sigma_2$). The transmission coefficient is denoted by σ and can be computed from the coupling coefficient using $\sigma^2 + \kappa^2 = 1$ relation for a loss-less coupler.

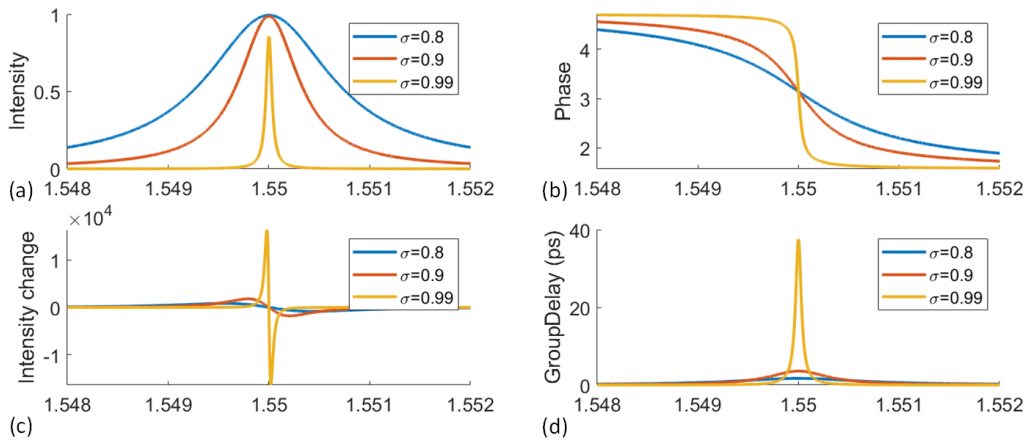

Figure 10.2: Drop port of single ring-resonator for different σ values.

As σ_2 approaches unity for a critically coupled structure, the ring's quality factor increases, and the maximum coupled power decreases while the slope of the phase response improves. These trends are shown in Fig. 10.3.

For comprehensive treatment of ring resonators, time-domain ring loss modulation effect on bandwidth and modulation depth $\Delta = (I_{max} - I_{min})(I_{max} + I_{min})$ are examined using (10.7) from [125] where τ is the ring round-trip time.

$$T_{Thru}(t) = \sigma + a(t)e^{-i\phi}(sigmaT(t - \tau) - 1) \tag{10.7}$$

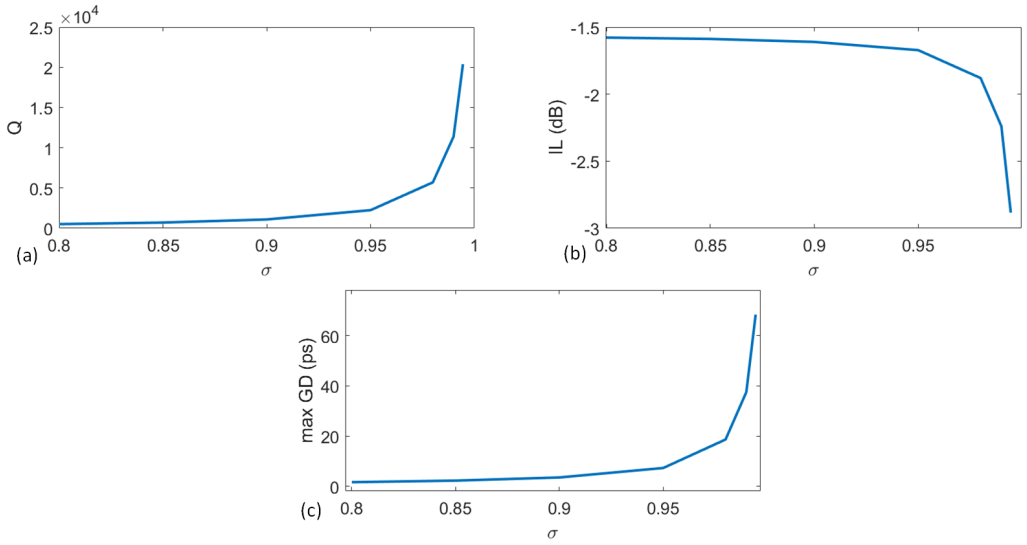

Figure 10.3: Performance of RRM for various σ values. Quality factor (a), insertion loss (b), and group delay (c) increase with increased transmission at the drop port.

Bandwidth and modulation depth for ring round-trip loss modulation for various quality-factors is shown in Fig. 10.4. For low drive voltage operation using a high quality-factor, the modulation bandwidth and modulation depth will be limited, as shown in [124].

Standalone single-ring resonator as an amplitude modulator is design by first specifying the desired output extinction ratio (ER). Intensity and phase of a ring resonator for 4dB extinction ratio is shown in Fig. 10.5 (a),(b) plotted as a function of the fraction of wavelength phase increase to the total resonator round-trip in radians ($d\phi_R = 2\pi(R_{Vmod} - R_{V=0})/\lambda \times 2\pi$). Applying sinusoidal voltage modulation to this ring (Fig. 10.5(c)) results in the output waveform shown in Fig. 10.5(e).

Ring-Assisted MZI Modulator

As expected, the output phase of the ring resonator is linear near the resonance (Fig. 10.5(b)) and serves as the compact and linear phase modulator for ring-assisted MZI structures. This structure is depicted in Fig. 10.6. Similar to push-pull MZI modulators, this structure can also be operated by shifting the two-ring's resonance wavelengths in opposite directions. This architecture requires large voltage swings to shift the ring resonance frequencies by $\pi/2$. Furthermore, the rings are required to have a high quality-factor. Henceforth, the structure is very susceptible to temperature variations.

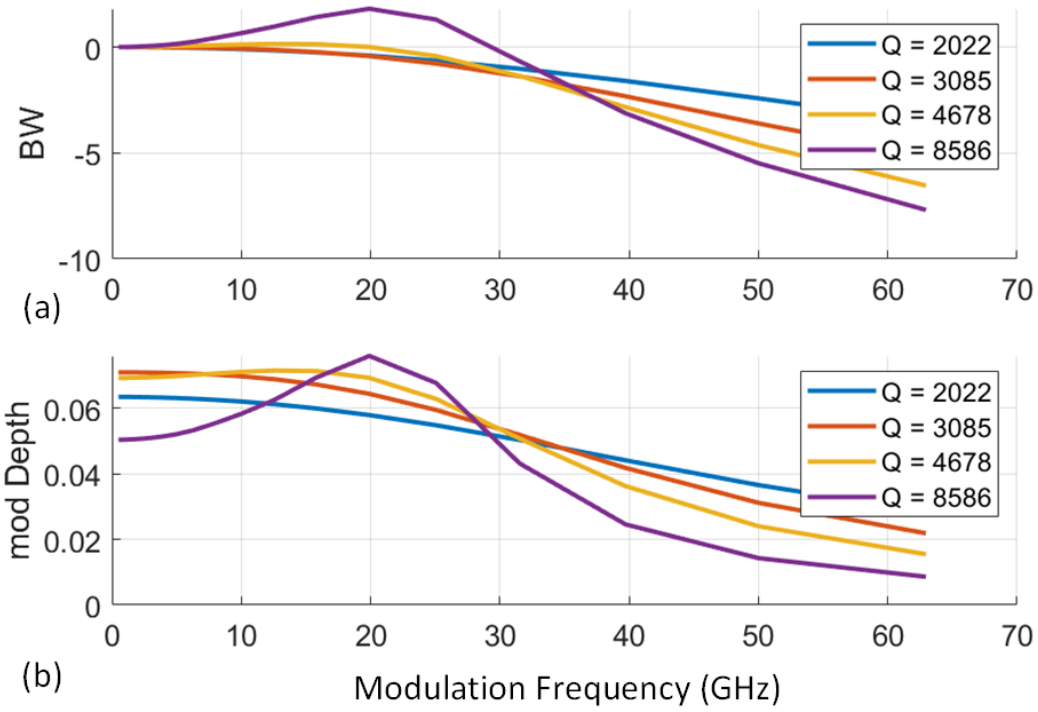

Figure 10.4: Small signal modulation depth and bandwidth for single-ring resonator loss modulators for different quality factor values.

Calculating the required change in ring round-trip length to achieve $\pi/2$ phase shift, we can compute the ring phase and amplitude change as shown in Fig. 10.7 (a),(b). Using this ring resonator with a sinusoidal drive voltage that provides $\pi/2$ phase shift in two arms of a differentially-modulated RAMZI, we observe high extinction-ratio as well as reduced insertion loss (Fig. 10.7 (e)).

Cascaded Ring-Assisted MZI Modulator

It is shown that a cascade of ring resonator modulators on the MZI modulator arms can further improve the modulation efficiency of this structure by reducing the drive voltage requirements [132]. Fig. 10.8 shows a differentially driven cascaded-ring resonator modulator with three cascaded rings in each arm. This modulator's transfer function is similar to the through-port of the ring where N is the number of rings in the cascaded chain (10.8).

$$E_{Cascade}(\phi) = \left(\frac{\sigma_1 - \sigma_2^* \alpha e^{j\phi}}{1 - \sigma_1^* \sigma_2^* \alpha e^{j\phi}}\right)^N \tag{10.8}$$

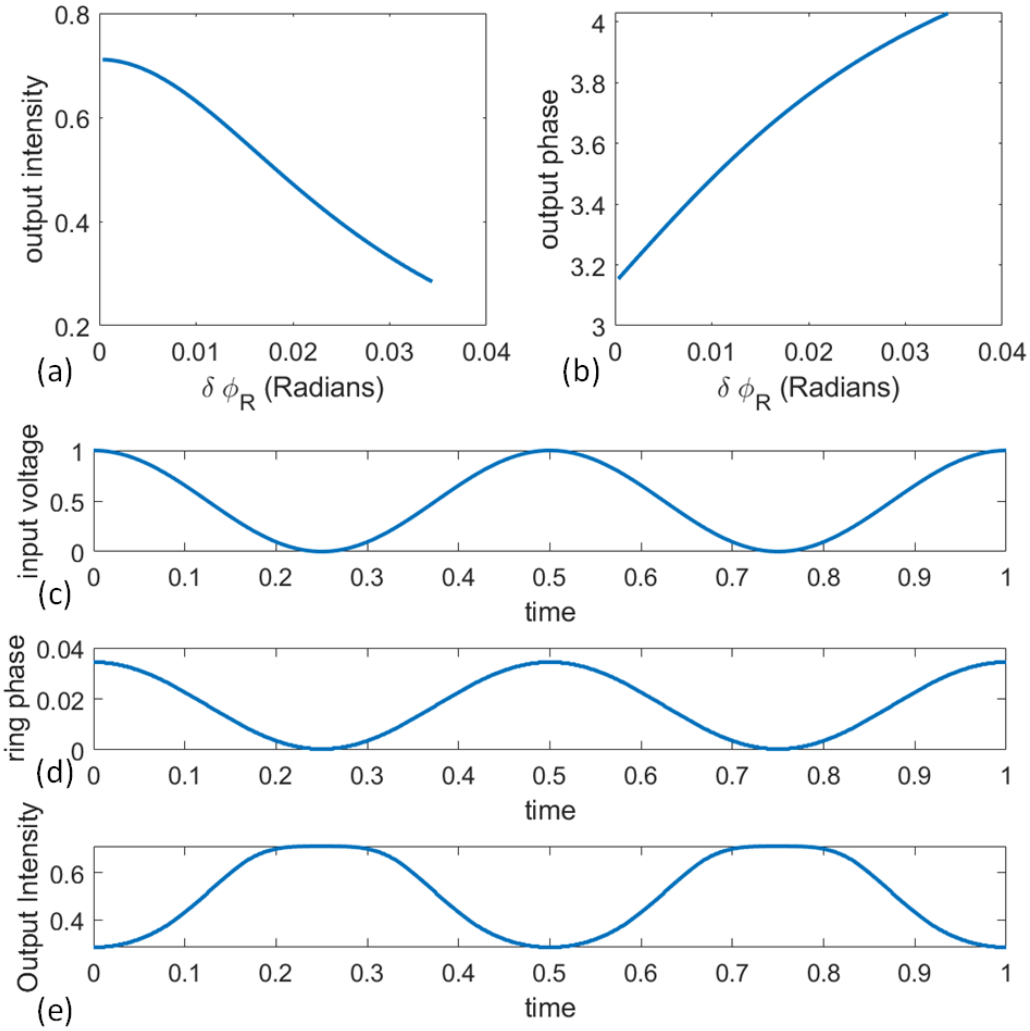

Figure 10.5: RRM output intensity and phase variations for 4dB ER intensity modulation. (a) Amplitude and (b) phase response of ring as a function of the fraction of wavelength phase increase to the total resonator round-trip in radians. (c) Sinusoidal input voltage. (d) Ring phase modulation. (e) Modulated output intensity.

Similar to the single-ring resonator, the intensity and phase response of the cascaded-ring resonator is calculated for a transmission coefficient of $\sigma = 0.9$ for several cascaded ring resonators with $10\mu m$ ring radius and 1 dB propagation loss. This is shown in Fig. 10.9. As it is seen in Fig. 10.9(b), the slope of the phase response increases with the increasing number of rings, which reduce the drive voltage requirements. Quality-factor, insertion loss, maximum group delay, and change in ring round-trip path, as a fraction of the operation wavelength, required

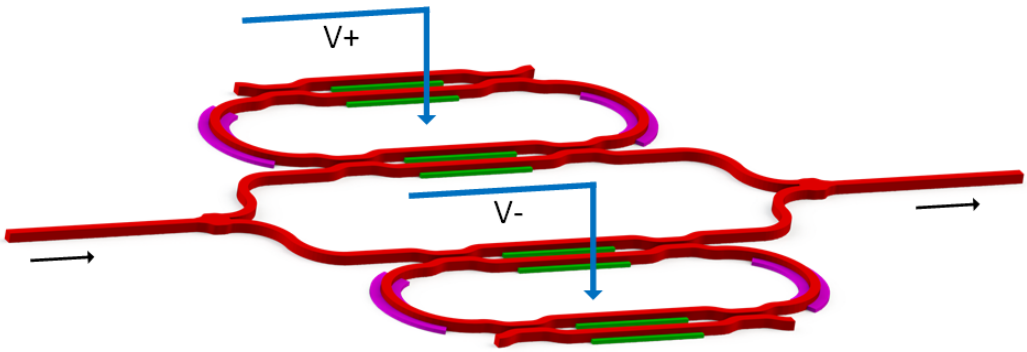

Figure 10.6: Dual ring assisted MZI modulator.

for $\pi/2$ phase shift are plotted for increasing number of rings in the cascaded ring resonator modulator (Fig. 10.10).

Ring phase shift required to achieve $\pi/2$ phase shift is calculated, and the resulting multi-ring cascaded structure's intensity and amplitude response is shown in Fig. 10.11 (a),(b) for $N = 3$ and $N = 5$ rings. A higher number of rings significantly reduces the ring modulation requirements at an increased insertion loss. Finally, the modulation performance of this structure for a sinusoidal input is analyzed for both cases in Fig. 10.11 (c),(d),(e). The drive voltage requirements are three to five times smaller than single ring-resonator.

Nested Ring-Assisted MZI Modulator

For nested ring-assisted MZI modulators, the coupling parameters are optimized for maximally flat ring resonator response. This nested-ring modulator is referred to as aperiodic coupled ring-resonator waveguide in [135]. Coupling coefficient for maximally flat 3-ring modulator and 5-ring modulators are (0.4668, 0.099, 0.099, 0.4668) and (0.4306, 0.0782, 0.0544, 0.0544, 0.0782, 0.4306) respectively [135]. This structure is shown in Fig. 10.12 for differential operation. It can be seen that the coupling coefficients are symmetric with respect to the center of the structure.

The analytical formulation for the through and drop port of nested rings using the algebraic approach shown in [136] is complex and cannot be intuitively analyzed. A more intuitive approach using matrix analysis of forward and back-propagating waves in the rings is shown in [137]. A simplified derivation of the wave propagation analysis based on [137] is shown here. Forward and backward propagation waves in the ring resonator are shown in Fig. 10.13.

Forward propagating waves $[A_1', C_1']$ entering the junction related to the output

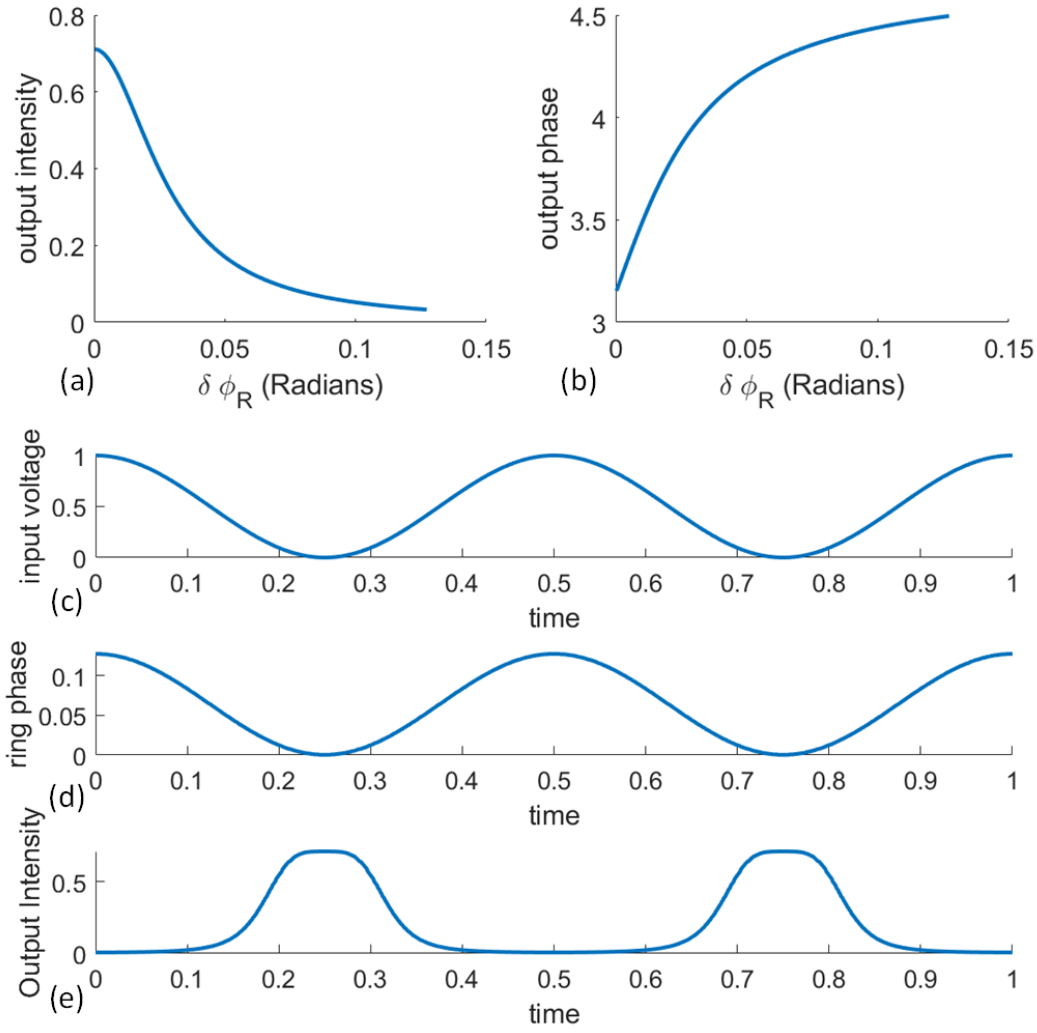

Figure 10.7: Ring assisted MZI. (a) Amplitude and (b) phase response of each arm as a function of the fraction of wavelength phase increase to the total resonator round-trip in radians. (c) Sinusoidal input voltage. (d) Ring phase modulation. (e) Modulated intensity at the output of the RAMZI.

waves $[D_1, B_1]$ via matrix (10.9)

$$\begin{bmatrix} B_1 \\ D_1' \end{bmatrix} = \begin{bmatrix} \sigma_1 & \kappa_1 \\ -\kappa_1^* & \sigma_1^* \end{bmatrix} \begin{bmatrix} A_1' \\ C_1' \end{bmatrix} \tag{10.9}$$

Backward propagating waves for the same coupler $[A_1, C_1]$ leaving the coupler as a result of the input waves $[B_1', D_1']$ via the matrix give (10.9)

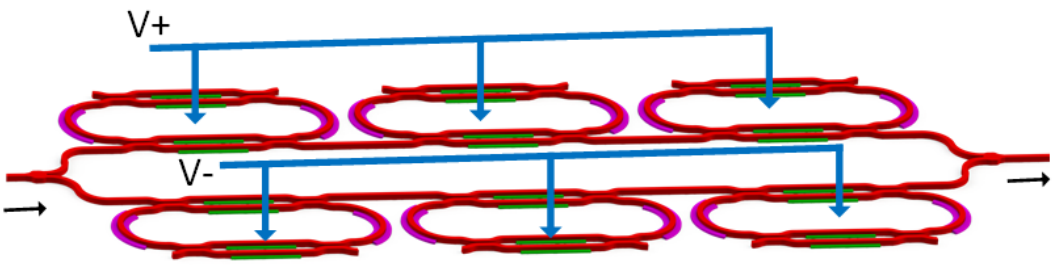

Figure 10.8: Differentially modulated cascaded-ring assisted MZI modulator.

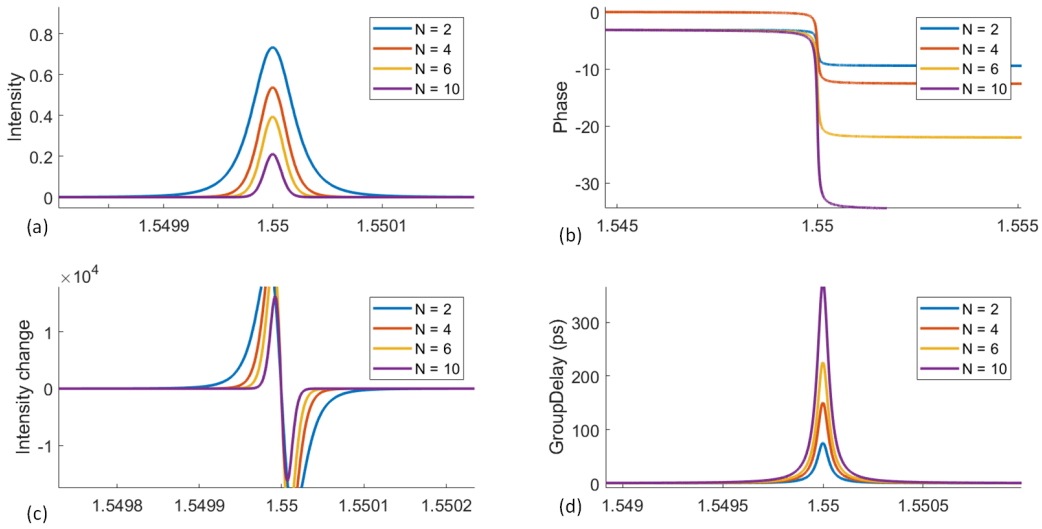

Figure 10.9: Cascaded ring resonators' phase and intensity response as a function of the number of rings. Increasing the number of rings beyond $N = 5$ results in more than 3 dB insertion loss.

$$\begin{bmatrix} A_1 \\ C_1 \end{bmatrix} = \begin{bmatrix} \sigma_1 & \kappa_1 \\ -\kappa_1^* & \sigma_1^* \end{bmatrix} \begin{bmatrix} B_1' \\ D_1' \end{bmatrix} \tag{10.10}$$

The resulting four components into and out of each coupler can be formulated as a vector x_n and x_n' in a 4×1 matrix.

$$x_n = \begin{bmatrix} A_n' \\ B_n \\ B_n' \\ A_n \end{bmatrix} \tag{10.11}$$

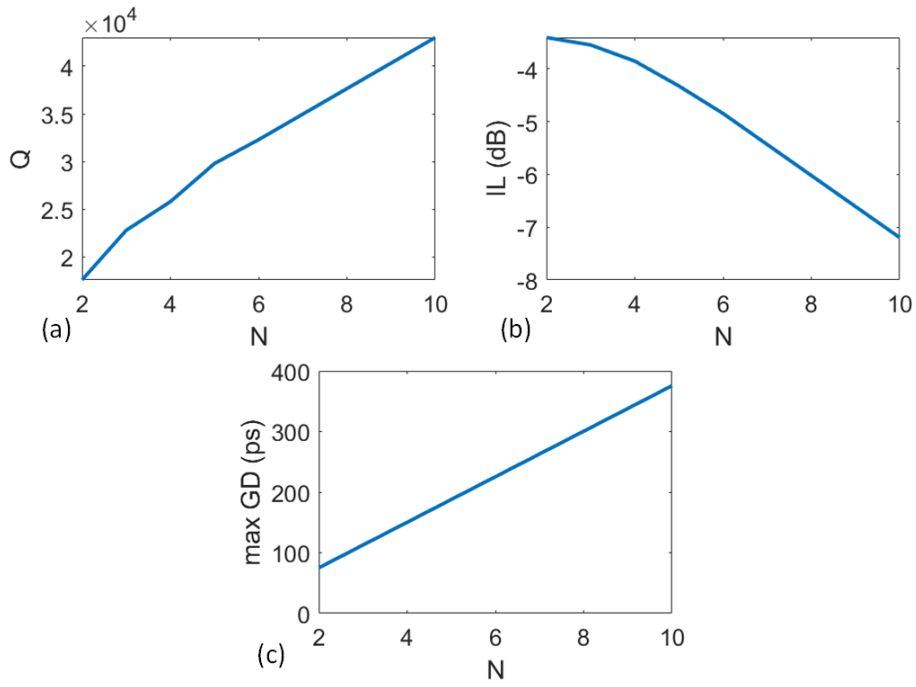

Figure 10.10: Performance metrics for cascaded ring-assisted MZI for various number of rings. (a) Quality factor, (b) insertion loss, and (c) maximum group delay increase for higher number of rings in the structure.

$$x'_n = \begin{bmatrix} C'_n \\ D_n \\ D'_n \\ C_n \end{bmatrix} \tag{10.12}$$

Assuming no back-reflection from these forward and backward propagating waves, we can combine (10.9) and (10.10) as matrix $\mathbb{P}$

$$x_{n+1} = \begin{bmatrix} P & 0 \\ 0 & P \end{bmatrix} x'_n = \mathbb{P} x'_n, \tag{10.13}$$

where matrix P is 2×2.

$$P = \frac{1}{\kappa} \begin{bmatrix} -\sigma & 1 \\ -1 & \sigma^* \end{bmatrix} \tag{10.14}$$

Furthermore, the phase shift resulted from the wave propagating in the ring is given by

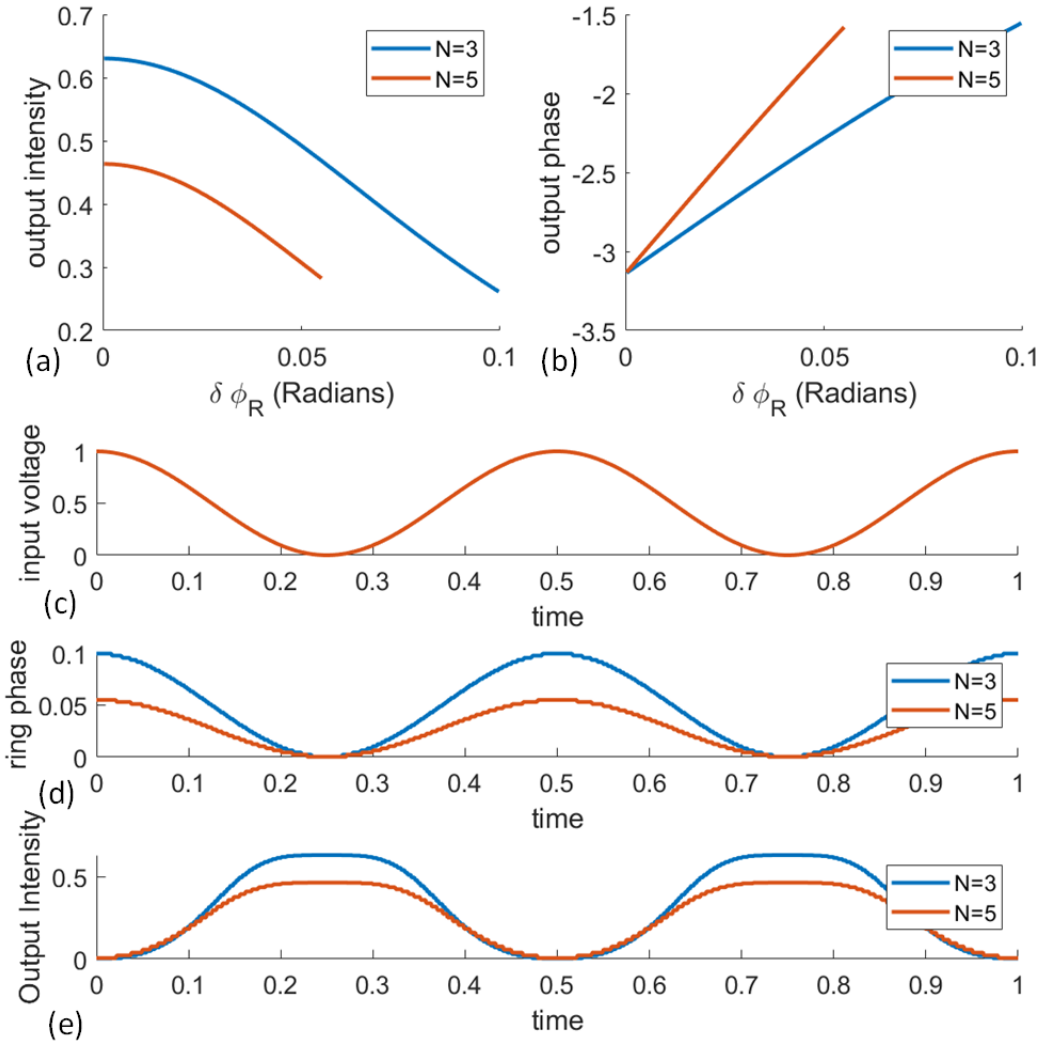

Figure 10.11: Cascaded ring-assisted MZI modulator: (a) Amplitude and (b) phase response of cascaded ring for N=3 and N=5 in each arm as a function of fraction of wavelength phase increase to the total resonator round-trip in radians. (c) Sinusoidal input voltage. (d) Ring phase modulation. (e) Output intensity variations.

$$x_n' = \begin{bmatrix} 0 & Q \\ Q & 0 \end{bmatrix} x_n = \mathbb{Q} x_n \tag{10.15}$$

$$Q = \begin{bmatrix} 0 & e^{-i\beta R\pi} \\ e^{i\beta R\pi} & 0 \end{bmatrix} \tag{10.16}$$

Serially coupling these two terms results in

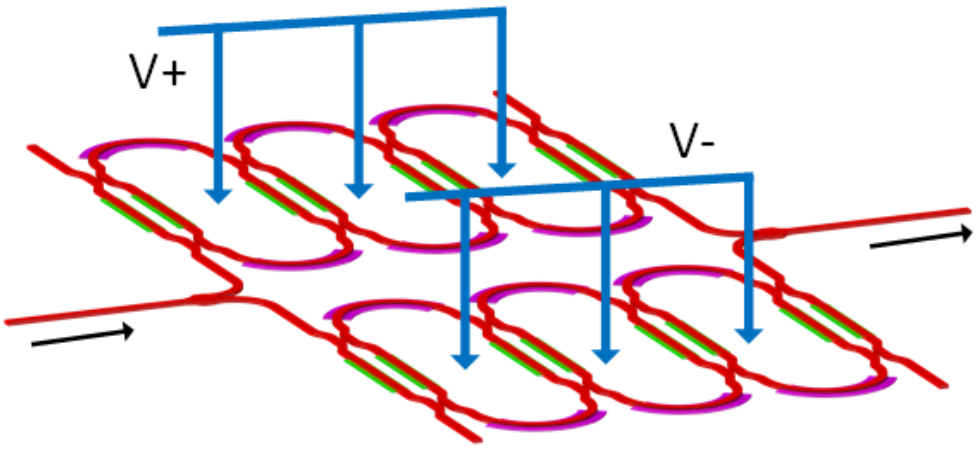

Figure 10.12: Nested ring-assisted MZI modulator.

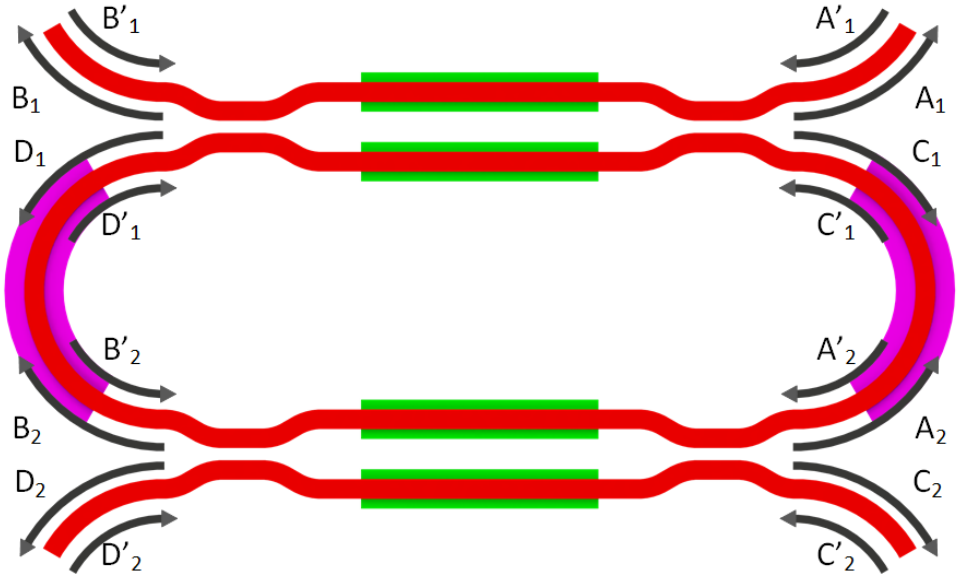

Figure 10.13: Port definition for ring resonator modulator.

$$x_{n+1} = \mathbb{P}\mathbb{Q}x_n \tag{10.17}$$

For the purpose of this analysis, we assume waves propagate in only one direction in the ring (input from port B'_1 and D'_N). Moreover, the input wave leaves the structure through C_N. This results in further simplification for the wave propagation in the structure given by

$$\begin{bmatrix} D'_{n+1} \\ C_{n+1} \end{bmatrix} = PQ \begin{bmatrix} C'_n \\ D'_n \end{bmatrix} \tag{10.18}$$

For the full resonator structure (Fig. 10.14), we can simplify the result into a simple ABCD matrix

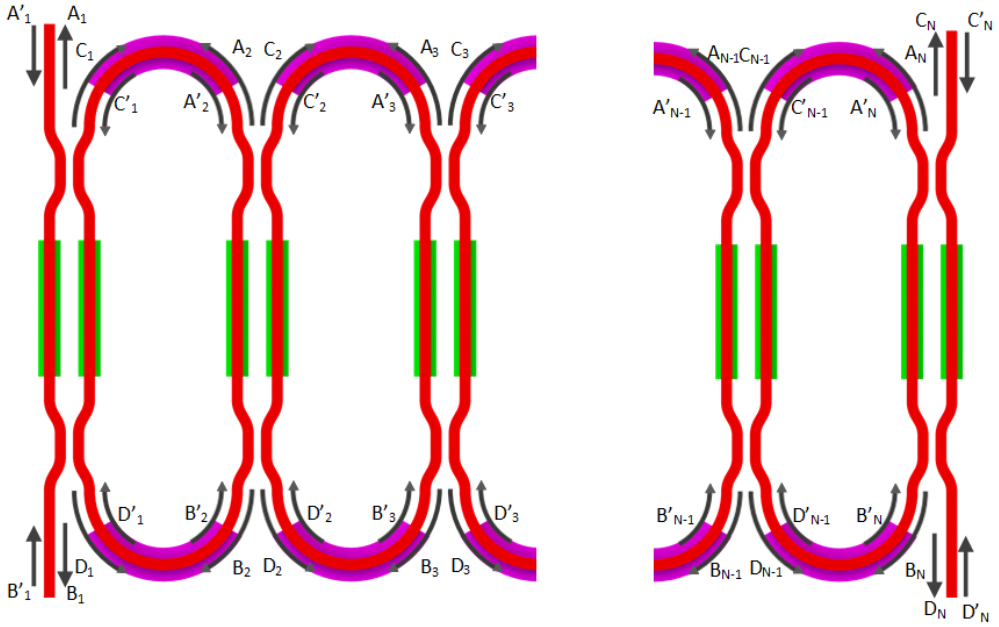

Figure 10.14: Port definition for ring resonator modulator.

$$\begin{bmatrix} D'_N \\ C_N \end{bmatrix} = P_N Q_N P_{N-1} Q_{N-1} \ldots P_1 \begin{bmatrix} C'_1 \\ D'_1 \end{bmatrix} = \begin{bmatrix} \boldsymbol{A} & \boldsymbol{B} \\ \boldsymbol{C} & \boldsymbol{D} \end{bmatrix} = \begin{bmatrix} C'_1 \\ D'_1 \end{bmatrix} \tag{10.19}$$

For modulation applications, light is fed from a single port ($D'_N = 0$). We can now write the simplified transfer function relation for this nested-ring modulator. For the through-port, we have

$$\frac{A_1}{B'_1} = -\frac{\boldsymbol{A}}{\boldsymbol{B}} = T_{thru}(\lambda) \tag{10.20}$$

For the drop port we can write

$$\frac{C_N}{B'_1} = \boldsymbol{C} - \frac{\boldsymbol{AD}}{\boldsymbol{B}} = T_{drop}(\lambda) \tag{10.21}$$

Spectral characteristics for this nested-ring modulator is shown in Fig. 10.15 based on coupling coefficients in [135]. The modulator maintains a wide spectral bandwidth even for a large number of rings. However, the phase slope of the modulator increases linearly. Quality-factor, insertion loss, and maximum group delay for an increasing number of rings is shown in Fig. 10.16.

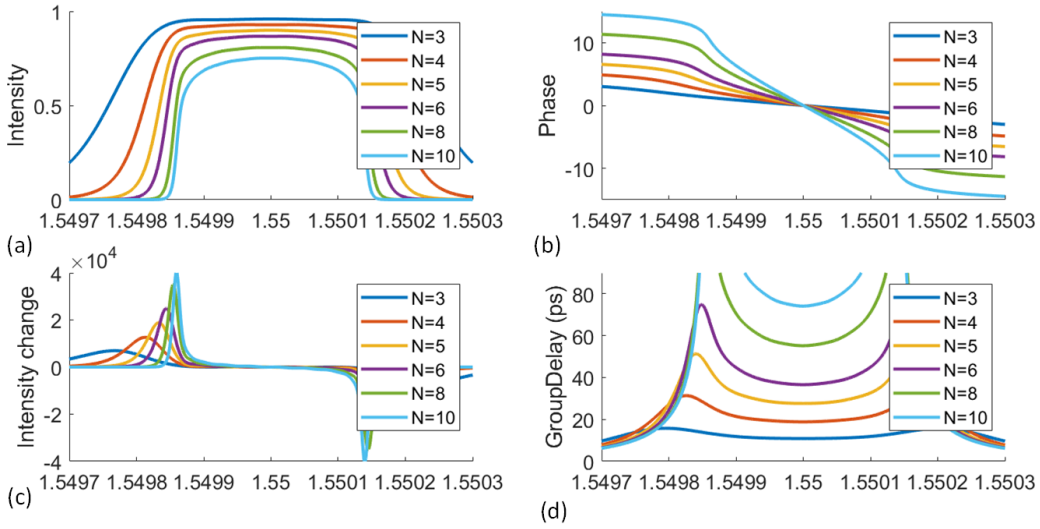

Figure 10.15: Nested-ring resonators' intensity and phase spectral response for different number of rings for maximally flat response.

To compare the performance of this nested ring-assisted MZI modulator with single-ring and cascaded-ring MZI modulators, the required phase shift in the ring resonance (changing the effective length of the resonator) for $\pi/2$ phase change is calculated. The resulting phase and intensity response of the output are plotted in Fig. 10.17 (a) and (b) for three and five nested rings. Compared to the cascaded-ring structure, this nested-ring structure experiences much lower amplitude fluctuations for the same total induced phase shift. The modulated time-domain output intensity of the differential nested-ring-assisted MZI modulator is shown in Fig. 10.17 (e), showing a high extinction-ratio.

10.3 Integrated NRAMZM Design

Based on the design parameters of three nested-ring modulators, a differential nested-ring-assisted modulator is designed in a standard CMOS compatible silicon photonics process. Tunable couplers are implemented to fine-tune the modulator coupling coefficients for flat ring response. Sniffer photodiodes are included to calibrate the resonance wavelength to the desired operation point using integrated

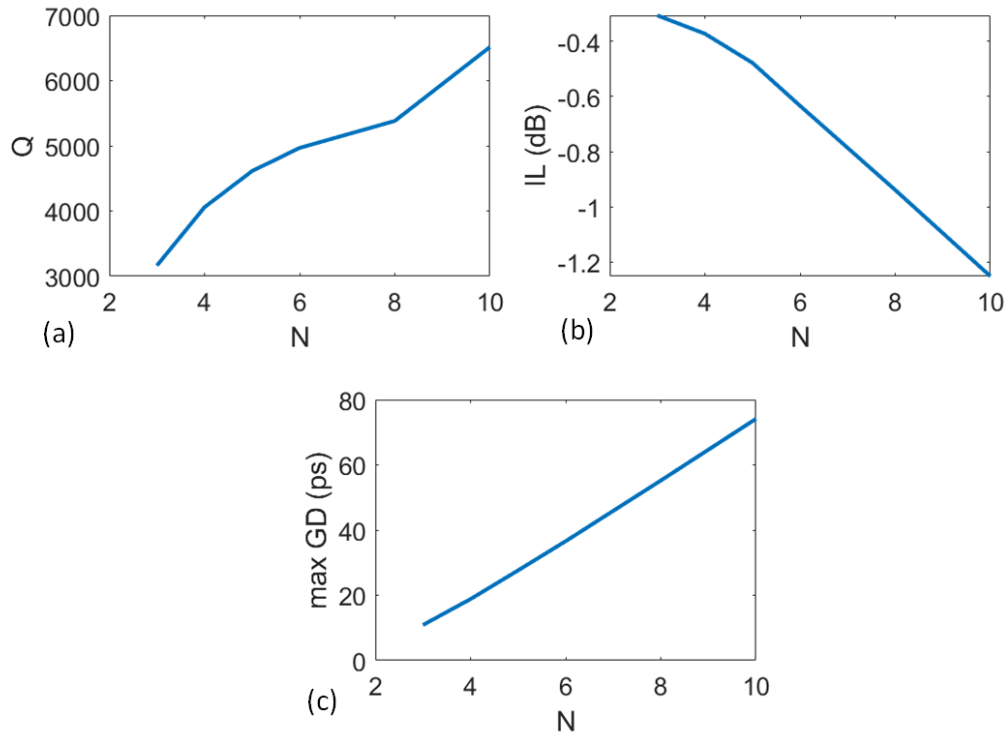

Figure 10.16: Performance metrics for nested ring-assisted MZI for different number of rings for maximally flat response.

thermal heaters in each ring. Die-photo of the proposed design is shown in Fig. 10.18

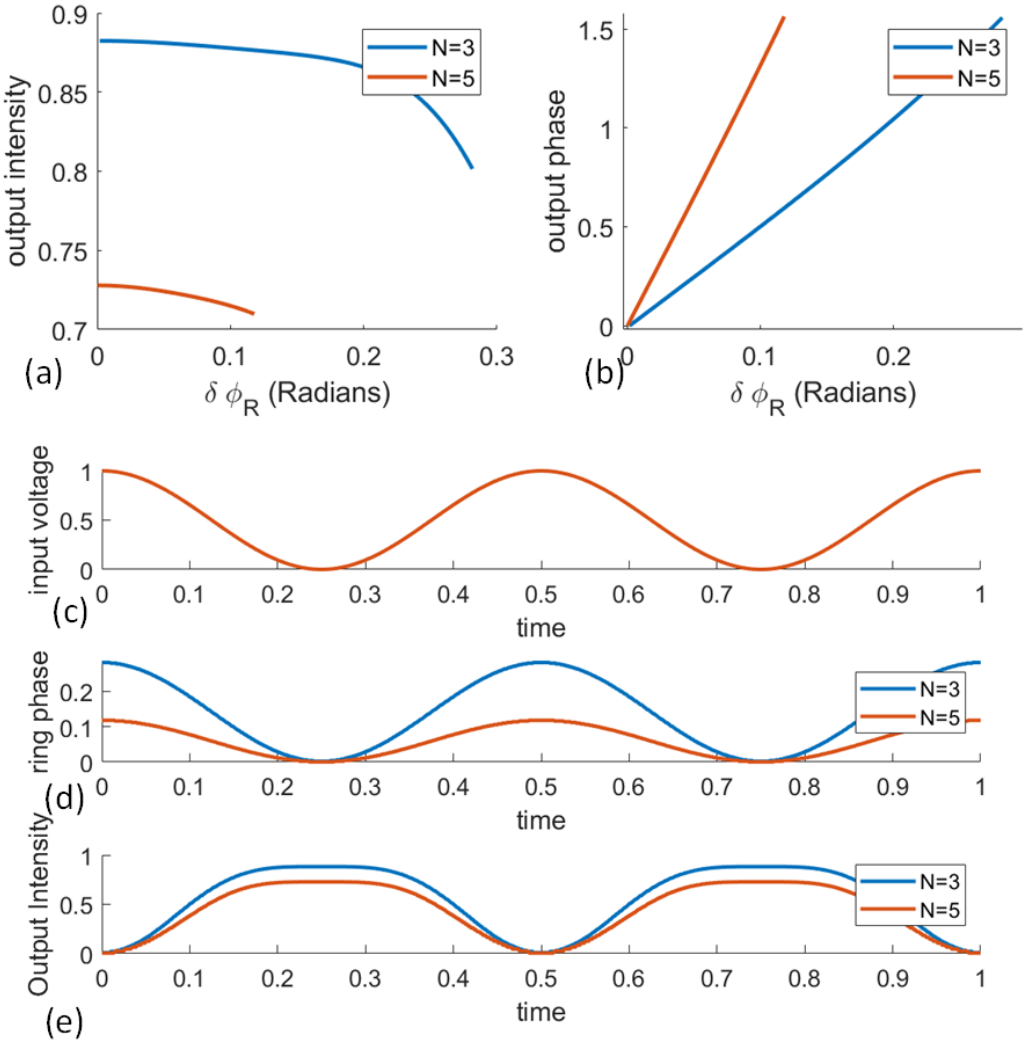

Figure 10.17: Nested ring-assisted MZI modulator. (a) Amplitude and (b) phase response of nested ring for N=3 and N=6 in each arm as a function of the fraction of wavelength phase increase to the total resonator round-trip in radians. (c) Sinusoidal input voltage. (d) Ring phase modulation. (e) Output intensity variations.

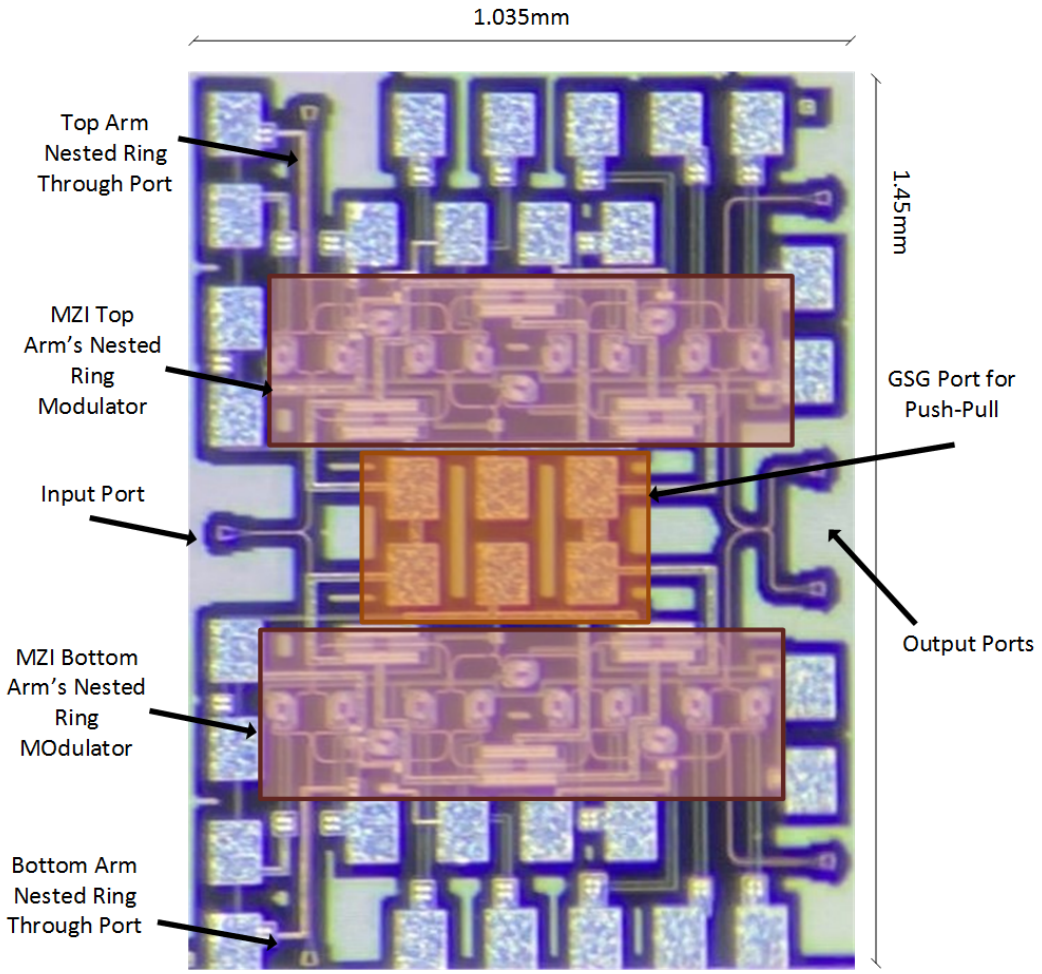

Figure 10.18: Die photo of the nested ring-assisted MZI.

BIBLIOGRAPHY

[1] L. B. Kish, "End of moore's law: Thermal (noise) death of integration in micro and nano electronics," *Physics Letters A*, vol. 305, no. 3, pp. 144–149, 2002, ISSN: 0375-9601. DOI: https://doi.org/10.1016/S0375-9601(02)01365-8. [Online]. Available: http://www.sciencedirect.com/science/article/pii/S0375960102013658.

[2] J. Hecht, "A short history of laser development," *Appl. Opt.*, vol. 49, no. 25, F99–F122, 2010. DOI: 10.1364/AO.49.000F99. [Online]. Available: http://ao.osa.org/abstract.cfm?URI=ao-49-25-F99.

[3] P. J. Winzer and D. T. Neilson, "From scaling disparities to integrated parallelism: A decathlon for a decade," *Journal of Lightwave Technology*, vol. 35, no. 5, pp. 1099–1115, 2017. DOI: 10.1109/JLT.2017.2662082.

[4] P. J. Winzer, "Spatial multiplexing in fiber optics: The 10x scaling of metro/core capacities," *Bell Labs Technical Journal*, vol. 19, pp. 22–30, 2014. DOI: 10.15325/BLTJ.2014.2347431.

[5] F. Vasey, F. K. Reinhart, R. Houdré, and J. M. Stauffer, "Spatial optical beam steering with an algaas integrated phased array," *Appl. Opt.*, vol. 32, no. 18, pp. 3220–3232, Jun. 1993. DOI: 10.1364/AO.32.003220. [Online]. Available: http://ao.osa.org/abstract.cfm?URI=ao-32-18-3220.

[6] H. Sasaki and R. M. De La Rue, "Electro-optic multichannel waveguide deflector," *Electronics Letters*, vol. 13, no. 10, pp. 295–296, 1977. DOI: 10.1049/el:19770216.

[7] R. A. Meyer, "Optical beam steering using a multichannel lithium tantalate crystal," *Appl. Opt.*, vol. 11, no. 3, pp. 613–616, Mar. 1972. DOI: 10.1364/AO.11.000613. [Online]. Available: http://ao.osa.org/abstract.cfm?URI=ao-11-3-613.

[8] M. Jarrahi, R. Fabian, W. Pease, D. Miller, and T. Lee, "High-speed optical beam-steering based on phase-arrayed waveguides," *Journal of Vacuum Science & Technology B: Microelectronics and Nanometer Structures Processing, Measurement, and Phenomena*, vol. 26, no. 6, pp. 2124–2126, 2008. DOI: 10.1116/1.2978945.

[9] J. K. Doylend, M. J. R. Heck, J. T. Bovington, J. D. Peters, L. A. Coldren, and J. E. Bowers, "Two-dimensional free-space beam steering with an optical phased array on silicon-on-insulator," *Opt. Express*, vol. 19, no. 22, pp. 21 595–21 604, Oct. 2011. DOI: 10.1364/OE.19.021595. [Online]. Available: http://www.opticsexpress.org/abstract.cfm?URI=oe-19-22-21595.

[10] J. Sun, E. Timurdogan, A. Yaacobi, E. S. Hosseini, and M. R. Watts, "Large-scale nanophotonic phased array," *Nature*, vol. 493, pp. 195–199, 2013. DOI: https://doi.org/10.1038/nature11727. [Online]. Available: http://dx.doi.org/10.1038/nature11727.

[11] F. Aflatouni, B. Abiri, A. Rekhi, and A. Hajimiri, "Nanophotonic coherent imager," *Opt. Express*, vol. 23, no. 4, pp. 5117–5125, Feb. 2015. DOI: 10.1364/OE.23.005117. [Online]. Available: http://www.opticsexpress.org/abstract.cfm?URI=oe-23-4-5117.

[12] F. Aflatouni, B. Abiri, A. Rekhi, and A. Hajimiri, "Nanophotonic projection system," *Opt. Express*, vol. 23, no. 16, pp. 21 012–21 022, Aug. 2015. DOI: 10.1364/OE.23.021012. [Online]. Available: http://www.opticsexpress.org/abstract.cfm?URI=oe-23-16-21012.

[13] T. Raj, F. Hashim, A. Huddin, M. Ibrahim, and A. Hussain, "A survey on lidar scanning mechanisms," *Electronics*, vol. 9, no. 5, p. 741, 2020. DOI: https://doi.org/10.3390/electronics9050741.

[14] L. Wu, X. Wang, X. He, Z. Huang, X. Huang, and C. Xiong, "Arbitrary multiple beam forming by two cascaded liquid crystal optical phased arrays," *Opt. Express*, vol. 26, no. 13, pp. 17 066–17 077, Jun. 2018. DOI: 10.1364/OE.26.017066. [Online]. Available: http://www.opticsexpress.org/abstract.cfm?URI=oe-26-13-17066.

[15] M. Iqbal, M. A. Gleeson, B. Spaugh, F. Tybor, W. G. Gunn, M. Hochberg, T. Baehr-Jones, R. C. Bailey, and L. C. Gunn, "Label-free biosensor arrays based on silicon ring resonators and high-speed optical scanning instrumentation," *IEEE Journal of Selected Topics in Quantum Electronics*, vol. 16, no. 3, pp. 654–661, 2010. DOI: 10.1109/JSTQE.2009.2032510.

[16] P. P. Khial, A. D. White, and A. Hajimiri, "Nanophotonic optical gyroscope with reciprocal sensitivity enhancement," *Nature Photon*, vol. 12, pp. 671–675, 2018. DOI: https://doi.org/10.1038/s41566-018-0266-5.

[17] R. Fatemi, A. Khachaturian, and A. Hajimiri, "A nonuniform sparse 2-D large-fov optical phased array with a low-power pwm drive," *IEEE Journal of Solid-State Circuits*, vol. 54, no. 5, pp. 1200–1215, 2019. DOI: 10.1109/JSSC.2019.2896767.

[18] P. P. Khial, A. White, F. Salehi, B. Hassibi, and A. Hajimiri, "A silicon photonics computational lensless active-flat-optics imaging system," *Sci Rep*, vol. 10, p. 1689, 2020. DOI: https://doi.org/10.1038/s41598-020-58027-1.

[19] H. A. Clevenson, S. J. Spector, L. Benney, M. G. Moebius, J. Brown, A. Hare, A. Huang, J. Mlynarczyk, C. V. Poulton, E. Hosseini, M. R. Watts, R. Dawson, J. P. Laine, and B. F. Lane, "Incoherent light imaging using an optical phased array," *Applied Physics Letters*, vol. 116, no. 3, p. 031 105, 2020. DOI: 10.1063/1.5130697.

[20] G. Zhang, J. Y. Haw, and H.Cai, "An integrated silicon photonic chip platform for continuous-variable quantum key distribution," *Nature Photon*, vol. 13, pp. 839–842, 2019. DOI: https://doi.org/10.1038/s41566-019-0504-5.

[21] M. H. Tahersima, K. Kojima, T. Koike-Akino, and et al., "Deep neural network inverse design of integrated photonic power splitters," *Sci Rep*, vol. 9, p. 1368, 2019. DOI: https://doi.org/10.1038/s41598-018-37952-2.

[22] R. Fatemi, A. Khachaturian, and A. Hajimiri, "Scalable optical phased array with sparse 2D aperture," in *Conference on Lasers and Electro-Optics*, Optical Society of America, 2018, STu4B.6. DOI: 10.1364/CLEO_SI.2018.STu4B.6. [Online]. Available: http://www.osapublishing.org/abstract.cfm?URI=CLEO_SI-2018-STu4B.6.

[23] M. Hochberg and T. Baehr-Jones, "Towards fabless silicon photonics," *Nature photonics*, vol. 4, no. 8, pp. 492–494, 2010. DOI: https://doi.org/10.1038/nphoton.2010.172.

[24] T. Pinguet, S. Denton, S. Gloeckner, M. Mack, G. Masini, A. Mekis, S. Pang, M. Peterson, S. Sahni, and P. D. Dobbelaere, "High-volume manufacturing platform for silicon photonics," *Proceedings of the IEEE*, vol. 106, no. 12, pp. 2281–2290, 2018. DOI: 10.1109/JPROC.2018.2859198.

[25] C. Sun, M. Wade, M. Georgas, S. Lin, L. Alloatti, B. Moss, R. Kumar, A. Atabaki, F. Pavanello, R. Ram, M. Popović, and V. Stojanović, "A 45nm soi monolithic photonics chip-to-chip link with bit-statistics-based resonant microring thermal tuning," in *2015 Symposium on VLSI Circuits (VLSI Circuits)*, 2015, pp. C122–C123. DOI: 10.1109/VLSIC.2015.7231348.

[26] A. Khachaturian, B. Abiri, A. Zhou, and A. Hajimiri, "Monolithic mach-zehnder interferometer modulator in an unmodified cmos process," in *2015 IEEE Photonics Conference (IPC)*, 2015, pp. 394–395. DOI: 10.1109/IPCon.2015.7323627.

[27] N. Dupuis, J. E. Proesel, N. Boyer, H. Ainspan, C. W. Baks, F. Doany, E. Cyr, and B. G. Lee, "An 8x8 silicon photonic switch module with nanosecond-scale reconfigurability," in *Optical Fiber Communication Conference Post-deadline Papers 2020*, Optical Society of America, 2020, Th4A.6. DOI: 10.1364/OFC.2020.Th4A.6. [Online]. Available: http://www.osapublishing.org/abstract.cfm?URI=OFC-2020-Th4A.6.

[28] L. Zimmermann, D. Knoll, M. Kroh, S. Lischke, D. Petousi, G. Winzer, and Y. Yamamoto, "Bicmos silicon photonics platform," in *Optical Fiber Communication Conference*, Optical Society of America, 2015, Th4E.5. DOI: 10.1364/OFC.2015.Th4E.5. [Online]. Available: http://www.osapublishing.org/abstract.cfm?URI=OFC-2015-Th4E.5.

[29] D. Thomson, A. Zilkie, J. E. Bowers, T. Komljenovic, G. T. Reed, L. Vivien, D. Marris-Morini, E. Cassan, L. Virot, J.-M. Fédéli, *et al.*, "Roadmap on silicon photonics," *Journal of Optics*, vol. 18, no. 7, p. 073 003, 2016. DOI: 10.1088/2040-8978/18/7/073003. [Online]. Available: https://doi.org/10.1088/2040-8978/18/7/073003.

[30] W. D. Sacher, Y. Huang, G.-Q. Lo, and J. K. S. Poon, "Multilayer silicon nitride-on-silicon integrated photonic platforms and devices," *J. Lightwave Technol.*, vol. 33, no. 4, pp. 901–910, Feb. 2015. DOI: 10.1109/JLT.2015.2392784. [Online]. Available: http://jlt.osa.org/abstract.cfm?URI=jlt-33-4-901.

[31] C. Koos, J. Leuthold, W. Freude, M. Kohl, L. Dalton, W. Bogaerts, A. L. Giesecke, M. Lauermann, A. Melikyan, S. Koeber, S. Wolf, C. Weimann, S. Muehlbrandt, K. Koehnle, J. Pfeifle, W. Hartmann, Y. Kutuvantavida, S. Ummethala, R. Palmer, D. Korn, L. Alloatti, P. C. Schindler, D. L. Elder, T. Wahlbrink, and J. Bolten, "Silicon-organic hybrid (soh) and plasmonic-organic hybrid (poh) integration," *Journal of Lightwave Technology*, vol. 34, no. 2, pp. 256–268, 2016. DOI: 10.1109/JLT.2015.2499763.

[32] L. Vivien and L. Pavesi, *Handbook of silicon photonics*. Taylor & Francis, 2016, ISBN: 9781439836101.

[33] W. D. Sacher, Y. Huang, L. Ding, B. J. F. Taylor, H. Jayatilleka, G.-Q. Lo, and J. K. S. Poon, "Wide bandwidth and high coupling efficiency si3n4-on-soi dual-level grating coupler," *Opt. Express*, vol. 22, no. 9, pp. 10 938–10 947, May 2014. DOI: 10.1364/OE.22.010938. [Online]. Available: http://www.opticsexpress.org/abstract.cfm?URI=oe-22-9-10938.

[34] M. Papes, P. Cheben, D. Benedikovic, J. H. Schmid, J. Pond, R. Halir, A. Ortega-Moñux, G. Wangüemert-Pérez, W. N. Ye, D.-X. Xu, S. Janz, M. Dado, and V. Vašinek, "Fiber-chip edge coupler with large mode size for silicon photonic wire waveguides," *Opt. Express*, vol. 24, no. 5, pp. 5026–5038, Mar. 2016. DOI: 10.1364/OE.24.005026. [Online]. Available: http://www.opticsexpress.org/abstract.cfm?URI=oe-24-5-5026.

[35] R. Fatemi, P. P. Khial, A. Khachaturian, and A. Hajimiri, "Breaking fov-aperture trade-off with multi-mode nano-photonic antennas," *IEEE Journal of Selected Topics in Quantum Electronics*, vol. 27, no. 1, pp. 1–14, 2021. DOI: 10.1109/JSTQE.2020.3026966.

[36] N. Abadia, T. Bernadin, P. Chaisakul, S. Olivier, D. Marris-Morini, R. E. de Lamaëstre, J. Weeber, and L. Vivien, "Low-power consumption franz-keldysh effect plasmonic modulator," *Optics express*, vol. 22, no. 9, pp. 11 236–11 243, 2014. DOI: 10.1364/OE.22.011236. [Online]. Available: http://www.opticsexpress.org/abstract.cfm?URI=oe-22-9-11236.

[37] N. C. Harris, Y. Ma, J. Mower, T. Baehr-Jones, D. Englund, M. Hochberg, and C. Galland, "Efficient, compact and low loss thermo-optic phase shifter in silicon," *Optics express*, vol. 22, no. 9, pp. 10 487–10 493, 2014. DOI: 10.1364/OE.22.010487. [Online]. Available: http://www.opticsexpress.org/abstract.cfm?URI=oe-22-9-10487.

[38] M. Nedeljkovic, R. Soref, and G. Z. Mashanovich, "Free-carrier electrorefraction and electroabsorption modulation predictions for silicon over the 1-4um infrared wavelength range," *IEEE Photonics Journal*, vol. 3, no. 6, pp. 1171–1180, 2011. DOI: doi:10.1109/JPHOT.2011.2171930.

[39] S. Wolf, H. Zwickel, W. Hartmann, M. Lauermann, Y. Kutuvantavida, C. Kieninger, L. Altenhain, R. Schmid, J. Luo, A. K.-Y. Jen, *et al.*, "Silicon-organic hybrid (soh) mach-zehnder modulators for 100 gbit/s on-off keying," *Scientific reports*, vol. 8, no. 1, pp. 1–13, 2018. DOI: https://doi.org/10.1038/s41598-017-19061-8.

[40] M. Huang, P. Cai, S. Li, L. Wang, T.-I. Su, L. Zhao, W. Chen, C.-y. Hong, and D. Pan, "Breakthrough of 25gb/s germanium on silicon avalanche photodiode," in *Optical Fiber Communication Conference*, Optical Society of America, 2016, Tu2D–2, ISBN: 978-1-5090-0735-6.

[41] Y. Zhang, S. Yang, Y. Yang, M. Gould, N. Ophir, A. E.-J. Lim, G.-Q. Lo, P. Magill, K. Bergman, T. Baehr-Jones, *et al.*, "A high-responsivity photodetector absent metal-germanium direct contact," *Optics express*, vol. 22, no. 9, pp. 11 367–11 375, 2014. DOI: 10.1364/OE.22.011367. [Online]. Available: http://www.opticsexpress.org/abstract.cfm?URI=oe-22-9-11367.

[42] A. Moscoso-Mártir, A. Tabatabaei-Mashayekh, J. Müller, J. Nojić, R. Setter, M. Nielsen, A. Sandomirsky, S. Rockman, E. Mentovich, F. Merget, *et al.*, "8-channel wdm silicon photonics transceiver with soa and semiconductor mode-locked laser," *Optics express*, vol. 26, no. 19, pp. 25 446–25 459, 2018. DOI: 10.1364/OE.26.025446. [Online]. Available: http://www.opticsexpress.org/abstract.cfm?URI=oe-26-19-25446.

[43] C. V. Poulton, M. J. Byrd, P. Russo, E. Timurdogan, M. Khandaker, D. Vermeulen, and M. R. Watts, "Long-range lidar and free-space data communication with high-performance optical phased arrays," *IEEE Journal of Selected Topics in Quantum Electronics*, vol. 25, no. 5, pp. 1–8, 2019. DOI: 10.1109/JSTQE.2019.2908555.

[44] S. Chung, H. Abediasl, and H. Hashemi, "15.4 a 1024-element scalable optical phased array in 0.18μm soi cmos," in *2017 IEEE International Solid-State Circuits Conference (ISSCC)*, 2017, pp. 262–263. DOI: 10.1109/ISSCC.2017.7870361.

[45] H. Abediasl and H. Hashemi, "Monolithic optical phased-array transceiver in a standard soi cmos process," *Opt. Express*, vol. 23, no. 5, pp. 6509–6519, Mar. 2015. DOI: 10.1364/OE.23.006509. [Online]. Available: http://www.opticsexpress.org/abstract.cfm?URI=oe-23-5-6509.

[46] P. P. Vaidyanathan and P. Pal, "Mimo radar, simo radar, and ifir radar: A comparison," in *2009 Conference Record of the Forty-Third Asilomar Conference on Signals, Systems and Computers*, 2009, pp. 160–167. DOI: 10.1109/ACSSC.2009.5470139.

[47] C. Balanis, *Antenna Theory: Analysis and Design*. Wiley, 2015, ISBN: 978-1-119-17899-6. [Online]. Available: https://www.wiley.com/en-us/Antenna+Theory%5C%3A+Analysis+and+Design%5C%2C+4th+Edition-p-9781118642061.

[48] R. Hansen, *Phased Array Antennas*, ser. Wiley Series in Microwave and Optical Engineering. Wiley, 2009, ISBN: 9780470529171. [Online]. Available: https://books.google.com/books?id=vVtnDPhi43YC.

[49] W. Xie, T. Komljenovic, J. Huang, M. L. Davenport, and J. E. Bowers, *Dense iii-v/si phase-shifter based optical phased array*, 2019. arXiv: 1904.01104 [physics.app-ph].

[50] M. Raval, C. V. Poulton, and M. R. Watts, "Unidirectional waveguide grating antennas for nanophotonic phased arrays," in *Conference on Lasers and Electro-Optics*, Optical Society of America, 2017, STh1M.5. DOI: 10.1364/CLEO_SI.2017.STh1M.5. [Online]. Available: http://www.osapublishing.org/abstract.cfm?URI=CLEO_SI-2017-STh1M.5.

[51] W. Xie, J. Huang, T. Komljenovic, L. Coldren, and J. Bowers, *Diffraction limited centimeter scale radiator: Metasurface grating antenna for phased array lidar*, 2018. arXiv: 1810.00109 [physics.app-ph].

[52] J. C. Hulme, J. K. Doylend, M. J. R. Heck, J. D. Peters, M. L. Davenport, J. T. Bovington, L. A. Coldren, and J. E. Bowers, "Fully integrated hybrid silicon two dimensional beam scanner," *Opt. Express*, vol. 23, no. 5, pp. 5861–5874, Mar. 2015. DOI: 10.1364/OE.23.005861. [Online]. Available: http://www.opticsexpress.org/abstract.cfm?URI=oe-23-5-5861.

[53] C. V. Poulton, M. J. Byrd, B. Moss, E. Timurdogan, R. Millman, and M. R. Watts, "8192-element optical phased array with 100° steering range and flip-chip cmos," in *Conference on Lasers and Electro-Optics*, Optical Society of America, 2020, JTh4A.3. DOI: https://doi.org/10.1364/CLEO_AT.2020.JTh4A.3. [Online]. Available: http://www.osapublishing.org/abstract.cfm?URI=CLEO_SI-2020-JTh4A.3.

[54] S. A. Miller, C. T. Phare, Y.-C. Chang, X. Ji, O. A. J. Gordillo, A. Mohanty, S. P. Roberts, M. C. Shin, B. Stern, M. Zadka, and M. Lipson, "512-element actively steered silicon phased array for low-power lidar,"

in *Conference on Lasers and Electro-Optics*, Optical Society of America, 2018, JTh5C.2, ISBN: 978-1-5386-5733-1. [Online]. Available: http://www.osapublishing.org/abstract.cfm?URI=CLEO_QELS-2018-JTh5C.2.

[55] T. Kim, P. Bhargava, C. V. Poulton, J. Notaros, A. Yaacobi, E. Timurdogan, C. Baiocco, N. Fahrenkopf, S. Kruger, T. Ngai, Y. Timalsina, M. R. Watts, and V. Stojanović, "A single-chip optical phased array in a wafer-scale silicon photonics/cmos 3d-integration platform," *IEEE Journal of Solid-State Circuits*, vol. 54, no. 11, pp. 3061–3074, 2019. DOI: 10.1109/JSSC.2019.2934601.

[56] P. Wang, G. Luo, Y. Li, W. Yang, H. Yu, X. Zhou, Y. Zhang, and J. Pan, "Large scanning range optical phased array with a compact and simple optical antenna," *Microelectronic Engineering*, vol. 224, p. 111 237, 2020, ISSN: 0167-9317. DOI: https://doi.org/10.1016/j.mee.2020.111237. [Online]. Available: http://www.sciencedirect.com/science/article/pii/S0167931720300253.

[57] W. Ma, S. Tan, K. Wang, W. Guo, Y. Liu, L. Liao, L. Zhou, J. Zhou, X. Li, L. Liang, and W. Li, "Practical two-dimensional beam steering system using an integrated tunable laser and an optical phased array," *Appl. Opt.*, vol. 59, no. 32, pp. 9985–9994, Nov. 2020. DOI: 10.1364/AO.403314. [Online]. Available: http://ao.osa.org/abstract.cfm?URI=ao-59-32-9985.

[58] J. Notaros, N. Li, C. V. Poulton, Z. Su, M. J. Byrd, E. S. Magden, E. Timurdogan, C. Baiocco, N. M. Fahrenkopf, and M. R. Watts, "Cmos-compatible optical phased array powered by a monolithically-integrated erbium laser," *J. Lightwave Technol.*, vol. 37, no. 24, pp. 5982–5987, Dec. 2019. DOI: 10.1109/JLT.2019.2944607. [Online]. Available: http://jlt.osa.org/abstract.cfm?URI=jlt-37-24-5982.

[59] K. Wagner, N. Dostart, B. Zhang, M. Brand, D. Feldkhun, and M. Popović, "Scalable: Self-calibrated adaptive lidar aperture beamsteering light engine," in *Imaging and Applied Optics 2019 (COSI, IS, MATH, pcAOP)*, Optical Society of America, 2019, CTh2A.5. DOI: 10.1364/COSI.2019.CTh2A.5. [Online]. Available: http://www.osapublishing.org/abstract.cfm?URI=COSI-2019-CTh2A.5.

[60] N. Dostart, B. Zhang, A. Khilo, M. Brand, K. A. Qubaisi, D. Onural, D. Feldkhun, K. H. Wagner, and M. A. Popović, "Serpentine optical phased arrays for scalable integrated photonic lidar beam steering," *Optica*, vol. 7, no. 6, pp. 726–733, Jun. 2020. DOI: 10.1364/OPTICA.389006. [Online]. Available: http://www.osapublishing.org/optica/abstract.cfm?URI=optica-7-6-726.

[61] D. G. Leeper, "Isophoric arrays-massively thinned phased arrays with well-controlled sidelobes," *IEEE Transactions on Antennas and Propagation*, vol. 47, no. 12, pp. 1825–1835, 1999. DOI: 10.1109/8.817659.

[62] A. Moffet, "Minimum-redundancy linear arrays," *IEEE Transactions on Antennas and Propagation*, vol. 16, no. 2, pp. 172–175, 1968. DOI: 10.1109/TAP.1968.1139138.

[63] S. S. Brunke and G. R. Lockwood, "Broad-bandwidth radiation patterns of sparse two-dimensional vernier arrays," *IEEE Transactions on Ultrasonics, Ferroelectrics, and Frequency Control*, vol. 44, no. 5, pp. 1101–1109, 1997. DOI: 10.1109/58.655635.

[64] P. Pal and P. P. Vaidyanathan, "Nested arrays: A novel approach to array processing with enhanced degrees of freedom," *IEEE Transactions on Signal Processing*, vol. 58, no. 8, pp. 4167–4181, 2010. DOI: 10.1109/TSP.2010.2049264.

[65] D. N. Hutchison, J. Sun, J. K. Doylend, R. Kumar, J. Heck, W. Kim, C. T. Phare, A. Feshali, and H. Rong, "High-resolution aliasing-free optical beam steering," *Optica*, vol. 3, no. 8, pp. 887–890, Aug. 2016. DOI: 10.1364/OPTICA.3.000887. [Online]. Available: http://www.osapublishing.org/optica/abstract.cfm?URI=optica-3-8-887.

[66] N. Dostart, M. Brand, B. Zhang, D. Feldkhun, K. Wagner, and M. A. Popović, "Vernier si-photonic phased array transceiver for grating lobe suppression and extended field-of-view," in *Conference on Lasers and Electro-Optics*, Optical Society of America, 2019, AW3K.2. DOI: 10.1364/CLEO_AT.2019.AW3K.2. [Online]. Available: http://www.osapublishing.org/abstract.cfm?URI=CLEO_AT-2019-AW3K.2.

[67] L. Wu, Z. Zhang, and H. Liu, "Transmit beamforming for mimo optical wireless communication systems," *Wireless Pers Commun*, vol. 78, pp. 615–628, Apr. 2014. DOI: https://doi.org/10.1007/s11277-014-1774-3.

[68] H. singh, H. Sneha, and R. Jha, "Mutual coupling in phased arrays:a review," *Hindawi Publications*, 2013. DOI: https://doi.org/10.1155/2013/348123.

[69] P. P. Vaidyanathan and P. Pal, "Sparse sensing with coprime arrays," in *2010 Conference Record of the Forty Fourth Asilomar Conference on Signals, Systems and Computers*, 2010, pp. 1405–1409. DOI: 10.1109/ACSSC.2010.5757766.

[70] ——, "Sparse sensing with co-prime samplers and arrays," *IEEE Transactions on Signal Processing*, vol. 59, no. 2, pp. 573–586, 2011. DOI: 10.1109/TSP.2010.2089682.

[71] J. Sun, E. shah Hosseini, A. Yaacobi, D. B. Cole, G. Leake, D. Coolbaugh, and M. R. Watts, "Two-dimensional apodized silicon photonic phased arrays," *Opt. Lett.*, vol. 39, no. 2, pp. 367–370, Jan. 2014. DOI: 10.1364/OL.39.000367. [Online]. Available: http://ol.osa.org/abstract.cfm?URI=ol-39-2-367.

[72] B. Gramatikov, *Handbook of Biomedical Optics*. CRC Press, 2011, ISBN: 9781420090369. [Online]. Available: https://www.worldcat.org/title/handbook-of-biomedical-optics/oclc/672978818.

[73] M. E. Bialkowski and N. C. Karmakar, "A two-ring circular phased-array antenna for mobile satellite communications," *IEEE Antennas and Propagation Magazine*, vol. 41, no. 3, pp. 14–23, 1999. DOI: 10.1109/74.775244.

[74] N. H. Noordin, V. Zuniga, A. O. El-Rayis, N. Haridas, A. T. Erdogan, and T. Arslan, "Uniform circular arrays for phased array antenna," in *2011 Loughborough Antennas Propagation Conference*, 2011, pp. 1–4. DOI: 10.1109/LAPC.2011.6114031.

[75] M. S. Eggleston, F. Pardo, C. Bolle, B. Farah, N. Fontaine, H. Safar, M. Cappuzzo, C. Pollock, D. J. Bishop, and M. P. Earnshaw, "90db sensitivity in a chip-scale swept-source optical coherence tomography system," in *Conference on Lasers and Electro-Optics*, Optical Society of America, 2018, JTh5C.8. DOI: 10.1364/CLEO_AT.2018.JTh5C.8. [Online]. Available: http://www.osapublishing.org/abstract.cfm?URI=CLEO_AT-2018-JTh5C.8.

[76] B. Behroozpour, P. A. M. Sandborn, N. Quack, T. J. Seok, Y. Matsui, M. C. Wu, and B. E. Boser, "11.8 chip-scale electro-optical 3d fmcw lidar with 8um ranging precision," in *2016 IEEE International Solid-State Circuits Conference (ISSCC)*, 2016, pp. 214–216. DOI: 10.1109/ISSCC.2016.7417983.

[77] J. A. Christian and S. Cryan, "A survey of lidar technology and its use in spacecraft relative navigation," in *AIAA Guidance, Navigation, and Control (GNC) Conference*. DOI: 10.2514/6.2013-4641. eprint: https://arc.aiaa.org/doi/pdf/10.2514/6.2013-4641. [Online]. Available: https://arc.aiaa.org/doi/abs/10.2514/6.2013-4641.

[78] N. Satyan, A. Vasilyev, G. Rakuljic, V. Leyva, and A. Yariv, "Precise control of broadband frequency chirps using optoelectronic feedback," *Opt. Express*, vol. 17, no. 18, pp. 15 991–15 999, Aug. 2009. DOI: 10.1364/OE.17.015991. [Online]. Available: http://www.opticsexpress.org/abstract.cfm?URI=oe-17-18-15991.

[79] V. Vercesi, D. Onori, F. Laghezza, F. Scotti, A. Bogoni, and M. Scaffardi, "Frequency-agile dual-frequency lidar for integrated coherent radar-lidar architectures," *Opt. Lett.*, vol. 40, no. 7, pp. 1358–1361, Apr. 2015. DOI: 10.1364/OL.40.001358. [Online]. Available: http://ol.osa.org/abstract.cfm?URI=ol-40-7-1358.

[80] I. Coddington, W. Swann, L. Nenadovic, and et al., "Rapid and precise absolute distance measurements at long range," *Nature Photon*, vol. 3, pp. 351–356, 2009. DOI: https://doi.org/10.1038/nphoton.2009.94.

[81] W. C. Swann and N. R. Newbury, "Frequency-resolved coherent lidar using a femtosecond fiber laser," *Opt. Lett.*, vol. 31, no. 6, pp. 826–828, Mar. 2006. DOI: 10.1364/OL.31.000826. [Online]. Available: http://ol.osa.org/abstract.cfm?URI=ol-31-6-826.

[82] P. Adany, C. Allen, and R. Hui, "Chirped lidar using simplified homodyne detection," *Journal of Lightwave Technology*, vol. 27, no. 16, pp. 3351–3357, 2009. DOI: 10.1109/JLT.2009.2016220.

[83] S. Gao and R. Hui, "Frequency-modulated continuous-wave lidar using i/q modulator for simplified heterodyne detection," *Opt. Lett.*, vol. 37, no. 11, pp. 2022–2024, Jun. 2012. DOI: 10.1364/OL.37.002022. [Online]. Available: http://ol.osa.org/abstract.cfm?URI=ol-37-11-2022.

[84] M. Kashmiri, B. Behroozpour, V. Petkov, K. Wojciechowski, and C. Lang, "23.1 a 4gs/s 80db dr current-domain analog front-end for phase-coded pulse-compression direct time-of-flight automotive lidar," in *2020 IEEE International Solid- State Circuits Conference - (ISSCC)*, 2020, pp. 344–346. DOI: 10.1109/ISSCC19947.2020.9062993.

[85] Z. Xu, L. Tang, H. Zhang, and S. Pan, "Simultaneous real-time ranging and velocimetry via a dual-sideband chirped lidar," *IEEE Photonics Technology Letters*, vol. 29, no. 24, pp. 2254–2257, 2017. DOI: 10.1109/LPT.2017.2771415.

[86] S. Gao, M. O'Sullivan, and R. Hui, "Complex-optical-field lidar system for range and vector velocity measurement," *Opt. Express*, vol. 20, no. 23, pp. 25 867–25 875, Nov. 2012. DOI: 10.1364/OE.20.025867. [Online]. Available: http://www.opticsexpress.org/abstract.cfm?URI=oe-20-23-25867.

[87] D. G. Girton, S. L. Kwiatkowski, G. F. Lipscomb, and R. S. Lytel, "20 ghz electro-optic polymer mach–zehnder modulator," *Applied Physics Letters*, vol. 58, no. 16, pp. 1730–1732, 1991. DOI: 10.1063/1.105123.

[88] T. Baehr-Jones, R. Ding, Y. Liu, A. Ayazi, T. Pinguet, N. C. Harris, M. Streshinsky, P. Lee, Y. Zhang, A. E.-J. Lim, T.-Y. Liow, S. H.-G. Teo, G.-Q. Lo, and M. Hochberg, "Ultralow drive voltage silicon traveling-wave modulator," *Opt. Express*, vol. 20, no. 11, pp. 12 014–12 020, May 2012. DOI: 10.1364/OE.20.012014. [Online]. Available: http://www.opticsexpress.org/abstract.cfm?URI=oe-20-11-12014.

[89] Y. Chen, M. Kibune, A. Toda, A. Hayakawa, T. Akiyama, S. Sekiguchi, H. Ebe, N. Imaizumi, T. Akahoshi, S. Akiyama, S. Tanaka, T. Simoyama, K. Morito, T. Yamamoto, T. Mori, Y. Koyanagi, and H. Tamura, "22.2 a 25gb/s hybrid integrated silicon photonic transceiver in 28nm cmos and soi," in *2015 IEEE International Solid-State Circuits Conference - (ISSCC) Digest of Technical Papers*, 2015, pp. 1–3. DOI: 10.1109/ISSCC.2015.7063096.

[90] B. R. Moss, C. Sun, M. Georgas, J. Shainline, J. S. Orcutt, J. C. Leu, M. Wade, Y. Chen, K. Nammari, X. Wang, H. Li, R. Ram, M. A. Popovic, and V. Stojanovic, "A 1.23pj/b 2.5gb/s monolithically integrated optical carrier-injection ring modulator and all-digital driver circuit in commercial 45nm soi," in *2013 IEEE International Solid-State Circuits Conference Digest of Technical Papers*, 2013, pp. 126–127. DOI: 10.1109/ISSCC.2013.6487666.

[91] J. H. Song, R. A. Budd, B. G. Lee, C. L. Schow, and F. R. Libsch, "Focusing grating couplers in unmodified 180-nm silicon-on-insulator cmos," *IEEE Photonics Technology Letters*, vol. 26, no. 8, pp. 825–828, 2014. DOI: 10.1109/LPT.2014.2306999.

[92] G. T. Reed, G. Z. Mashanovich, F. Y. Gardes, M. Nedeljkovic, Y. Hu, D. J. Thomson, K. Li, P. R. Wilson, S.-W. Chen, and S. S. Hsu, "Recent breakthroughs in carrier depletion based silicon optical modulators," *Nanophotonics*, vol. 3, no. 4-5, pp. 229–245, 2014. DOI: https://doi.org/10.1515/nanoph-2013-0016. [Online]. Available: https://www.degruyter.com/view/journals/nanoph/3/4-5/article-p229.xml.

[93] Z. Yong, W. D. Sacher, Y. Huang, J. C. Mikkelsen, Y. Yang, X. Luo, P. Dumais, D. Goodwill, H. Bahrami, P. G.-Q. Lo, E. Bernier, and J. K. S. Poon, "U-shaped pn junctions for efficient silicon mach-zehnder and microring modulators in the o-band," *Opt. Express*, vol. 25, no. 7, pp. 8425–8439, Apr. 2017. DOI: 10.1364/OE.25.008425. [Online]. Available: http://www.opticsexpress.org/abstract.cfm?URI=oe-25-7-8425.

[94] D. Petousi, P. Rito, S. Lischke, D. Knoll, I. Garcia-Lopez, M. Kroh, R. Barth, C. Mai, A. Ulusoy, A. Peczek, G. Winzer, K. Voigt, D. Kissinger, K. Petermann, and L. Zimmermann, "Monolithically integrated high-extinction-ratio mzm with a segmented driver in photonic bicmos," *IEEE Photonics Technology Letters*, vol. 28, no. 24, pp. 2866–2869, 2016. DOI: 10.1109/LPT.2016.2624700.

[95] A. Brimont, D. J. Thomson, P. Sanchis, J. Herrera, F. Gardes, J. M. Fedeli, G. T. Reed, and J. Martí, "High speed silicon electro-optical modulators enhanced via slow light propagation," *Opt. Express*, vol. 19, no. 21, pp. 20 876–20 885, Oct. 2011. DOI: 10.1364/OE.19.020876. [Online]. Available: http://www.opticsexpress.org/abstract.cfm?URI=oe-19-21-20876.

[96] A. Brimont, A. M. Gutierrez, M. Aamer, D. J. Thomson, F. Y. Gardes, J. Fedeli, G. T. Reed, J. Marti, and P. Sanchis, "Slow-light-enhanced silicon optical modulators under low-drive-voltage operation," *IEEE Photonics Journal*, vol. 4, no. 5, pp. 1306–1315, 2012. DOI: 10.1109/JPHOT.2012.2207884.

[97] H. Yu and W. Bogaerts, "An equivalent circuit model of the traveling wave electrode for carrier-depletion-based silicon optical modulators," *Journal of Lightwave Technology*, vol. 30, no. 11, pp. 1602–1609, 2012. DOI: 10.1109/JLT.2012.2188779.

[98] S. Hosseini and K. Jamshidi, "Enhancement of bandwidth-energy consumption tradeoffs in reverse-biased modulators," in *2016 IEEE Photonics Society Summer Topical Meeting Series (SUM)*, 2016, pp. 94–95. DOI: 10.1109/PHOSST.2016.7548737.

[99] R. Hosseini and K. Jamshidi, "Performance analysis of reverse biased silicon mach-zehnder modulators using slow light corrugated waveguides: Bandwidth and loss study," in *2017 International Topical Meeting on Microwave Photonics (MWP)*, 2017, pp. 1–4. DOI: 10.1109/MWP.2017.8168737.

[100] Y. Miyamoto and M. Tomizawa, "6.2 high-capacity scalable optical communication for future optical transport network," in *2014 IEEE International Solid-State Circuits Conference Digest of Technical Papers (ISSCC)*, 2014, pp. 118–119. DOI: 10.1109/ISSCC.2014.6757363.

[101] F. Gan and F. X. Kartner, "High-speed silicon electrooptic modulator design," *IEEE Photonics Technology Letters*, vol. 17, no. 5, pp. 1007–1009, 2005. DOI: 10.1109/LPT.2005.846756.

[102] M. Notaros, M. Raval, J. Notaros, and M. R. Watts, "Integrated visible-light liquid-crystal phase modulator," in *Frontiers in Optics*, Optical Society of America, 2018, FW6B–5. DOI: 10.1364/FIO.2018.FW6B.5. [Online]. Available: http://www.osapublishing.org/abstract.cfm?URI=FiO-2018-FW6B.5.

[103] M. F. Rosa, L. Rathgeber, R. Elster, N. Hoppe, T. Föhn, M. Schmidt, W. Vogel, and M. Berroth, "Design of a carrier-depletion mach-zehnder modulator in 250 nm silicon-on-insulator technology," *Advances in Radio Science: ARS*, vol. 15, p. 269, 2017. DOI: 10.5194/ars-15-269-2017.

[104] M. Webster, K. Lakshmikumar, C. Appel, C. Muzio, B. Dama, and K. Shastri, "Low-power mos-capacitor based silicon photonic modulators and cmos drivers," in *2015 Optical Fiber Communications Conference and Exhibition (OFC)*, 2015, pp. 1–3. DOI: 10.1364/OFC.2015.W4H.3.

[105] S. Yu and T. Chu, "Electrical nonlinearity in silicon modulators based on reversed pn junctions," *Photon. Res.*, vol. 5, no. 2, pp. 124–128, Apr. 2017. DOI: 10.1364/PRJ.5.000124. [Online]. Available: http://www.osapublishing.org/prj/abstract.cfm?URI=prj-5-2-124.

[106] E. Timurdogan, C. V. Poulton, M. Byrd, and M. Watts, "Electric field-induced second-order nonlinear optical effects in silicon waveguides," *Nature Photonics*, vol. 11, no. 3, pp. 200–206, 2017. DOI: https://doi.org/10.1038/nphoton.2017.14.

[107] C. R. Doerr, L. Zhang, P. J. Winzer, J. H. Sinsky, A. L. Adamiecki, N. J. Sauer, and G. Raybon, "Compact high-speed inp dqpsk modulator," *IEEE Photonics Technology Letters*, vol. 19, no. 15, pp. 1184–1186, 2007. DOI: 10.1109/LPT.2007.901588.

[108] C. Wang, M. Zhang, X. Chen, M. Bertrand, A. Shams-Ansari, S. Chandrasekhar, P. Winzer, and M. Lončar, "Integrated lithium niobate electro-optic modulators operating at cmos-compatible voltages," *Nature*, vol. 562, no. 7725, pp. 101–104, 2018. DOI: https://doi.org/10.1038/s41586-018-0551-y.

[109] Y. Ogiso, J. Ozaki, Y. Ueda, N. Kashio, N. Kikuchi, E. Yamada, H. Tanobe, S. Kanazawa, H. Yamazaki, Y. Ohiso, T. Fujii, and M. Kohtoku, "Over 67 ghz bandwidth and 1.5 v vpi inp-based optical iq modulator with n-i-p-n heterostructure," *Journal of Lightwave Technology*, vol. 35, no. 8, pp. 1450–1455, 2017. DOI: 10.1109/JLT.2016.2639542.

[110] R. Jones, P. Doussiere, J. B. Driscoll, W. Lin, H. Yu, Y. Akulova, T. Komljenovic, and J. E. Bowers, "Heterogeneously integrated inp-silicon photonics: Fabricating fully functional transceivers," *IEEE Nanotechnology Magazine*, vol. 13, no. 2, pp. 17–26, 2019. DOI: 10.1109/MNANO.2019.2891369.

[111] F. Eltes, C. Mai, D. Caimi, M. Kroh, Y. Popoff, G. Winzer, D. Petousi, S. Lischke, J. E. Ortmann, L. Czornomaz, L. Zimmermann, J. Fompeyrine, and S. Abel, "A batio3-based electro-optic pockels modulator monolithically integrated on an advanced silicon photonics platform," *Journal of Lightwave Technology*, vol. 37, no. 5, pp. 1456–1462, 2019. DOI: 10.1109/JLT.2019.2893500.

[112] A. Rao, A. Patil, P. Rabiei, A. Honardoost, R. DeSalvo, A. Paolella, and S. Fathpour, "High-performance and linear thin-film lithium niobate mach–zehnder modulators on silicon up to 50 ghz," *Optics letters*, vol. 41, no. 24, pp. 5700–5703, 2016. DOI: 10.1364/OL.41.005700. [Online]. Available: http://ol.osa.org/abstract.cfm?URI=ol-41-24-5700.

[113] C. Kieninger, C. Füllner, H. Zwickel, Y. Kutuvantavida, J. N. Kemal, C. Eschenbaum, D. L. Elder, L. R. Dalton, W. Freude, S. Randel, and C. Koos, "Soh mach-zehnder modulators for 100 gbd pam4 signaling with sub-1 db phase-shifter loss," in *2020 Optical Fiber Communications Conference and Exhibition (OFC)*, 2020, pp. 1–3, ISBN: 978-1-9435-8071-2.

[114] Y. Bai, N. Song, J. P. Gao, X. Sun, X. Wang, G. Yu, and Z. Y. Wang, "A new approach to highly electrooptically active materials using cross-linkable, hyperbranched chromophore-containing oligomers as a macromolecular dopant," *Journal of the American Chemical Society*, vol. 127, no. 7, pp. 2060–2061, 2005. DOI: https://doi.org/10.1021/ja042854f.

[115] D. Jin, H. Chen, A. Barklund, J. Mallari, G. Yu, E. Miller, and R. Dinu, "Eo polymer modulators reliability study," in *Organic Photonic Materials and Devices XII*, International Society for Optics and Photonics, vol. 7599, 2010, 75990H. DOI: https://doi.org/10.1117/12.837418.

[116] R. Dinu, D. Jin, G. Yu, B. Chen, D. Huang, H. Chen, A. Barklund, E. Miller, C. Wei, and J. Vemagiri, "Environmental stress testing of electro–optic polymer modulators," *Journal of Lightwave Technology*, vol. 27, no. 11, pp. 1527–1532, 2009. DOI: 10.1109/JLT.2009.2014178.

[117] G. Yu, E. Miller, J. Mallari, C. Wei, B. Chen, H. Chen, V. Shofman, and R. Dinu, "Small form factor thin film polymer modulators for telecom applications," in *OFC/NFOEC*, 2012, pp. 1–3. DOI: https://doi.org/10.1364/OFC.2012.OM3J.1.

[118] J. Mallari, C. Wei, D. Jin, G. Yu, A. Barklund, E. Miller, P. O'Mathuna, R. Dinu, A. Motafakker-Fard, and B. Jalali, "100gbps eo polymer modulator product and its characterization using a real-time digitizer," in *Optical Fiber Communication Conference*, Optical Society of America, 2010, OThU2. DOI: 10.1364/OFC.2010.OThU2. [Online]. Available: http://www.osapublishing.org/abstract.cfm?URI=OFC-2010-OThU2.

[119] R. Amin, R. Maiti, C. Carfano, Z. Ma, M. H. Tahersima, Y. Lilach, D. Ratnayake, H. Dalir, and V. J. Sorger, "0.52 v mm ito-based mach-zehnder modulator in silicon photonics," *APL Photonics*, vol. 3, no. 12, p. 126 104, 2018. DOI: https://doi.org/10.1063/1.5052635.

[120] J.-M. Brosi, C. Koos, L. C. Andreani, M. Waldow, J. Leuthold, and W. Freude, "High-speed low-voltage electro-optic modulator with a polymer-infiltrated silicon photonic crystal waveguide," *Opt. Express*, vol. 16, no. 6, pp. 4177–4191, Mar. 2008. DOI: 10.1364/OE.16.004177. [Online]. Available: http://www.opticsexpress.org/abstract.cfm?URI=oe-16-6-4177.

[121] V. R. Almeida, Q. Xu, C. A. Barrios, and M. Lipson, "Guiding and confining light in void nanostructure," *Opt. Lett.*, vol. 29, no. 11, pp. 1209–1211, Jun. 2004. DOI: 10.1364/OL.29.001209. [Online]. Available: http://ol.osa.org/abstract.cfm?URI=ol-29-11-1209.

[122] R. Palmer, L. Alloatti, D. Korn, W. Heni, P. C. Schindler, J. Bolten, M. Karl, M. Waldow, T. Wahlbrink, W. Freude, C. Koos, and J. Leuthold, "Low-loss silicon strip-to-slot mode converters," *IEEE Photonics Journal*, vol. 5, no. 1, pp. 2 200 409–2 200 409, 2013. DOI: 10.1109/JPHOT.2013.2239283.

[123] A. Yariv, *Optical electronics*. Saunders College Publishing, 1991, ISBN: 9780030702891.

[124] S. Saeedi, B. Abiri, A. Hajimiri, and A. Emami, "Differential optical ring modulator: Breaking the bandwidth/quality-factor trade-off," in *2015 Euro-*

pean Conference on Optical Communication (ECOC), 2015, pp. 1–3. DOI: 10.1109/ECOC.2015.7341731.

[125] W. D. Sacher and J. K. S. Poon, "Dynamics of microring resonator modulators," *Opt. Express*, vol. 16, no. 20, pp. 15 741–15 753, Sep. 2008. DOI: 10.1364/OE.16.015741. [Online]. Available: http://www.opticsexpress.org/abstract.cfm?URI=oe-16-20-15741.

[126] H. Li, G. Balamurugan, M. Sakib, R. Kumar, H. Jayatilleka, H. Rong, J. Jaussi, and B. Casper, "12.1 a 3d-integrated microring-based 112gb/s pam-4 silicon-photonic transmitter with integrated nonlinear equalization and thermal control," in *2020 IEEE International Solid- State Circuits Conference - (ISSCC)*, 2020, pp. 208–210. DOI: 10.1109/ISSCC19947.2020.9063122.

[127] A. M. Gutierrez, J. V. Galan, J. Herrera, A. Brimont, D. Marris-Morini, J. Fédéli, L. Vivien, and P. Sanchis, "High linear ring-assisted mzi electro-optic silicon modulators suitable for radio-over-fiber applications," in *The 9th International Conference on Group IV Photonics (GFP)*, 2012, pp. 57–59. DOI: 10.1109/GROUP4.2012.6324085.

[128] S. Chen, G. Zhou, L. Zhou, L. Lu, and J. Chen, "High-linearity silicon modulator based on a reconfigurable microring-assisted mach-zehnder interferometer," in *2019 18th International Conference on Optical Communications and Networks (ICOCN)*, 2019, pp. 1–3. DOI: 10.1109/ICOCN.2019.8933966.

[129] J. Cardenas, P. A. Morton, J. B. Khurgin, A. Griffith, C. B. Poitras, K. Preston, and M. Lipson, "Linearized silicon modulator based on a ring assisted mach zehnder inteferometer," *Opt. Express*, vol. 21, no. 19, pp. 22 549–22 557, Sep. 2013. DOI: 10.1364/OE.21.022549. [Online]. Available: http://www.opticsexpress.org/abstract.cfm?URI=oe-21-19-22549.

[130] C. Zhang, P. A. Morton, J. B. Khurgin, J. D. Peters, and J. E. Bowers, "Ultralinear heterogeneously integrated ring-assisted mach–zehnder interferometer modulator on silicon," *Optica*, vol. 3, no. 12, pp. 1483–1488, Dec. 2016. DOI: 10.1364/OPTICA.3.001483. [Online]. Available: http://www.osapublishing.org/optica/abstract.cfm?URI=optica-3-12-1483.

[131] S. Akiyama, T. Kurahashi, T. Baba, N. Hatori, T. Usuki, and T. Yamamoto, "A 1 v peak-to-peak driven 10-gbps slow-light silicon mach–zehnder modulator using cascaded ring resonators," *Applied physics express*, vol. 3, no. 7, p. 072 202, 2010. DOI: 10.1143/apex.3.072202. [Online]. Available: https://doi.org/10.1143/apex.3.072202.

[132] S. Akiyama, T. Kurahashi, K. Morito, T. Yamamoto, T. Usuki, and S. Nomura, "Cascaded-ring-resonator-loaded mach–zehnder modulator for enhanced modulation efficiency in wide optical bandwidth," *Opt. Express*,

vol. 20, no. 15, pp. 16 321–16 338, Jul. 2012. DOI: 10.1364/OE.20.016321. [Online]. Available: http://www.opticsexpress.org/abstract.cfm?URI=oe-20-15-16321.

[133] M. S. Rasras, K.-Y. Tu, D. M. Gill, Y.-K. Chen, A. White, S. Patel, A. Pomerene, D. Carothers, J. Beattie, M. Beals, J. Michel, and L. Kimerling, "Demonstration of a tunable microwave-photonic notch filter using low-loss silicon ring resonators," *J. Lightwave Technol.*, vol. 27, no. 12, pp. 2105–2110, Jun. 2009. DOI: 10.1109/JLT.2008.2007748. [Online]. Available: http://jlt.osa.org/abstract.cfm?URI=jlt-27-12-2105.

[134] Z. Zhou and L. S. Feng, "Analysis of a silicon dual-coupled-ring resonator modulator based on push–pull coupling tunings," *IEEE Photonics Journal*, vol. 10, no. 1, pp. 1–12, 2018. DOI: 10.1109/JPHOT.2017.2781689.

[135] Y. Chen and S. Blair, "Nonlinearity enhancement in finite coupled-resonator slow-light waveguides," *Opt. Express*, vol. 12, no. 15, pp. 3353–3366, Jul. 2004. DOI: 10.1364/OPEX.12.003353. [Online]. Available: http://www.opticsexpress.org/abstract.cfm?URI=oe-12-15-3353.

[136] D. G. Rabus, "Ring resonators: Theory and modeling," *Integrated Ring Resonators: The Compendium*, pp. 3–40, 2007. DOI: https://doi.org/10.1007/978-3-540-68788-7_2.

[137] J. K. S. Poon, J. Scheuer, S. Mookherjea, G. T. Paloczi, Y. Huang, and A. Yariv, "Matrix analysis of microring coupled-resonator optical waveguides," *Opt. Express*, vol. 12, no. 1, pp. 90–103, Jan. 2004. DOI: 10.1364/OPEX.12.000090. [Online]. Available: http://www.opticsexpress.org/abstract.cfm?URI=oe-12-1-90.